Biophysical and Structural Approaches to Characterize the Mechanism of P-glycoprotein, a Multidrug Efflux Transporter

Jiarong Mavis Li

A dissertation

submitted in partial fulfillment of the

requirements for the degree of

Doctor of Philosophy

University of Washington

2017

Reading Committee:

William M. Atkins, Chair

Abhinav Nath

Rodney J.Y. Ho

Program Authorized to Offer Degree:

Pharmacy - Medicinal Chemistry

University of Washington

Abstract

Biophysical and Structural Approaches to Characterize the Mechanism of P-glycoprotein, a Multidrug Efflux Transporter

Jiarong Mavis Li

Chair of the Supervisory Committee:
Professor William M. Atkins
Department of Medicinal Chemistry

P-glycoprotein (P-gp), an ATP Binding Cassette transporter (ABCB1), plays an important role in multidrug resistance in cancers and clinical drug interactions. P-gp utilizes the energy from ATP hydrolysis to drive conformational transitions from the inward-facing (IF) to outward-facing (OF) states that lead to extracellular drug release. In addition to the nucleotide-dependent conformational rearrangements which provide alternating access of substrates to intracellular or extracellular milieu, the drug binding sites have been proposed to cycle between high and low affinities to facilitate drug binding or dissociation. However, drug-specific effects on nucleotide-dependent affinity changes to P-gp remain largely uncharacterized. The lack of binding kinetics in general also limits the mechanistic interpretation of P-gp transport. Furthermore, molecular details of IF and OF conformations have not been demonstrated because the structure of OF P-gp remains unavailable by classical methods. To address these questions, this dissertation describes the work in employing complementary biophysical, biochemical and structural techniques to gain additional insight on P-gp. By using Fluorescence Correlation Spectroscopy to monitor fluorescent probe affinities for P-gp, our results indicate that changes in affinities are both probe- and nucleotide-dependent. Combined with a novel antibody-based quenching strategy for vesicle-based transport, we find that Flutax-2 may represent an under-appreciated class of P-gp substrates whereby transport is uncoupled to nucleotide binding and hydrolysis. Hydrogen-Deuterium Exchange Mass Spectrometry was used to characterize the detailed structural dynamics of P-gp in the IF or OF states, and in detergent or nanodiscs environment. Vanadate inhibition of P-gp to promote the OF conformations leads to an overall decrease in deuterium uptake throughout the NBDs, but also causes an increased solvent exposure of a peptide from TM1 which supports the OF conformation with an opening of drug binding sites towards extracellular space. Interestingly, several peptides displaying EX1 exchange kinetics indicate that P-gp motions occur on a wide range of time scale, from seconds to hours. Lastly, Surface Plasmon Resonance is presented as viable technique for studying drug interactions with membrane proteins reconstituted into nanodiscs. Experimental considerations, advantages and disadvantages associated with different biosensor chips are discussed, and successful preliminary experiments with small-molecules binding to P-gp nanodiscs are demonstrated. Together, these results shed light on the complex structural and functional mechanism of P-gp.

TABLE OF CONTENTS

LIST OF FIGURES

LIST OF TABLES

ACKNOWLEDGEMENTS

First of all, I would like to thank Bill Atkins for his unwavering support and guidance during the entire course of my training. I would also like to thank Mike Dabrowski, Hyewon Kwon, Mauro Acchione, Michele Scian, Nick Treuheit, Michelle Redhair and Dennis Goulet for making my time spent in the lab fulfilling and memorable. Additionally, I would like to thank Abhi Nath for great advice and stimulating discussions on FCS, and Mike Guttman for sharing his expertise on HDX experiments. I also appreciate many useful feedback from my committee members, Rodney Ho, Jash Unadkat and Kelly Lee.

Last but not the least, I would like to give special thanks to my parents, Ngan Yin Chan and Tung Li, aunties Chet Mui Chan and Loke Yin Chan, brother and sister Nicholas and Nicholette Li, for their unconditional love and support in their own ways, and to my husband, Shaowei Png, for being the most understanding and supportive companion during this journey.

Chapter 1

Introduction to P-glycoprotein as an ATP-dependent Efflux Transporter, with Emphasis on Cooperativity between Drug Binding, ATP Hydrolysis and Conformational Switch

1.1 P-glycoprotein

1.1.1 Structure and Function

In living cells, membrane transporters are essential for regulating the movement of solutes, small molecules and macromolecules across biological membranes. Among these transporters, members of the ATP-binding cassette (ABC) family are active transporters. From prokaryotes to eukaryotes, a key role of these transmembrane ATPases is to harness energy from hydrolysis of ATP to transport nutrients into cells (importers) or to export metabolic byproducts or xenobiotics out of cells (exporters). In humans, there are 49 ABC genes that are classified into 7 subfamilies (ABC-A to ABC-G) based on sequence homology and all function as exporters (1). P-glycoprotein (P-gp), also known as ABCB1 or multidrug resistance protein 1 (MDR1), is a clinically important ABC efflux transporter that has a protective role. P-gp mediates the secretion of metabolites and drugs into the bile, urine and lumen of the gastrointestinal tract, as evidenced by the localization of P-gp on the apical surface of epithelial cells in small biliary ductules in the liver, proximal tubules in the kidney, and columnar cells in the colon. Likewise, P-gp is also found at the blood-brain, blood-placenta, and blood-testis barriers to protect vital organs from toxins and xenobiotics (2).

Although the 3D crystal structure of human P-gp (MDR1A) is unavailable, a significant understanding of its mechanism is derived from crystal structures of mouse P-gp (mdr1a/mdr3) and bacterial ABC transporters (such as Sav 1866). Like all ABC proteins, P-gp has a structural core of two transmembrane domains (TMDs) and two nucleotide binding domains (NBDs). While some members of the family are half transporters consisting of subunits that form homodimers or heterodimers, P-gp is a full transporter consisting of a single polypeptide of 1280 amino acid residues (~170 kDa) arranged in two homologous halves from an amino terminal TMD to a cytosolic NBD.

The NBDs of P-gp each contain several highly conserved motifs, including the Walker A and B sequences, the signature C motif, and the H loop and Q loop. The TMDs each comprise six transmembrane helices which form multiple, overlapping drug binding sites that contribute to the substrate promiscuity. It has been widely proposed that during ATP binding and hydrolysis, P-gp undergoes a large scale conformational change, which involves NBD dimerization (to form a "nucleotide-sandwich" dimer) coupled to conformational rearrangements in the TMD (3,4). This conformational change converts P-gp from an inward-facing (IF), open conformation to an outward-facing (OF), closed conformation that facilitates translocation of drugs across the lipid membrane (Figure 1.1). As discussed further in this chapter, it is becoming apparent that P-gp does not simply exist as a two-state, IF or OF system. There is compelling evidence that indicates that the transporter is conformationally heterogeneous and flexible. That is, P-gp exists as an equilibria of multiple partially open or closed states. It could be envisaged that the multiple conformations present a large selection of drug binding sites that contribute to the broad substrate specificity of P-gp, and the intrinsic flexibility facilitates the interconversion between conformations to contribute to its function as an efflux pump. However, it is also very likely that the structural heterogeneity and dynamics of P-gp hampers years of crystallization efforts and makes this a challenging membrane protein to study.

1.1.2 Physiological and Clinical Significance, Motivation for Study

One of the most critical functions of P-gp is its protective role in the blood brain barrier, as demonstrated with mdr1a double knockout mice (5). Nearly all the knockout mice died after exposure to ivermectin, a pesticide which does not cause adverse effects in normal mice. The knockout mice accumulated a nearly 100-fold increase in ivermectin in the brain, which indicated that P-gp in the blood brain barrier played a crucial role in excluding xenobiotics or drug substrates from the brain compartment. Structurally, the blood brain barrier consists of endothelial cells that are joined together by tight junctions and very little fenestration or pinocytosis occurs in these cells (6). The blood brain barrier is therefore less leaky compared to blood capillaries in other parts of the body, and generally, larger and more hydrophobic molecules are required to partition into the endothelial cells in order to reach the brain. It is now well-established that P-gp at the blood brain barrier helps to prevent penetration of large, hydrophobic drugs into the brain. P-gp plays a similar role in other sanctuary sites such as placenta, testis, and kidney (2,7,8).

Clinically, there is considerable interest in P-gp because of the role it plays in drug-drug interactions, bioavailability and multidrug resistant (MDR) cancers. For example, induction of P-gp activity reduces bioavailability of orally administered drugs and decreases therapeutic efficacy. Inhibition of P-gp activity, on the other hand, increases bioavailability of the drug but potentially leads to an increased risk of drug-associated toxicities or side effects. Due to the efflux function of P-gp, overexpression of the protein confers multi-drug resistance in malignancies such as colon and kidney cancers because many anticancer drugs like the anthracyclines, taxanes and vinca alkaloids are substrates of P-gp. Even in cancers that have a low basal level of expression, P-gp is found to be upregulated following prolonged exposure to chemotherapy, resulting in poor prognosis (9). Potential drug-drug interactions also occur when P-gp inhibitors intended to act as chemosensitizers are substrates for the drug metabolizing cytochrome P450s (10). Induction or inhibition of the cytochrome P450s by the chemosensitizers alters the metabolism of co-administered anti-cancer drugs and this presents significant challenges in chemotherapy dosage adjustments because of unpredictable drug metabolism and clearance pathways.

Approaches to inhibit P-gp activity are essential to overcome P-gp dependent MDR cancers. Highly specific P-gp inhibitors that lack interactions with the P450s have been developed over the years but none have been clinically approved due to severe toxicities accompanying increased brain penetration of anticancer drugs (11). In addition to the continuous pursuit of novel, highly specific P-gp inhibitors from a variety of sources, other proposed strategies include control of protein expression for direct therapeutic purposes and tailoring drug regimens to include P-gp inhibitors based on anticancer drugs used. Additionally, it is imperative to investigate the molecular basis of P-gp as an ATP-dependent transporter in order to establish new solutions to treat mdr cancers. Other human ABC transporters share many structural and functional features and overlapping substrate specificities with P-gp. Therefore, P-gp remains the prototypical transporter from a mechanistic perspective and a major target for pharmacological intervention of the clearance of other drugs.

The aim of this dissertation is to investigate the molecular details of P-gp transport. Compared to the very fast, diffusion rate-limited transport process associated with ion channels, protein-mediated transport processes such as facilitated diffusion and active transport are slower processes because of additional requirements for ligand binding and protein conformational changes. This presents an opportunity for biophysical and biochemical characterization of the elementary rate constants and identifying the rate-limiting step involved in P-gp transport cycle. In addition, the mechanistic knowledge from studies with P-gp may have broader implications for other ABC transporters.

1.1.3 Catalytic and Transport Mechanism

A generally described mechanism of transport pathway of P-gp includes a putative transition state that has been well-characterized and linked to a conformational change that is necessary for transmembrane movement of drugs (12-15). Although the exact sequence of events that occur during the energy-dependent drug transport process remains uncertain, an early model proposed by Sauna *et al*. involved the following basic steps: 1) Initiation of the transport pathway by ATP binding and/or drug binding, 2) Dimerization of the NBDs following ATP binding and/or hydrolysis, 3) Conformational rearrangements at the TMDs that is coupled to a high to low affinity switch at the drug binding site that releases the drug, and 4) Resetting the pump with binding/hydrolysis of a second ATP molecule (16). A confounding aspect in the analysis of P-gp mediated drug transport is the presence of basal activity even in the absence of drugs, which is sometimes not incorporated into transport models. A more elaborate model based on analysis of the transition state of P-gp was proposed by Al-Shawi *et al*., which took into account both basal and drug-stimulated ATPase activity of P-gp and also demonstrated that the transition states involved in the drug-coupled and uncoupled activity are different (Figure 1.2; adapted from (17)). The model suggests that P-gp exists in at least two active populations, an uncoupled and coupled form that transports drugs. In the absence of drugs, the uncoupled form leads to basal ATPase activity, whereas in the presence of drugs, more P-gp is recruited to the transport competent coupled population. Therefore, at relatively high drug concentrations, P-gp presumably exists only in the coupled form with high drug affinity sites. Besides the basal and drug stimulated activity (in the absence of drugs and presence of activating concentrations of drugs respectively), very high concentrations of drugs generally result in drug inhibited activity, possibly through occupying low affinity sites that induce new conformations.

Associated with the transport cycle is the generally accepted model of alternating catalysis of the NBDs (Figure 1.3). Extensive studies that exploit vanadate trapping of nucleotide at either catalytic site, mutations or chemical modifications which inactivate one catalytic site, completely abolished ATP hydrolysis at the other site (18-20). Therefore, it is postulated that when one site enters the post-hydrolysis transition state, the other site cannot do so, and the NBDs catalyze ATP hydrolysis alternately (21). In addition, although P-gp is likely to be bound with two molecules of ATP under physiological conditions, it has been demonstrated that the energy from hydrolysis of one ATP molecule is sufficient to drive transport (17). It is proposed that P-gp keeps a "conformational memory" of which NBD last hydrolyzed ATP, and catalysis takes place in a reciprocal fashion. In Figure 1.2, the binding of a new molecule of ATP (shown) promotes the hydrolysis of a previously bound ATP molecule.

Historically, the "processive clamp" model was proposed in lieu of the alternating catalysis model, because Tampe et al. isolated NBD dimers containing two ADPs in addition to those containing one ATP and one ADP, and two ATPs. Therefore, it was hypothesized that both ATPs can be hydrolyzed sequentially in a single cycle (22). A main feature of the model is the ATP-induced NBD dimerization which causes a conformational change in the TMDs that displaces the drug, and NBD dissociation following sequential ATP hydrolysis that resets the transporter. Although it is now clear that the alternating catalytic site model is operative because subsequent biochemical studies demonstrated an 'occluded' ATP molecule in the NBDs, it is noteworthy that the mechanistic concepts of ATP-induced NBD dimerization and ADP-induced dissociation prevail across different models.

1.2 Overview: Multiple Drug Binding Sites of P-gp

P-gp has been estimated to bind more than 300 different compounds. However, how P-gp recognizes and binds a diverse array of anticancer drugs, cyclic peptides, xenobiotics, lipids and detergents is still a subject of intense debate. P-gp has been described as a 'flippase' or 'hydrophobic vacuum cleaner' in earlier models with heavy emphasis on substrate-lipid interactions (23). However, it has become clear with many investigations that there are more specific, multiple drug binding sites on P-gp that contribute to its broad substrate specificity. Multiple binding sites were located within P-gp using a range of photoaffinity analogs that labeled both the N- and C- terminal halves of the transmembrane regions, and classical radioligand binding and displacement experiments revealed competitive or non-competitive interactions. One of the earliest studies demonstrated the presence of two distinct, positively cooperative, transport sites termed the H site for Hoechst 33342 (that also binds colchicine), and R site for Rhodamine 123 (also binds anthracyclines) (24). A third binding site for prazosin and progesterone was also reported (25). Later, more extensive binding studies revealed at least four distinct binding sites that are linked by negative heterotropic allostery and up to seven different binding sites on P-gp has been reported (26). Besides the competitive and non-competitive interactions between drugs, it has also been shown that multiple molecules of a drug can bind simultaneously to P-gp based on biphasic ATPase and binding assays, which suggest that low affinity and high affinity sites exist (27,28). Furthermore, these binding sites have also been classified as transport or modulatory sites, because some substrates are transported by P-gp but others modulate its ATPase activity without being transported. Currently, direct drug binding studies with P-gp are limited and most of these are not related to the rates of drug transport. In other words, there is a disconnect between binding and transport kinetics, and it is unclear whether the transport sites of P-gp are related to the high and low drug affinity sites. We attempt to address this gap in knowledge in Chapter 2, where we use Fluorescence Correlation Spectroscopy (FCS) to selectively probe the high affinity sites of ligand binding and perform vesicular transport experiments under conditions that populate the high affinity sites.

1.3 Overview: Allosteric Interactions between Drug Binding Sites and Nucleotide Binding Domains

Conformational changes transmitted between drug binding sites and nucleotide binding domains are believed to drive translocation of drugs across the membrane. Drug binding at the TMDs has been shown to quench the fluorescence probe MIANS covalently bound at the NBDs (29). Cross-talk in the reverse direction has been demonstrated by the ability of nucleotide binding and hydrolysis within the NBDs to elicit conformational changes at the TMDs, as shown by tryptophan quenching, limited trypsin digestion, photolabeling and changes in binding of UIC2 antibody to the extracellular epitope on P-gp (14,30,31). Overall, these investigations suggest inter-domain communication via conformational changes; however, few studies actually explored how cycling between high and low drug affinity binding sites differentially affect P-gp conformation and promote drug translocation.

Several lines of research suggest that drug binding and nucleotide binding are coupled. However, to date, biochemical strategies for investigating nucleotide-dependent changes in drug binding affinity remain difficult and results are controversial. For example, photolabeling studies with iodoaryl-azidoprazosin (IAAP) showed a reduction in substrate binding when P-gp was trapped by vanadate in a post-hydrolysis conformation (30). However, using equilibrium radioligand binding assays, another group demonstrated that a reduction in drug binding affinity was effected not only by post-hydrolysis vanadate trapping, but also with a non-hydrolysable nucleotide analog AMP-PNP (27). This suggests that nucleotide binding and hydrolysis led to a decrease in drug binding. In contrast to these studies, fluorescence quenching experiments with MIANS using detergent solubilized P-gp showed no change in affinity for many drugs at different nucleotide bound states (32). Based on these studies two opposing models of how P-gp transports drugs have been proposed. The first multistep model proposed that, for efficient and rapid translocation of drugs, the drug binding sites switch from high affinity (for drug association) to low affinity (for drug dissociation) that are alternately exposed to the opposite sides of the bilayer during ATP binding or hydrolysis. A second model proposed that nucleotide binding has no effect on drug affinity. These observations may arise from underlying differences in reconstitution methods, such as liposomes/membrane vesicles vs lipid-detergent micelles, and also from direct (radioligand binding assays) versus indirect measurements of drug binding affinity. These results also likely indicate that coupling between nucleotide bound conformations and drug binding is dependent on the identity of the drug. In general, much remains to be learned about the nucleotide-dependent interactions between drugs and P-gp and additional binding studies with new strategies are required. In Chapter 2, FCS together with nanodiscs technology, allow us to probe both the drug binding and nucleotide binding sites of P-gp and to study nucleotide-dependent effects on probe affinity changes. In Chapter 4, Surface Plasmon Resonance (SPR) may provide an additional strategy to measure drug binding affinities to P-gp although more work is needed to extract the rate constants.

1.4 Overview: Nucleotide or Drug-induced Conformational Change and Structural Complexities

A gap in our current understanding of P-gp mechanism is the extent to which the NBDs engages or dissociates as P-gp transits from an IF to OF conformation, and how these movements are coupled to helical rearrangements in the TMDs during a transport cycle. The first X-ray crystallographic structure of P-gp in the nucleotide-free, IF, open state was solved for the murine isoform and refined recently (33,34). Although ATP hydrolysis is proposed to require the association or close contact between the NBDs based on studies of analogous bacterial ABC transporters, no matching OF or closed conformation of any eukaryotic ABC transporter has been reported. Rather, many studies have used homology modeling to construct such an OF conformation using SAV1866 as a template (35). Notably, among structures reported for murine and *C.elegans* P-gp, there is a continuum of IF conformations with various extent of NBD separation (46 Å to 72Å), which suggests conformational flexibility of the transporter. Early FRET experiments that utilized P-gp labeled with donor and acceptor fluorophores at the NBDs reported paradoxical results. MIANS/NBD labeled P-gp in the presence of detergent demonstrated no significant changes in energy transfer efficiency when P-gp was in the resting state, in presence of drug or ATP alone, or with a combination of ATP and drug (36). In contrast, cysteine mutants of P-gp labeled with Alexa 488 and Atto dyes reconstituted into liposomes showed around 5-10% increase in FRET efficiency in the presence of ATP and between 10- 20% increase in the presence of vanadate (versus resting state). The authors also observed at least three populations of FRET efficiencies under conditions of verapamil transport using single molecule FRET, which they attribute to at least three major conformations of P-gp during a transport cycle (37). Most recent studies using single particle electron microscopy provide conflicting results, again, with different reconstitution systems. With cryo-EM, human P-gp in detergent micelles were reported to undergo a switch from IF to OF conformation in the post-hydrolysis state with vanadate trapping in the absence of drugs (38). However, this was not observed by negative stain EM using mouse P-gp in bicelles or nanodiscs and the IF to OF conformational change was only shown with vanadate trapped P-gp in the presence of drugs (39). The resolution of the techniques may result in the differences, because cryo-EM enables higher resolution of the particles compared to negative stain EM. Furthermore, it is possible that P-gp in bicelles or nanodiscs may have different conformational dynamics compared to P-gp in detergent. Although the P-gp isoforms are different in the two studies (human versus mouse), mouse P-gp has 87% sequence homology with human P-gp and it is unlikely that they are structurally dissimilar. A common feature reported in both studies is that P-gp exists in both IF and OF conformations, although it was reported to be of equal ratio for human P-gp in detergent micelles, but only up to 3% of the OF conformation for mouse P-gp in lipid membranes. These biochemical data highlight that conformational heterogeneity of P-gp may contribute, and it may also be possible that the authors have employed different classification systems that resulted in different 3D reconstruction of P-gp conformations. The NBDs of P-gp likely does not dimerize with a tight interface, unlike homologous bacterial exporters (such as MsbA), and this is likely to result in subjective assessment of particles as open or closed states. Without the crystal structure of P-gp in the OF state, orthogonal structural techniques are required to study the conformational changes of P-gp. In Chapter 3, we use Hydrogen Deuterium Exchange Mass Spectrometry (HDX-MS) to compare structural changes and solvent accessibility between mouse P-gp in the resting and post-hydrolysis states, in both detergent and nanodiscs environment.

1.5 Summary

This chapter serves to emphasize that a multi-faceted approach is required to elucidate the mechanism of drug transport by P-gp. Despite more than 30 years of biochemical research, direct binding experiments to measure drug or nucleotide affinities remain scant and difficult, because many hydrophobic substrates of P-gp are poorly soluble in aqueous buffers and non-specific interactions are prevalent. Furthermore, very weak affinity interactions between nucleotides and P-gp (millimolar range) prohibit many biochemical and biophysical characterizations. In addition, different reconstitution systems between studies likely contribute to the disparate results and a detergent-free membrane environment for studying P-gp has been recommended (40). P-gp reconstituted into lipid nanodiscs is reported to behave similarly to P-gp in liposomes or native membranes, and has additional advantages such as homogeneous size distribution and accessibility of both intracellular and extracellular epitopes for analyses.

The remainder of this dissertation is, therefore, dedicated to efforts made towards applying state-of-the-art biophysical strategies, in combination with a lipid nanodisc model membrane platform, to provide new insights on P-gp-ligand interactions and structural changes.

Figures

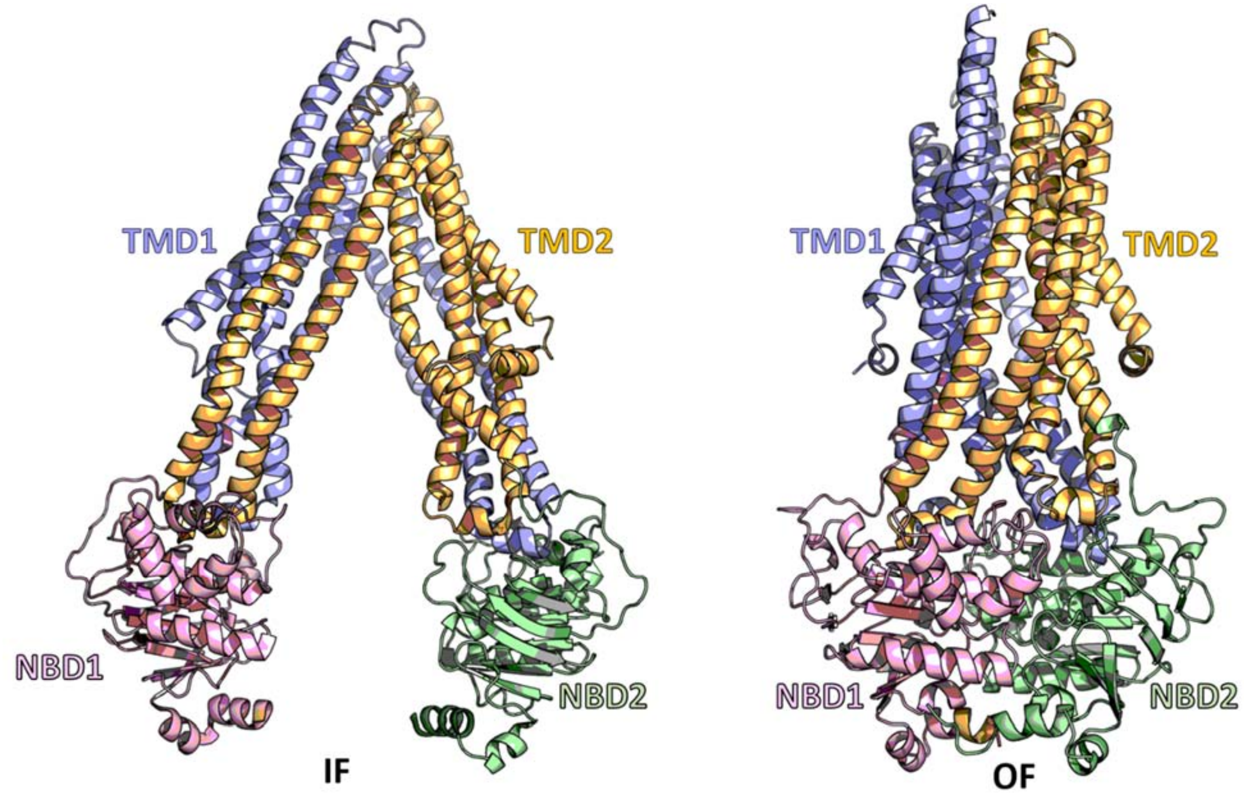

Figure 1.1. Cartoon representations of mouse P-gp in different conformations. Crystal structure of P-gp in the IF (inward-facing) conformation (PDB ID: 4Q9H, left) and homology model of P-gp in the OF (outward-facing) conformation (PMDB: PM0075213, right) with Sav1866 as a template. Shown in light blue, light pink, light orange and pale green are regions corresponding to TMD1 (residues 31-366), NBD1 (residues 367-625), TMD2 (residues 687-1010) and NBD2 (residues 1011-1272) respectively.

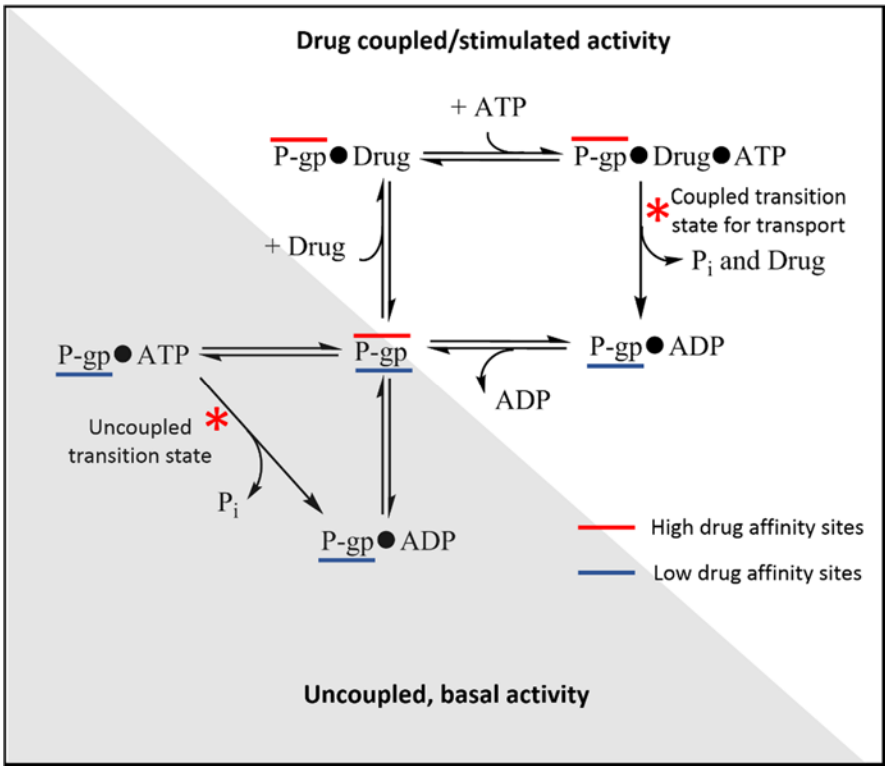

Figure 1.2. Activity and transport cycle of P-glycoprotein, modified from (17). In the absence of drug, but in the presence of ATP, P-gp partitions into the uncoupled cycle (lower, shaded) and hydrolyses ATP without doing any transport work. This constitutes the basal activity of P-gp. In the presence of a drug substrate, P-gp partitions into the coupled activity cycle in which drug transport is coupled to ATP hydrolysis and results in the stimulated activity of P-gp (upper, unshaded cycle). Drug binding promotes the binding of a second ATP molecule at the nucleotide binding domain, which leads to the subsequent hydrolysis of a bound ATP from the previous catalytic cycle (alternating catalysis, figure 1.3). After passing through a high energy transition state (red asterisk), the drug is released to the extracellular space, followed by the release of Pi and ADP. The two transition states (two red asterisks) represent two different experimentally determined protein conformations, from (17).

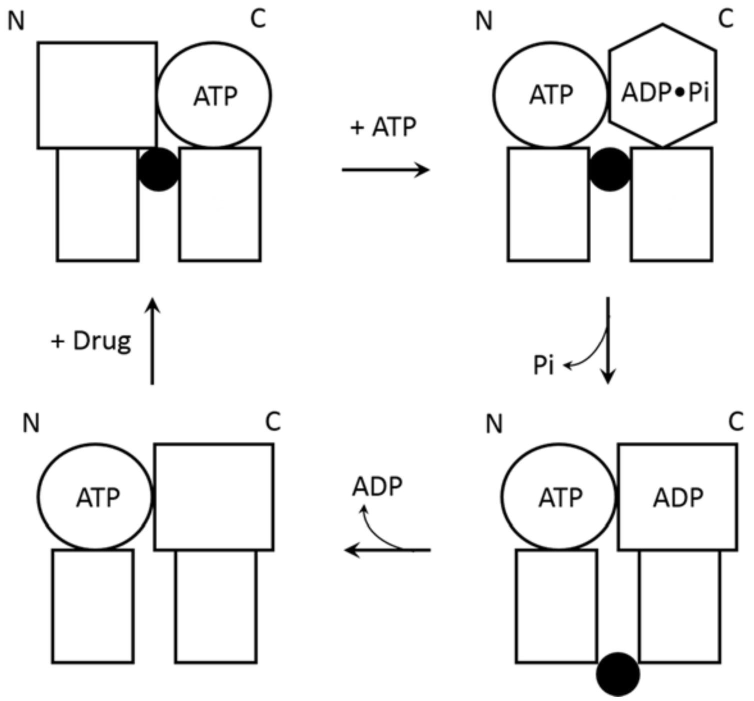

Figure 1.3. A proposed model for alternating catalysis by P-gp, adapted from (21). Rectangles represent the two transmembrane domains of P-gp; circle, square and hexagon represent different NBD conformations when occupied by ATP, ADP or no nucleotide, and ADP•Pi respectively. A hypothetical cycle begins when drug binds at a site within the transmembrane domains, and the N catalytic site is empty while the C catalytic site has a bound ATP (top left). The binding of a new molecule of ATP at the N site allows ATP hydrolysis at the C site, and the post-hydrolysis conformation at the C-site prevents hydrolysis at the N site (top right). The post-hydrolysis, high chemical potential state of the C site after bond cleavage is depicted as a hexagon. Relaxation of the C site occurs, which is coupled to rearrangements in the TMDs that results in the release of drug from inward-facing, high affinity site to outward-facing, lower affinity site and Pi is released (bottom right). Drug and ADP dissociates from P-gp, and the cycle resets (bottom left) but now the ATP molecule at the N site will undergo hydrolysis when a new molecule of ATP binds to the C site in the next cycle.

1.6 References

1. Vasiliou, V., Vasiliou, K., and Nebert, D. W. (2009) Human ATP-binding cassette (ABC) transporter family. *Hum Genomics* **3**, 281-290
2. Thiebaut, F., Tsuruo, T., Hamada, H., Gottesman, M. M., Pastan, I., and Willingham, M. C. (1987) Cellular localization of the multidrug-resistance gene product P-glycoprotein in normal human tissues. *Proc Natl Acad Sci U S A* **84**, 7735-7738
3. Crowley, E., O'Mara, M. L., Kerr, I. D., and Callaghan, R. (2010) Transmembrane helix 12 plays a pivotal role in coupling energy provision and drug binding in ABCB1. *FEBS J* **277**, 3974-3985
4. Martin, C., Berridge, G., Mistry, P., Higgins, C., Charlton, P., and Callaghan, R. (2000) Drug binding sites on P-glycoprotein are altered by ATP binding prior to nucleotide hydrolysis. *Biochemistry* **39**, 11901-11906
5. Schinkel, A. H. (1999) P-Glycoprotein, a gatekeeper in the blood-brain barrier. *Adv Drug Deliv Rev* **36**, 179-194
6. Goldstein, G. W., and Betz, A. L. (1986) The blood-brain barrier. *Sci Am* **255**, 74-83
7. Arceci, R. J., Croop, J. M., Horwitz, S. B., and Housman, D. (1988) The gene encoding multidrug resistance is induced and expressed at high levels during pregnancy in the secretory epithelium of the uterus. *Proc Natl Acad Sci U S A* **85**, 4350-4354
8. Mruk, D. D., Su, L., and Cheng, C. Y. (2011) Emerging role for drug transporters at the blood-testis barrier. *Trends Pharmacol Sci* **32**, 99-106
9. Bradley, G., and Ling, V. (1994) P-glycoprotein, multidrug resistance and tumor progression. *Cancer Metastasis Rev* **13**, 223-233
10. Yasuda, K., Lan, L. B., Sanglard, D., Furuya, K., Schuetz, J. D., and Schuetz, E. G. (2002) Interaction of cytochrome P450 3A inhibitors with P-glycoprotein. *J Pharmacol Exp Ther* **303**, 323-332
11. Srivalli, K. M. R., and Lakshmi, P. K. (2012) Overview of P-glycoprotein inhibitors: a rational outlook. *Brazilian Journal of Pharmaceutical Sciences* **48**, 353-367
12. Urbatsch, I. L., Tyndall, G. A., Tombline, G., and Senior, A. E. (2003) P-glycoprotein catalytic mechanism: studies of the ADP-vanadate inhibited state. *J Biol Chem* **278**, 23171-23179
13. Loo, T. W., and Clarke, D. M. (2000) Drug-stimulated ATPase activity of human P-glycoprotein is blocked by disulfide cross-linking between the nucleotide-binding sites. *J Biol Chem* **275**, 19435-19438
14. Sonveaux, N., Vigano, C., Shapiro, A. B., Ling, V., and Ruysschaert, J. M. (1999) Ligand-mediated tertiary structure changes of reconstituted P-glycoprotein. A tryptophan fluorescence quenching analysis. *J Biol Chem* **274**, 17649-17654
15. Rosenberg, M. F., Kamis, A. B., Callaghan, R., Higgins, C. F., and Ford, R. C. (2003) Three-dimensional structures of the mammalian multidrug resistance P-glycoprotein demonstrate major conformational changes in the transmembrane domains upon nucleotide binding. *J Biol Chem* **278**, 8294-8299
16. Sauna, Z. E., and Ambudkar, S. V. (2001) Characterization of the catalytic cycle of ATP hydrolysis by human P-glycoprotein. The two ATP hydrolysis events in a single catalytic cycle are kinetically similar but affect different functional outcomes. *J Biol Chem* **276**, 11653-11661

17. Al-Shawi, M. K., Polar, M. K., Omote, H., and Figler, R. A. (2003) Transition state analysis of the coupling of drug transport to ATP hydrolysis by P-glycoprotein. *J Biol Chem* **278**, 52629-52640
18. Tombline, G., Bartholomew, L. A., Urbatsch, I. L., and Senior, A. E. (2004) Combined mutation of catalytic glutamate residues in the two nucleotide binding domains of P-glycoprotein generates a conformation that binds ATP and ADP tightly. *J Biol Chem* **279**, 31212-31220
19. Sauna, Z. E., Nandigama, K., and Ambudkar, S. V. (2006) Exploiting reaction intermediates of the ATPase reaction to elucidate the mechanism of transport by P-glycoprotein (ABCB1). *J Biol Chem* **281**, 26501-26511
20. Sauna, Z. E., Muller, M., Peng, X. H., and Ambudkar, S. V. (2002) Importance of the conserved Walker B glutamate residues, 556 and 1201, for the completion of the catalytic cycle of ATP hydrolysis by human P-glycoprotein (ABCB1). *Biochemistry* **41**, 13989-14000
21. Senior, A. E., al-Shawi, M. K., and Urbatsch, I. L. (1995) The catalytic cycle of P-glycoprotein. *FEBS Lett* **377**, 285-289
22. Janas, E., Hofacker, M., Chen, M., Gompf, S., van der Does, C., and Tampe, R. (2003) The ATP hydrolysis cycle of the nucleotide-binding domain of the mitochondrial ATP-binding cassette transporter Mdl1p. *J Biol Chem* **278**, 26862-26869
23. Sharom, F. J. (2014) Complex Interplay between the P-Glycoprotein Multidrug Efflux Pump and the Membrane: Its Role in Modulating Protein Function. *Front Oncol* **4**, 41
24. Shapiro, A. B., and Ling, V. (1997) Positively cooperative sites for drug transport by P-glycoprotein with distinct drug specificities. *Eur J Biochem* **250**, 130-137
25. Shapiro, A. B., Fox, K., Lam, P., and Ling, V. (1999) Stimulation of P-glycoprotein-mediated drug transport by prazosin and progesterone. Evidence for a third drug-binding site. *Eur J Biochem* **259**, 841-850
26. Safa, A. R. (2004) Identification and characterization of the binding sites of P-glycoprotein for multidrug resistance-related drugs and modulators. *Curr Med Chem Anticancer Agents* **4**, 1-17
27. Martin, C., Higgins, C. F., and Callaghan, R. (2001) The vinblastine binding site adopts high- and low-affinity conformations during a transport cycle of P-glycoprotein. *Biochemistry* **40**, 15733-15742
28. Litman, T., Zeuthen, T., Skovsgaard, T., and Stein, W. D. (1997) Structure-activity relationships of P-glycoprotein interacting drugs: kinetic characterization of their effects on ATPase activity. *Biochim Biophys Acta* **1361**, 159-168
29. Liu, R., and Sharom, F. J. (1996) Site-directed fluorescence labeling of P-glycoprotein on cysteine residues in the nucleotide binding domains. *Biochemistry* **35**, 11865-11873
30. Ramachandra, M., Ambudkar, S. V., Chen, D., Hrycyna, C. A., Dey, S., Gottesman, M. M., and Pastan, I. (1998) Human P-glycoprotein exhibits reduced affinity for substrates during a catalytic transition state. *Biochemistry* **37**, 5010-5019
31. Druley, T. E., Stein, W. D., and Roninson, I. B. (2001) Analysis of MDR1 P-glycoprotein conformational changes in permeabilized cells using differential immunoreactivity. *Biochemistry* **40**, 4312-4322
32. Qu, Q., Chu, J. W., and Sharom, F. J. (2003) Transition state P-glycoprotein binds drugs and modulators with unchanged affinity, suggesting a concerted transport mechanism. *Biochemistry* **42**, 1345-1353

33. Aller, S. G., Yu, J., Ward, A., Weng, Y., Chittaboina, S., Zhuo, R., Harrell, P. M., Trinh, Y. T., Zhang, Q., and Urbatsch, I. L. (2009) Structure of P-glycoprotein reveals a molecular basis for poly-specific drug binding. *Science* **323**, 1718-1722
34. Li, J., Jaimes, K. F., and Aller, S. G. (2014) Refined structures of mouse P-glycoprotein. *Protein Sci* **23**, 34-46
35. Dawson, R. J., and Locher, K. P. (2007) Structure of the multidrug ABC transporter Sav1866 from Staphylococcus aureus in complex with AMP-PNP. *FEBS Lett* **581**, 935-938
36. Qu, Q., and Sharom, F. J. (2001) FRET analysis indicates that the two ATPase active sites of the P-glycoprotein multidrug transporter are closely associated. *Biochemistry* **40**, 1413-1422
37. Verhalen, B., Ernst, S., Borsch, M., and Wilkens, S. (2012) Dynamic ligand-induced conformational rearrangements in P-glycoprotein as probed by fluorescence resonance energy transfer spectroscopy. *J Biol Chem* **287**, 1112-1127
38. Frank, G. A., Shukla, S., Rao, P., Borgnia, M. J., Bartesaghi, A., Merk, A., Mobin, A., Esser, L., Earl, L. A., Gottesman, M. M., Xia, D., Ambudkar, S. V., and Subramaniam, S. (2016) Cryo-EM Analysis of the Conformational Landscape of Human P-glycoprotein (ABCB1) During its Catalytic Cycle. *Mol Pharmacol* **90**, 35-41
39. Moeller, A., Lee, S. C., Tao, H., Speir, J. A., Chang, G., Urbatsch, I. L., Potter, C. S., Carragher, B., and Zhang, Q. (2015) Distinct conformational spectrum of homologous multidrug ABC transporters. *Structure* **23**, 450-460
40. Shukla, S., Abel, B., Chufan, E. E., and Ambudkar, S. V. (2017) Effect of Detergent Micelle Environment on P-glycoprotein (ABCB1)-Ligand Interactions. *Journal of Biological Chemistry*

Chapter 2

Differential Coupling of Binding, ATP Hydrolysis and Transport of Fluorescent Probes with P-glycoprotein in Lipid Nanodiscs

Parts of this chapter are taken from the published manuscript:

Li, M. J., Nath, A., and Atkins, W. M. (2017) Differential Coupling of Binding, ATP Hydrolysis, and Transport of Fluorescent Probes with P-Glycoprotein in Lipid Nanodiscs. *Biochemistry* **56**, 2506-2517

2.1 Introduction

P-glycoprotein (P-gp; ABCB1) plays a critical role in drug disposition and drug resistance by exporting a wide range of structurally diverse xenobiotics from several cell types. As discussed in Chapter 1, based on crystallographic models of mammalian P-gp in the absence of nucleotide (4,5) and results with bacterial P-gp homolog in the presence of nucleotides (6), it is well-established that binding and hydrolysis of ATP are coordinated to large scale conformational changes (7,8) that lead to alternate formation of inward-facing and outward-facing states (Figure 2.1). The binding and hydrolysis of ATP are coupled to binding and transport of different drugs in a drug-dependent manner. One possible outward-facing state is stabilized by addition of ATP or ADP with vanadate (9), and the resulting vanadate-trapped state has provided a model for the hydrolytic transition state or the post-hydrolysis state, and possibly other outward-facing conformations.

However, data suggest that different drugs elicit different conformations and hence differential coupling between drug transport and nucleotide-bound states. In addition, many drugs are known to bind with a stoichiometry greater than 1 drug per P-gp, possibly as high as 4 or 5 drugs per P-gp. It is likely that the two-state nucleotide-dependent scheme (inward-facing vs. outward-facing) is oversimplified, and each of these states may include substrate-dependent conformational ensembles that depend on both the identity of the drug bound and the number of drugs bound, as recently emphasized with verapamil (11).

Such mechanistic details have been difficult to study and to relate to actual drug transport *in vivo*. One source of this difficulty results from a lack of biochemical characterization of drug or probe substrate interactions with P-gp. For example, many *in vitro* fluorescent probe substrates are used in cell-based transport assays, but details of their molecular interactions with P-gp are not established, making it difficult to relate transport behavior to molecular mechanism. In effect, rates of probe transport in cell-based assays have not been related to their fundamental biochemical behavior or their specific interactions with P-gp. Interpretation of transport behavior of these fluorescent probe substrates would be facilitated with additional characterization of their binding interactions with P-gp. Notably, the structures of the fluorescent probes used here deviate significantly from their corresponding parent drugs so it should not be assumed that the drug and corresponding fluorophore bind at the same site.

It has also been technically difficult to apply many biochemical methods to P-gp in detergent solution or liposomal preparations. As mentioned in Chapter 1, results on changes in drug affinity for P-gp in different nucleotide-bound states in a detergent environment or in a lipid bilayer have been contradictory (12-14). In general, additional details concerning the nucleotide-dependent interactions of probes and drugs with P-gp are required to fully understand its mechanism and new methods to study these interactions may contribute.

We have previously established P-gp in lipid nanodiscs as a platform for its biochemical and biophysical characterization. For example, conformation specific antibodies against human P-gp in nanodiscs differentially recognize the vanadate-trapped nucleotide-bound P-gp vs. nucleotide free and other nucleotide-bound states, as probed by SPR (15). Here we extend the nanodisc platform with a comparison of DMPC and *E. coli* lipid nanodiscs, to monitor the affinity of probe ligands to different nucleotide-bound states of murine P-gp using fluorescence correlation spectroscopy (FCS). FCS measures the fluctuation in fluorescent intensity of single molecules over time and reports on the diffusion properties of the fluorescent molecules. In particular, FCS has some advantages over other fluorescence based approaches. One advantage is the extraordinary sensitivity of FCS that allows for interrogation specifically of low drug occupancy states. Here we demonstrate that the murine P-gp in nanodiscs exhibits nucleotide-dependent changes in affinity for BODIPY-verapamil (BD-verapamil) and BODIPY-vinblastine (BD-vinblastine), but the affinity of paclitaxel-Oregon Green 488 (Flutax-2) is unaffected by nucleotide. The chemical structures of each are shown in Figure 2.2 along with the corresponding unlabeled drug. Most interestingly, Flutax-2 is a transport substrate in murine P-gp vesicles but it does not stimulate ATPase activity in either lipid environment. Together the results confirm that P-gp in lipid nanodiscs has distinct ligand binding sites for commonly used fluorescent probes, at low occupancy, that are differentially coupled to nucleotide binding, and they demonstrate the utility of FCS with P-gp nanodiscs.

2.2 Materials and Methods

2.2.1 Materials

1,2-dimyristoyl-sn-glycero-3-phosphocholine (DMPC) and n-dodecyl-β-D-maltoside (DDM) were purchased from Avanti Polar Lipids. BODIPY FL verapamil (also known as Everfluor FL Verapamil) was purchased from Setareh Biotech. Oregon Green® 488 Paclitaxel (Flutax-2), BODIPY vinblastine, Alexa Fluor 488 succinimidyl ester and $DiOC_{16}(3)$ were purchased from ThermoFisher Scientific. Unless stated otherwise, nucleotides and other reagents were from Sigma-Aldrich.

2.2.2 P-gp and MSP1D1 Protein Expression and Purification

Hexa-histidine tagged MSP1D1 was expressed in *Escherichia coli* and purified via nickel affinity chromatography as described in detail previously (16). Briefly, MSP1D1 was expressed in *E. coli* BL21-Gold (DE3) cells transformed with a pET expression vector encoding kanamycin resistance with a C-terminal histidine tag and a TEV protease cleavage site. Cells were lysed using a French press followed by ultracentrifugation (45,000 g for 45 minutes) to separate intact cells and cell debris from the supernatant, and the supernatant was passed through a Ni-NTA column for purification. Pro-TEV Plus (Promega Corporation) was used to cleave the histidine-tag according to the established protocol, and cleaved MSP1D1 was further purified with another Ni-NTA affinity column, dialyzed into standard buffer (200 mM Tris, 100 mM NaCl, 0.5 mM EDTA, pH 7.4) before storing in aliquots at -80 °C.

The wild-type mouse P-gp mdr1a (or also known as mdr3) was expressed and purified from *Pichia Pastoris* as described previously with some modifications (17). Yeast cells were grown and induced with methanol in a 32 L DCI-Biolafitte fermentor with a 20 L working volume. Frozen, harvested cells were thawed before resuspension in an ice-cold homogenization buffer (100 mM Tris, 250 mM sucrose, 1 mM EDTA, 1 mM EGTA, 100 mM 6-aminohexanoic acid, 2 ug/ml pepstatin A, 2 ug/ml leupeptin, 1 mM PMSF, 2 mM benzamidine) at 0.5 mg cells/ml. Cells were lysed by French press and P-gp was solubilized in buffer containing 1% DDM (w/v) and protease inhibitors, purified by Ni-NTA and DEAE-cellulose chromatography according to established protocol, concentrated to 1mg/mL and stored in aliquots at -80 °C.

2.2.3 Nanodiscs Reconstitution and Purification

P-gp nanodiscs formation has been described previously (16). Instead of *E. coli* total lipid extract, DMPC was used to minimize heterogeneity in lipid composition and to increase the drug-stimulated over basal activity of murine P-gp. Briefly, DMPC lipid films were solubilized in disc forming buffer (20 mM Tris, 100 mM NaCl, pH 7.4) in presence of 6-fold excess DDM. Purified P-gp, MSP1D1 and lipid were mixed in a molar ratio of 0.1:1:80 and incubated for 1 hour at room temperature on a nutator. To remove the detergent, pre-washed Amberlite XAD2 resin (Sigma-Aldrich) was added at 0.6g/ml for 2 hours at room temperature, and P-gp nanodiscs were recovered by passing through a 25 Ga needle. P-gp nanodiscs were separated from empty nanodiscs by SEC-HPLC chromatography (Superdex 200 10/300 GL column, GE Healthcare). Fractions containing P-gp nanodiscs were collected and concentrated using a 100 kDa MWCO centrifugal filter unit (Millipore). P-gp nanodisc concentrations were estimated by comparing coomassie-stained P-gp bands with BSA standards of known concentration using SDS-PAGE.

2.2.4 ATPase Activity Assay

Basal and drug-stimulated ATPase activities of P-gp were measured using a colorimetric assay to monitor the release of inorganic phosphate according to Chifflet et. al. (18). P-gp nanodiscs (0.5 µg) were incubated in ATPase buffer (150 mM NH_4Cl, 50 mM Tris, 5 mM $MgSO_4$, 0.02% NaN_3, pH 7.4) in the presence of 1 mM MgATP for 1 hour at 37 °C. Drugs were added from concentrated DMSO stocks and final DMSO concentration did not exceed 1% (v/v). The absorbance intensity from the formation of phosphomolybdate was measured at 850 nm using a Tecan Infinite M200 microplate reader.

ATPase activity was measured as a function of drug concentration and rates were fit to the substrate inhibition equation as done for many P-gp studies, which assumes that there are two drug binding sites on P-gp, one which has high affinity and stimulates ATPase activity, and a second one which has low affinity and inhibits ATPase activity (19):

$$V = \frac{K_1K_2V_0 + K_2V_1S + V_2S^2}{K_1K_2 + K_2S + S^2}$$

where *V* is the overall rate of ATP hydrolysis, V_0 is the basal rate of ATP hydrolysis in the absence of drug, V_1 is the maximal rate of ATP hydrolysis when there is only activation, K_1 is the [substrate] that stimulates half of this maximal increase in ATPase activity, V_2 is the rate of ATP hydrolysis at infinite [substrate], and K_2 is the [substrate] that gives half maximal decrease in ATPase activity from the value V_1 to the value V_2.

2.2.5 Fluorescence Correlation Spectroscopy

FCS measurements were performed on a home-built instrument, consisting of an inverted Zeiss Axio Observer D1 (Carl Zeiss Microscopy, Peabody, MA) microscope equipped with HydraHarp 400 detection electronics, a pulsed 485 nm diode laser line, and a Tau-SPAD photon counting detector (PicoQuant GmbH, Berlin). Laser power was set at 150 uW to maximize signal to noise level and to minimize excitation saturation effects and photobleaching. The laser was passed through a 488/10 excitation filter and focused into the sample by a 63X/1.2 N.A. C-Apochromat water immersion objective. The resulting fluorescence signal of the sample was collected through the same objective and separated from the excitation light by a 488 nm dichroic mirror in combination with a 535/70 emission filter (all filters from Chroma Corp, Bellows Falls, VT). Emitted light was focused onto a 50 μm multimode fiber (OZ Optics, Ottawa, ON) and transmitted to the Tau-SPAD detector. Autocorrelation and time-correlated single-photon counting of fluorescence signal from the detector was performed using the HydraHarp 400 and SymphoTime 64 software (PicoQuant). Binding titrations were performed by adding increasing concentration of P-gp nanodiscs (receptor) to a fixed nanomolar concentration of the fluorophore (ligand). P-gp and empty nanodiscs were dialyzed in FCS buffer (20 mM Tris, 150 mM NaCl, 2 mM $MgSO_4$, 4% glycerol, pH 7.4) overnight and centrifuged at 17,500 rpm at 4°C for 15 minutes to remove any aggregates before use. A fixed amount of empty nanodiscs was added to minimize adsorption of fluorophores or P-gp to tubes and cover slips. For the data shown, 25 nM BD-verapamil was added to various P-gp nanodiscs concentrations in presence of 1 μM empty nanodiscs. Similarly, 25.7 nM Flutax-2 was added to P-gp nanodiscs in presence of 0.3 μM empty nanodiscs, and 50 nM BD-vinblastine was added to P-gp nanodiscs in presence of 0.3 μM empty nanodiscs. Effect of nucleotides on binding of drug-fluorophore to P-gp was characterized by adding 1 mM AMP-PNP, or 1 mM ATP with 240 μM Vi. Orthovanadate stock solutions (100 mM) were prepared from Na_3VO_4 (Calbiochem) with boiling at pH 10, and sub stocks were boiled for 5 minutes and diluted with FCS buffer before each use. Fluorophore concentrations were determined using $\varepsilon^M = 82{,}000 \pm 5000\ M^{-1}cm^{-1}$ at 506 nm for BODIPY dyes (ThermoFisher) and $49{,}100 \pm 1100\ M^{-1}cm^{-1}$ at 496 nm for Flutax-2 (20).

Competition experiments between the fluorescent probes and drug substrates for binding were carried out in the presence of a fixed concentration of P-gp nanodiscs (300 nM) and dye (as used for binding titrations). Drug stock solutions were made up in DMSO and final DMSO concentration in FCS samples did not exceed 1% (v/v).

Samples were incubated at room temperature (22.5 ± 0.5°C) for 90 minutes before measurement. 5-10 times of 1 minute measurements were recorded for each sample. Autocorrelation curves with intensity spikes due to aggregation or insolubility were removed. A one component, free diffusion model was used to describe the autocorrelation function ($G_{(\tau)}$) for single fluorescent molecules:

$$G(\tau) = \frac{1}{N}\left(1 + \frac{\tau}{\tau_D}\right)^{-1}\left(1 + \frac{\tau}{S^2\tau_D}\right)^{-\frac{1}{2}}$$

where N is the average number of molecules in the focal volume, τ_D is the translational diffusion time of the particles transiting the observation volume, and S (= Z_0/r_0) is the structure parameter which is the ratio of the axial (Z_0) to lateral dimension (r_0) of the volume (fixed at 5.0 for our instrumentation). For single component samples such as free dye alone or fully bound dye species to nanodiscs, the above equation was used to obtain τ_D. The laser point spread function was approximated by a three-dimensional Gaussian model and 20 nM of Alexa Fluor 488 succinimidyl ester was used for calibration and estimating the r_0^2 value ($r_0^2 = \tau_D * 4D$, where D is the diffusion coefficient of Alexa Fluor 488 SE which is reported to be 414 $\mu m^2/s$) (21). Fitting of autocorrelation curves was performed using Igor Pro 6, which uses the Levenberg- Marquardt nonlinear least squares fitting algorithm. The goodness-of-fit was derived from the χ^2 value or residual plot.

2.2.6 Equilibrium Binding of Fluorophores to P-gp Nanodiscs

To analyze a solution containing n non-interacting fluorescent species with n different τ_{Di}, the overall autocorrelation function is described as:

$$G(\tau) = \sum_{i=1}^{n} bi\left(1 + \frac{\tau}{\tau_{Di}}\right)^{-1}\left(1 + \frac{\tau}{S^2\tau_{Di}}\right)^{-\frac{1}{2}}$$

where S is the structure parameter (Z_0/r_0) and b_i is the relative amplitude of the components which is proportional to the concentration of molecules, assuming constant brightness of the molecules and contribution of chemical kinetic processes are negligible.

Here we used the approach of measuring a single, apparent τ_D, which is a weighted average of all the n components (free dye, empty nanodiscs, P-gp nanodiscs) in solution to determine the equilibrium dissociation constant, K_d

$$\tau_{D,app} = \frac{\tau_{free} + \tau_E \frac{[E]}{K_E} + \tau_P \frac{[P]}{K_P}}{1 + \frac{[E]}{K_E} + \frac{[P]}{K_P}}$$

where τ_{free}, τ_E, τ_P are the known translational diffusion times of the free fluorophore, empty nanodiscs and P-gp nanodiscs respectively, while [E] and [P], K_E and K_P are the concentrations and the dissociation constants of empty and P-gp nanodiscs respectively.

The concentrations of fluorophore and empty nanodiscs added to the samples were constant and fixed in the above equation, and non-specific binding to the empty nanodiscs was accounted for by determining K_E in a separate titration with empty nanodiscs alone. The dissociation constant of fluorophore binding to P-gp was obtained by plotting the apparent diffusion time vs. different P-gp nanodiscs concentrations, and independent data sets collected on different days were globally fitted.

To demonstrate that the FCS binding experiments selectively probe the high affinity site of P-gp, and that the above equation, which assumes a single binding site on P-gp is appropriate, simulations of the fractional occupancy at the high and low affinity sites were carried out using the following equation with Graphpad Prism 7, utilizing the parameters recovered from the fits of biphasic ATPase profiles of these probes as well as incorporating a component for non-specific binding to nanodiscs.

$$\text{Fractional Occupancy} = \frac{\frac{[\text{P-gp}]}{K_{D1}}}{1+\frac{[\text{P-gp}]}{K_{D1}}+\frac{[\text{P-gp}]}{K_{D2}}+\frac{[E]}{K_E}}$$

where K_{D1} and K_{D2} refers to the dissociation constants of the high and low affinity sites of P-gp, assuming that the K_M values for ATP hydrolysis derived from the activity assays are close approximates for the K_D values, and [high affinity sites] = [low affinity sites] = [P-gp].

The potencies of the drugs in competing for fluorophore binding to P-gp nanodiscs were assessed using the following non-linear regression derived from the Hill equation to determine the IC_{50} value:

$$\tau_{D,\mathrm{response}} = \tau_{\mathrm{Base}} + \frac{(\tau_{\mathrm{Max}} - \tau_{\mathrm{Base}})}{1 + \left(\frac{[\mathrm{Drug}]}{IC_{50}}\right)^{n}}$$

where τ_{Max} and τ_{Base} refer to the apparent diffusion times of the fluorophore when it is maximally bound to P-gp nanodiscs or when it is unbound, and η is the Hill coefficient.

2.2.7 Vesicle-based Transport Assay of Flutax-2

Transport of Flutax-2 was evaluated using inside-out membrane vesicles containing human or murine P-gp (GM0015 or GM0004 from GenoMembrane). The assay made use of an anti-Fluorescein antibody (anti-FL IgG; Thermofisher) that is membrane impermeant to quench the fluorescence of free Flutax-2 in solution but not Flutax-2 transported into vesicles. Fluorescence measurements were performed using a Varian Cary Eclipse spectrophotometer with a temperature-controlled sample compartment. A 75 µl aliquot of membrane vesicles containing 50 µg protein was pre-incubated with 133 nM Flutax-2 in transport buffer (20 mM Tris, 150 mM NaCl, 5 mM $MgSO_4$, pH 7.4) at 37°C for 5 minutes. To initiate transport, a 10 µl aliquot of ATP or AMP-PNP (control) was added by mixing for 10s (effective concentration 4.7 mM). At various time points, a 15 µl aliquot of anti-FL IgG (1mg/ml stock) was added with 10s mixing to rapidly quench the fluorescence of Flutax-2 remaining outside of vesicles and fluorescence readings were collected immediately. The final concentrations of reagents after addition of anti-FL IgG were 100 nM Flutax-2, 4 mM nucleotide and 1 µM anti-FL Ab. A control experiment with 100 nM Flutax-2 and 1 µM anti-FL Ab demonstrated that up to 90% of fluorescence quenching was achieved within first few seconds of mixing, in agreement with another study (20). Excitation was set at 495 nm (5 nm slit width) and emission was recorded from 510 to 650 nm (10 nm slit width). Data was collected at 1 nm interval and a single measurement was completed within 30 seconds. Since changes in fluorescence intensity were proportional to the dilution factor, the initial rate of ATP-dependent transport was approximated by taking the difference between the fluorescence intensity in presence of ATP and AMP-PNP after antibody quenching, scaling it to the fluorescence intensity for 100 nM Flutax-2 in presence of vesicles, and dividing by the amount of protein used and reaction time (adapted from GenoMembrane protocol). We recognized that more free dye remaining in AMP-PNP-containing incubations would result in different extent of quenching by antibody, so the subtraction method may be an underestimate of the rate of transport of Flutax-2.

Initial rate of transport (calculated from the first 2 or 3 time points contributing to linear phase) =

$$\frac{\text{Difference in fluorescence intensity (ATP-AMPPNP)}}{\text{Total fluorescence intensity}} \times \frac{\text{Amount of substrate in reaction medium (mole)}}{\text{Amount of protein (mg)} \times \text{Reaction time (min)}}$$

2.2.8 Homology Modelling

For illustrative purposes, we constructed a homology model of P-gp in the outward facing conformation based on crystal structures of the homodimeric bacterial ABC transporter SAV1866. Using the I-TASSER server (22) , N-terminal (residues 1–628) and C-terminal (residues 689–1280) portions of the human P-gp sequence were separately modeled with an AMP-PNP-bound crystal structure of SAV1866 (PDB ID: 2ONJ) specified as the primary template and the inward-facing murine P-gp structure (PDB ID: 4M1M) excluded as a template. This yielded models for the N- and C-terminal halves of P-gp that were then aligned with the 2ONJ crystal structure so as to provide an outward-facing model of P-gp (excluding residues 629–688). This model should be considered a rough approximation of the overall conformation of P-gp and possible inter-helical contacts in one of many outward-facing states, rather than as an atomically precise structure.

2.3 Results

2.3.1 Reconstitution of Mouse P-gp in DMPC Nanodiscs

Previously published results have demonstrated the utility of incorporating human P-gp into nanodiscs with *E. coli* mixed lipids (15,16). However, attempts to reconstitute human P-gp into DMPC nanodiscs were unsuccessful. Surprisingly, murine P-gp, which is 87 % identical to human P-gp, reconstitutes readily into DMPC nanodiscs using MSP1D1 as scaffold protein (Figure 2.3). Size exclusion chromatography and electrophoresis demonstrate that the final P-gp nanodiscs are highly purified, with a ratio of MSP1D1 scaffold : P-gp of 1.6:1 for the pooled fractions used (Figure 2.3). The theoretical ratio is 2:1. A significant advantage of the DMPC nanodiscs is their increased homogeneity and reproducibility compared to nanodiscs made with *E. coli* lipid extracts.

2.3.2 ATPase Activity of P-gp Nanodiscs with Probe Substrates

Although fluorescent analogs of probe drugs are used widely in cell-based assays to assess P-gp transport activity, their biochemical characterization is reported in only a few cases, and steady state kinetic parameters and binding constants are particularly sparse for the murine P-gp. Therefore, we determined the concentration dependence of BD-verapamil, BD-vinblastine and Flutax-2 in standard ATPase assays, in comparison to the corresponding unlabeled drugs (Figure 2.4). For each, the data were fit to a velocity equation that includes P-gp that is singly- or doublybound with substrate, as described in Methods. Whereas BD-verapamil and BD-vinblastine are known substrates for murine P-gp and human P-gp, biochemical data for Flutax-2 with murine P-gp have not been reported. The recovered parameters are summarized in Table 2.1. Consistent with findings that smaller molecules tend to be more stimulatory and larger molecules tend to bind more tightly with lower ATPase stimulation (23), BD-Verapamil and BD-vinblastine exhibit lower K_{MS} for both sites compared to their unlabeled analogs. BD-verapamil and BD-vinblastine stimulate ATP hydrolysis ~8-fold and ~2-fold over basal ATPase activity, respectively. Interestingly, BD-vinblastine is much less stimulatory than vinblastine. The K_M values for high affinity sites that stimulate ATP hydrolysis are in the range 77-330 nM, which are significantly below the corresponding high affinity K_M values for verapamil or vinblastine, suggesting tighter binding of BD-verapamil and BD-vinblastine. Also, both BD-verapamil and BD-vinblastine exhibit clear substrate inhibition with respect to ATPase activity, as observed for many drugs and probe substrates at higher concentrations. In contrast, Flutax-2 does not stimulate ATPase activity and modestly inhibits basal ATPase activity at concentrations approaching the low affinity K_M for paclitaxel.

For comparison, we also studied the stimulation of ATPase activity for each probe substrate with P-gp in *E. coli* lipid nanodiscs. The results are summarized in Table 2.1. Although the basal ATPase activity is higher in the *E. coli* lipid nanodiscs, the concentration-dependent effects of the three probes on ATPase activity are qualitatively similar in E. coli lipid nanodiscs as in DMPC nanodiscs. Flutax-2 exhibits no stimulation in either lipid environment. Neither BD-Vinblastine nor Flutax-2 stimulated ATPase activity in *E. coli* lipids. In fact both BD-Vinblastine and Flutax-2 are low affinity inhibitors that decrease the ATPase activity more in the *E. coli* lipid than in the DMPC nanodiscs (Figure 2.4).

In summary, the three probe ligands behave differently from one another in a lipid-dependent manner, and from their corresponding non-fluorescent analogs but, in particular, Flutax-2 is distinct in its inability to stimulate ATP hydrolysis in either case. We note that the value for K_2 with paclitaxel includes a high level of error because of insufficient data points at higher concentrations. This was due to the solubility limits of paclitaxel that prohibited the use of higher concentrations. Similarly, there is significant error in the K_1 values for the *E. coli* lipid nanodiscs, because of minimal activation. Although we acknowledge the error, the data still demonstrate substrate inhibition for paclitaxel in DMPC and a behavior distinctly different from that of BD-verapamil in *E. coli* lipid nanodiscs. We are careful not to overinterpret the recovered parameters, but they clearly indicate that Flutax-2 behaves differently with respect to the other ligands in DMPC nanodiscs and differently with respect to BD-verapamil in *E. coli* lipid nanodiscs.

2.3.3 Fluorescence Correlation Spectroscopy and Binding of Fluorescent Probe Substrates at Low Occupancy

In order to obtain more detail about the behavior of the fluorescent probes observed in fluorescent transport assays, we measured equilibrium binding affinities for each using FCS. This method is based on a shift in the diffusion times of the free probe when it binds to a P-gp nanodisc that has a much slower rate of diffusion. The P-gp nanodisc system is uniquely suited for FCS. In contrast, P-gp liposomes are not optimal because they provide a heterogeneous population of particles with different sizes, and hence different diffusion properties, and a large membrane reservoir for nonspecific binding of probe ligands. Also, an important distinction between FCS and other fluorescence based methods to monitor binding, is that FCS does not require a change in fluorescence intensity or emission wavelength associated with binding. The diffusion constants are independent of the intensity. The experimental design is a reverse titration in which increasing concentrations of P-gp nanodisc are added to a low, fixed, concentration of dye, and this selectively probes the tightest binding interaction between P-gp and ligand, without significantly populating the low affinity site(s).

Before monitoring the binding of fluorescent probes to the high affinity sites of P-gp in nanodiscs, it was necessary to calibrate the diffusion times of empty nanodiscs and P-gp nanodiscs, in order to account for any binding of probe to the lipid bilayer of the nanodisc. This was accomplished by incorporating trace amount of DiOC$_{16}$(3) into empty nanodiscs and also into P-gp nanodiscs in the molar ratio of 1:160 (dye to lipid) to determine the diffusion properties of nanodiscs with or without P-gp. The autocorrelation curves fit well to the one-component model and the average diffusion times of empty and P-gp nanodiscs were 1.71 ± 0.07 ms (n=5) and 3.02 ± 0.18ms (n=12), respectively (Figure 2.5). These values were used in subsequent experiments in which P-gp nanodiscs were titrated into solutions of BD-verapamil, BD-vinblastine or Flutax-2.

The addition of P-gp nanodiscs to solutions of each fluorescent probe, in the absence of nucleotide, resulted in concentration-dependent shifts in their diffusion times as shown in Figure 2.6.

In addition, we monitored the binding of each fluorophore to empty nanodiscs. At the concentrations used, BD-verapamil exhibited negligible binding to the lipid nanodiscs whereas Flutax-2 and BD-vinblastine yielded apparent K_D value of 3.6 μM and 1.7 μM respectively, which is more than an order of magnitude higher than the K_D's recovered for the tight binding site on P-gp in each case. A comparison of binding to P-gp nanodiscs versus empty nanodiscs is shown for each dye in Figure 2.7. In binding experiments with P-gp nanodiscs, the P-gp nanodisc-induced shift in fluorophore diffusion time was corrected for the membrane partitioning of the dye, as described in Materials and Methods, to obtain an apparent K_D specifically for binding to P-gp. The recovered values are listed in Table 2.2. The fact that the limiting values of τ in the binding isotherms of Figure 2.6 do not reach the theoretical limit of the bound diffusion time ($\tau \sim 3$ ms) likely arises from some impurity or heterogeneity of the dye in solution, wherein a fraction of fluorescent species that contribute to τ do not bind. Also, it is important to emphasize that with this experimental design, in which P-gp nanodiscs are titrated into a limiting concentration of probe, to a first approximation only the highest affinity site is occupied throughout the titration. Higher occupancy states are minimally populated. This is demonstrated with simulated binding isotherms based on the experimentally determined K_D values and the experimental condition, in Figure 2.8.

The binding affinity of each probe was determined also in the presence of a saturating concentration of AMP-PNP, which is a non-hydrolyzable analog of ATP, and in the vanadate-trapped state. The vanadate-trapped state is widely used to mimic the post hydrolysis transition state or the transition state (24,25). It is established that binding of AMP-PNP or vanadate trapping leads to a shift in the conformational ensemble towards an outward-facing conformation with NBDs in close proximity to one another, and with rearrangement of the TMHs. These nucleotide-bound states are expected to be predominantly outward facing, although likely different from one another and possibly are drug dependent and isoform dependent (6,26,27).

These results included interesting complexity. We observed that addition of P-gp nanodiscs to BD-verapamil or BD-vinblastine, but not Flutax-2, is accompanied by an increase in fluorescence intensity. Therefore, we investigated whether the observed increase in fluorescence intensity was due to a change in the quantum yield of BD-verapamil or BD-vinblastine upon binding to Pgp or nanodiscs. Since FCS measures apparent number of fluorescent particles in addition to hydrodynamic radius, we are able to determine the apparent molecular brightness from single-component fits.

For a two-component system where the brightness per molecule changes due to binding over the course of a titration, the apparent number of molecules is described by:

$$N_{app} = \frac{(f\left(\frac{Q2}{Q1}\right)N + (1-f)N)^2}{(f(\frac{Q2}{Q1})^2 + (1-f))N}$$

where Q_2/Q_1 is the ratio of quantum yields of the species, f is the molar fraction of species 2, and N is the true number of fluorescent molecules in the experimental focal volume, on average. The apparent number of molecules decreases over the course of a binding titration, before returning to N as binding is saturated as in Figure 2.9a. Correspondingly, the apparent brightness per molecule (i.e., the ratio of the measured intensity to N_{app}) also changes over the course of the titration, with the final value corresponding to the molecular brightness of the fully-bound species, according to this equation:

$$N_{app} = \frac{\left(\frac{Q2}{Q1} + (1-f)\right)(f(\frac{Q2}{Q1})^2 + (1-f))}{(f\left(\frac{Q2}{Q1}\right) + (1-f))^2} = \frac{(1-f) + f(\frac{Q2}{Q1})^2}{(1-f) + f(\frac{Q2}{Q1})}$$

In other words, the overall brightness is predicted to change linearly with fraction bound, while the apparent brightness per molecule is predicted to change asymptotically and more rapidly. Figure 2.9b shows the change in both quantities for the case $N = 1$ and $Q_2/Q_1 = 4$. Fitting the experimentally observed changes in B/Napp to the above equation indicate that there is no evidence for a significant change in molecular brightness (F-test: $P > 0.4$ for both compounds) as in Figure 2.9c. Therefore, the brightness per molecule did not change with an increasing fraction bound (*f*), but the data indicate that increasing the concentration of P-gp nanodiscs leads to a change in the apparent N_{app}. The change in N_{app} likely results from the recruitment of BD-verapamil or BD-vinblastine from weak nonspecific binding sites on the glass surfaces to the experimental focal volume upon binding. As a result of this complexity, the reported K_D values are apparent K_D's and should be considered as relative values.

Regardless of this complexity, the results, with binding parameters summarized in Table 2.2, clearly demonstrate that BD-verapamil and BD-vinblastine have decreased affinity for their high affinity site in the vanadate-trapped state, with increases in K_D of 10.3-fold and 6.8-fold respectively. Interestingly, the results with AMP-PNP are more substrate-dependent when comparing BD-verapamil vs. BD-vinblastine. With BD-verapamil, addition of AMP-PNP induces a 5.1-fold increase in $K_{D,}$ but only a 1.9-fold increase in K_D for BD-vinblastine. Furthermore, the results with Flutax-2 suggest a very different behavior. Specifically, the high affinity binding of Flutax-2 is relatively insensitive to the AMP-PNP binding or to vanadate trapping. This result was examined in greater detail below.

2.3.4 Competition of the High Affinity Site for Flutax-2 with Other Probes

It is reported that Flutax-2 is a transport substrate for human P-gp, but no additional characterization has been reported (28). Because Flutax-2 exhibited a high affinity interaction with the murine P-gp ($K_D = 519$ nM), with no effect on ATPase activity in this concentration range, we hypothesized that Flutax-2 binds at a site distinct from drugs that stimulate ATPase activity. Therefore, we performed competition experiments to determine whether it binds competitively with verapamil or vinblastine. For comparison we also determined whether BD-verapamil and BD-vinblastine bind competitively with these substrates. In separate experiments, each fluorescent probe was poised at a concentration (25-50 nM) that partially saturated the high affinity site on P-gp, in the presence of excess P-gp nanodisc (300 nM), and each nonfluorescent drug was titrated into the sample. As the nonfluorescent drug displaces the fluorescent dye, the apparent diffusion time of the dye decreases. This approach revealed whether each dye was competitively displaced by each drug. Results for the titration of verapamil or vinblastine into solutions containing the complexes [P-gp nanodisc • BD-verapamil], or [Pgp nanodisc • Flutax-2] are shown in Figure 2.10 and Figure 2.11, and the results for each of the dye combinations is summarized in Table 2.3.

For vinblastine and paclitaxel binding, the data did not fit to a simple 1:1 binding isotherm and a Hill equation was used. Hill coefficients of ~0.5 were recovered for vinblastine and paclitaxel binding to P-gp complexed with BD-vinblastine, consistent with multiple binding of these drugs. For verapamil binding to the BD-verapamil complex with P-gp, the recovered Hill coefficient was 0.95, suggesting that the binding of multiple verapamil molecules occurs with similar sequential K_D values and no cooperativity. Whereas vinblastine and verapamil each displaced BD-verapamil, paclitaxel did not displace it. Furthermore, vinblastine and paclitaxel each displaced BD-vinblastine, but verapamil did not. These results are consistent with previous models that suggest multiple, partially overlapping drug binding sites in P-gp (29,30), although a detailed molecular model for the binding sites was not pursued here. However, the results demonstrate the ability of the FCS approach to monitor overlapping or competitive binding sites. Most striking is the fact that none of the drugs displaced Flutax-2 from its high affinity site, indicating that it does not overlap substantially with verapamil, vinblastine or paclitaxel high affinity sites. Flutax-2 does not compete for the binding sites of vinblastine, verapamil or paclitaxel.

2.3.5 Transport of Flutax-2

Whereas some probes are known to be both transport substrates for P-gp and stimulate ATP hydrolysis, there are some that are transported despite the lack of ATPase stimulation (31). Because Flutax-2 exhibited high affinity for P-gp without having any effect on ATPase activity, we determined whether it is a transport substrate for murine P-gp. The human P-gp has been reported to actively transport Flutax-2 but the corresponding experiments with the murine protein have not been reported (28). Murine P-gp vesicles were used as described in Methods and we exploited anti-Fluorescein antibody (anti-FL IgG) to monitor the concentration of Flutax-2 remaining outside the vesicles after the addition of ATP or AMPNP. The anti-FL IgG added at various times quenches the fluorescence of free Flutax-2 but not the Flutax-2 that is transported to the inside of the vesicle. As a result, the fluorescence intensity remaining after addition of ATP and anti-FL-IgG represents the Flutax-2 that is transported. For comparison, we also measure the transport of Flutax-2 by human P-gp vesicles. The results are shown in Figure 2.12. Both human and murine P-gp clearly transport Flutax-2 in an ATP dependent process, with similar initial transport rates of approximately 51 pmol/mg total protein/min and 42 pmol/mg total protein/min respectively.

In light of the combined results that indicate that Flutax-2 is transported (Figure 2.12) but its binding is unaffected by nucleotide (Figure 2.6) we considered whether Flutax-2 stimulated ATPase activity in the Genomembrane system. We performed ATPase assays in both mouse and human P-gp vesicles and the results are shown in Figure 2.13. Whereas verapamil exhibited substrate inhibition with a maximal apparent 1.4-fold stimulation of ATPase activity in both human and mouse P-gp vesicles, Flutax-2 did not stimulate ATPase activity in the concentration range studied.

Finally, we note that there is apparent binding of Flutax-2 to the vesicles, distinct from transport, based on the background fluorescence in the samples containing AMP-PNP (Figure 2.12, insets). In order to determine whether this resulted from some background P-gp transport that was insensitive to AMPPNP, we also examined the effect of vanadate trapping (Figure 2.14). Vanadate trapping, like AMP-PNP, completely inhibited the time dependent increase in fluorescence without decreasing the time independent background fluorescence.

2.4 Discussion

The results described here contribute to three aspects of P-gp research. The first aspect is the demonstration that murine P-gp can be functionally reconstituted into lipid nanodiscs with DMPC. This is interesting because our attempts to reconstitute human P-gp into DMPC nanodiscs have not been successful, despite successful incorporation into nanodiscs made from *E. coli* lipid extract. It is established that the mouse P-gp and human P-gp have distinct lipid requirements (32), but it is difficult to predict how efficiently various membrane proteins can be incorporated into nanodiscs. So, we considered the possibility that the murine P-gp could be successfully incorporated into nanodiscs with DMPC. The verapamil-stimulated and vinblastine-stimulated ATPase activities of the murine P-gp nanodiscs are nearly identical to previously published results for P-gp in membranes or detergent solution (33,34). Moreover, larger molecules such as BD-verapamil and BD-vinblastine have higher affinity for P-gp than the unsubstituted drugs verapamil or vinblastine and this further confirms the catalytic and conformational integrity of the P-gp in this lipid environment. As noted elsewhere, incorporation of membrane proteins into lipid nanodiscs enables the application of several biochemical techniques that are difficult or impossible in other membrane platforms (35-37). The ability to reconstitute mouse P-gp into lipid nanodiscs allows for the application of new approaches to its characterization.

The second contribution of this work is the application of FCS to characterize P-gp, which is uniquely enabled by the nanodisc platform. FCS is particularly useful because many *in vitro* probes of P-gp transport are fluorophores. In fact many *in vitro* transport assays utilize fluorescence to monitor uptake into cells, via flow cytometry or fluorescence microscopy. However, understanding the specific interactions of these probes with P-gp requires purified preparations and different methods, and FCS provides some advantages. Neither detergent-solubilized preparations nor proteoliposomes are expected to be optimal with FCS due to heterogeneity in micelle or liposome dimensions. The monodisperse P-gp nanodiscs with a single P-gp per particle, and with both NBDs and cytosolic drug binding sites accessible to solution, are optimal for FCS. FCS provides a previously unexploited approach to characterize the interactions of commonly used fluorescent transport probes with P-gp and hence to better relate biochemical parameters to transport behavior. One potential advantage of FCS is that it does not rely on changes in emission intensity of ligand fluorescence or P-gp intrinsic fluorescence. Fluorescent probes that undergo no change in emission intensity can be studied by FCS. An additional significant advantage of the FCS is its high sensitivity, which requires minimal amounts of pure protein and allowed for the specific interrogation of low occupancy states of P-gp in the studies presented here.

The third aspect of P-gp research that is expanded here concerns the additional detail of its interactions with probe substrates revealed by the combination of FCS with functional activity assays. It is well established that drugs and modulators differentially couple ATP hydrolysis by P-gp to transport, and that nucleotides may also alter drug affinity to P-gp. Among the studies that have explored the functional linkage between drug binding sites and NBDs, nucleotide analogs yield variable effects on drug affinity when comparing different drug analogs. For example, 'classic' studies indicate that the ATP-vanadate trapped P-gp has lower affinity for the photo-affinity analog of prazosin, whereas another study showed that nucleotide binding, even in the absence of ATP hydrolysis, is capable of lowering drug affinity (12,14). Despite these, and other, elegant studies by a range of investigators, the mechanism by which drug binding is coupled to transport is not completely defined, and there may be drug-dependent mechanisms. Whereas BD-verapamil and BD-vinblastine interactions have been studied with human P-gp in various biological systems (38,39), their nucleotide-dependent interactions with murine P-gp have not been described under any conditions to the best of our knowledge. As noted above, the results for interactions of murine P-gp in nanodiscs with verapamil and vinblastine were consistent with previous studies in other lipid or detergent systems, thus validating the utility of the FCS and nanodisc platform. Specifically, AMP-PNP bound and vanadate trapped-P-gp demonstrate a 5- and 10-fold reduction in affinity for BD-verapamil respectively, compared to a 1.5- and 3.5-fold reduction in affinity for BD-vinblastine. The results for BD-verapamil and BD-vinblastine support the well-known behavior of P-gp, wherein the equilibrium affinity of drugs may be decreased in the presence of nucleotides, but the magnitude of the decrease in affinity can be drug-dependent and nucleotide-dependent. Addition of AMP-PNP to the complex of BD-vinblastine with human P-gp is sufficient to 'release' drug (39) but here the nucleotide causes an increase in K_D for BD-vinblastine of only 2-fold.

The human P-gp transports Flutax-2 in cell-based systems but its binding affinity for any P-gp has not been determined. Interestingly, Flutax-2 is distinct from the other probes or substrates studied here, inasmuch as it causes no detectable stimulation of ATP hydrolysis when bound to its high affinity site and only inhibits modestly at higher concentrations that approach the low affinity K_M for verapamil. Presumably, the transport of Flutax-2 that we observe requires the well-established conformational switching of Pgp, without formation of the same 'NBD dimer' conformation that hydrolyzes ATP at accelerated rates observed with other substrates. The combined results demonstrate that Flutax-2 binds with high affinity to murine P-gp at a site that is distinct from verapamil, paclitaxel or vinblastine. Based on the transport results, two possibilities are evident. Either the high affinity Flutax-2 binding site is not coupled to ATP hydrolysis, but nucleotide dependent switching between inward-facing and outward-facing conformations still occurs, without an increase over basal ATP hydrolysis, and Flutax-2 is able to dissociate from the outward facing conformations even though its affinity is not decreased. Alternatively the transport observed in our assay with vesicles occurs from P-gp complexes with multiple Flutax-2 molecules bound. Possibly, nucleotides do lower the affinity of Flutax-2 at high stoichiometry's of Flutax-2:P-gp, which are not probed in our FCS experiments, and this would facilitate transport. However, even if this occurs, it does so without stimulation of ATP hydrolysis, based on the lack of Flutax-2 effect on ATP hydrolysis even at high concentrations. On the basis of gel electrophoresis (not shown) we estimate that the transport assays contained 150 - 200 nM P-gp, similar to the level of P-gp expression in vesicles reported by others (40). With 117 nM Flutax-2 in the assays, and dramatically different K_D values for the first and second Flutax-2 binding sites, this would be expected to result in minimal P-gp with multiple Flutax-2 molecules bound in the transport assays. Therefore, it is unlikely that the observed transport requires multiple Flutax-2 binding, and we propose that the first possibility is operative. Apparently, binding to this high affinity site is not coupled to ATP hydrolysis but it allows for transport. Flutax-2 is among the murine P-gp transport substrates that do not stimulate ATP hydrolysis. The combined results are summarized in Figure 2.15, which emphasizes the similarities and differences between the probes studied here.

Figures

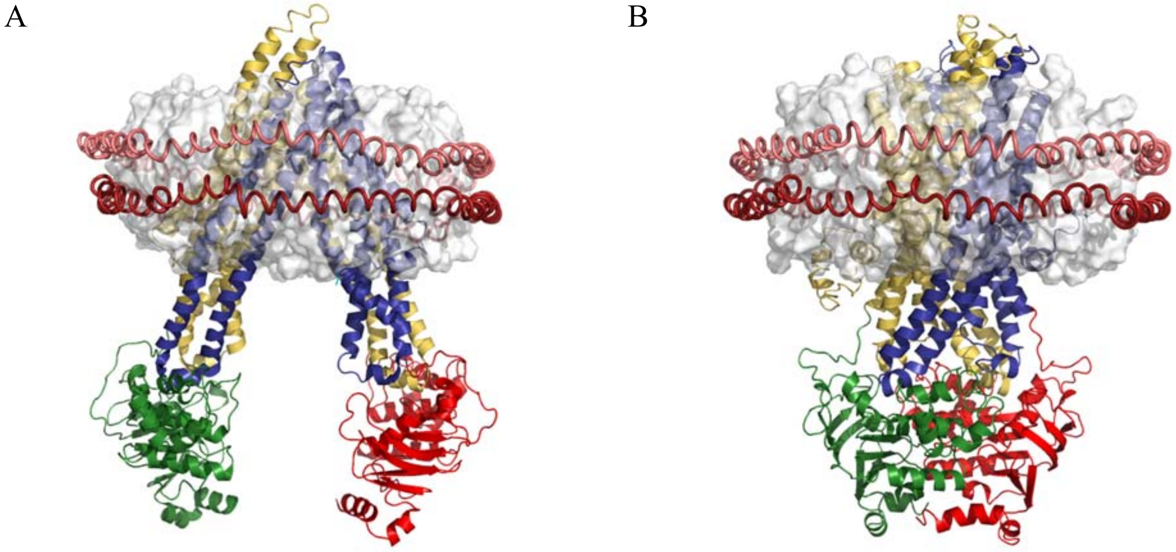

Figure 2.1. P-gp in inward facing and outward facing conformations. A) Crystal structure of apo murine P-gp (PDB ID: 4Q9H) and B) illustrative homology model of human P-gp (see Materials & Methods) manually docked with a discoidal HDL model. Colored segments are: transmembrane domains 1 (yellow) and 2 (blue); nucleotide binding domains 1 (green) and 2 (red). The OPM database (10) was used for the spatial arrangement of P-gp with respect to the lipid bilayer (white). The red helical peptides around the lipid bilayer represent the MSP protein of the nanodisc.

Verapamil

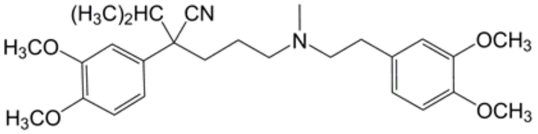

BD-Verapamil

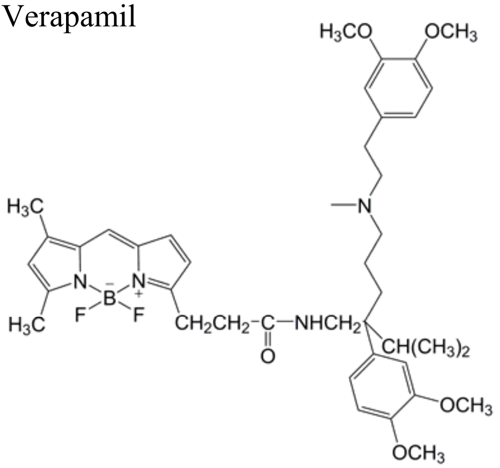

Vinblastine

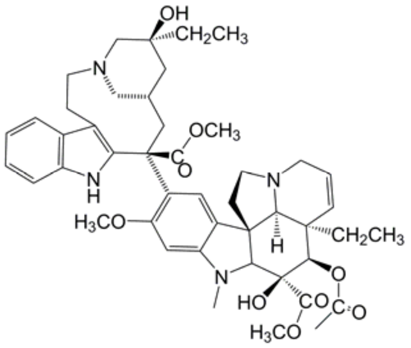

BD-Vinblastine

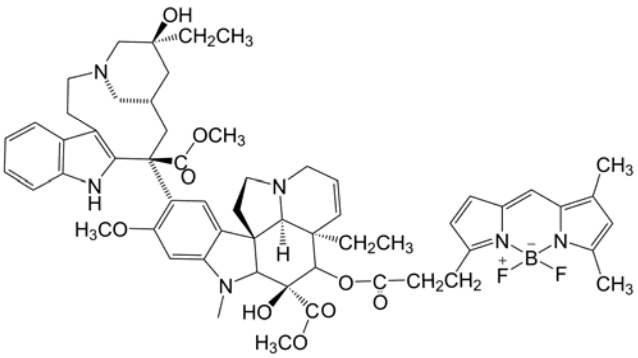

Paclitaxel

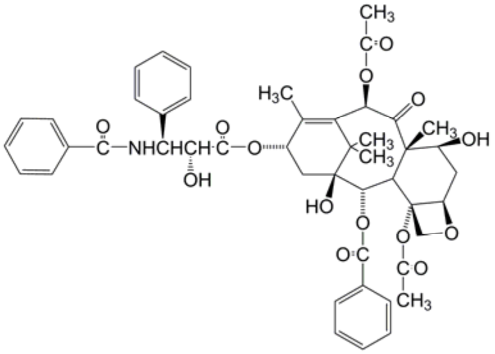

Flutax-2

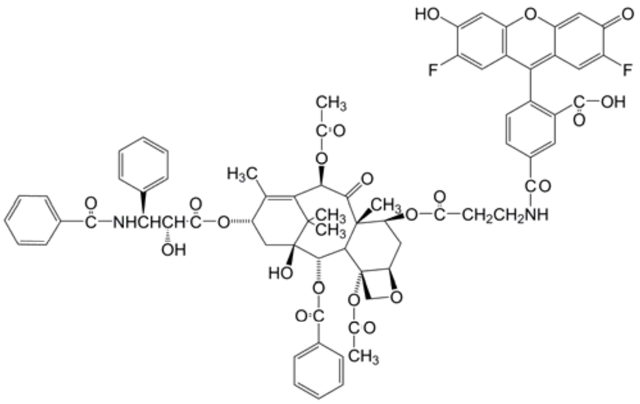

Figure 2.2. Chemical structures of the drugs and their fluorescent analogs used in this work.

A

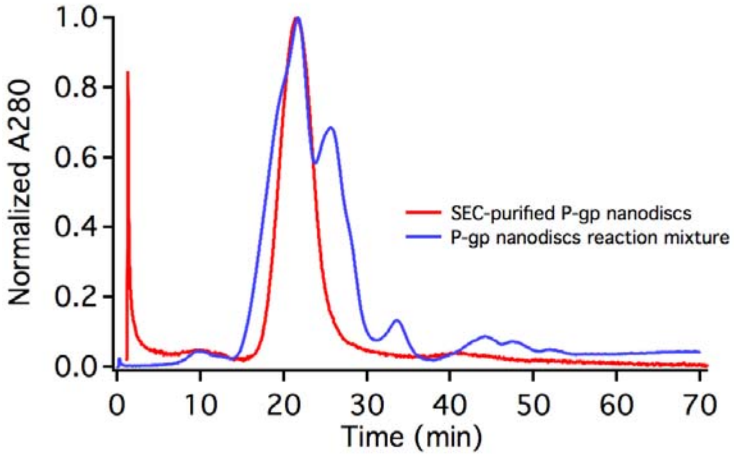

B

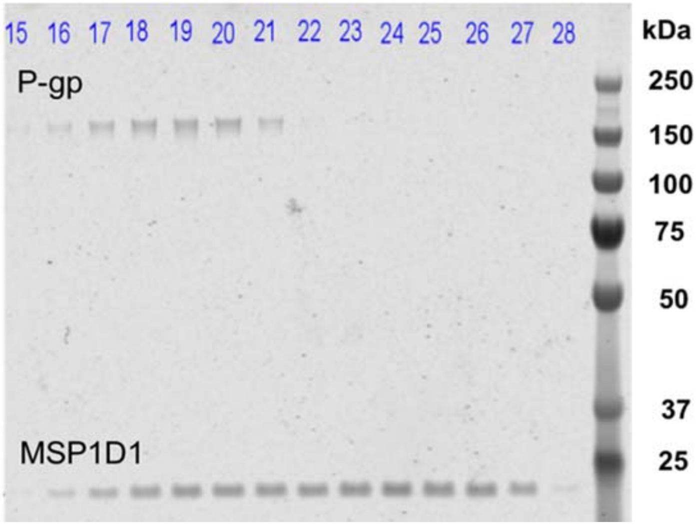

Figure 2.3. Separation of P-gp embedded nanodiscs from empty nanodiscs. A) SE-HPLC elution profile of nanodiscs reconstitution mixture (blue) and purified P-gp nanodiscs (red). B) Visualization of eluted fractions of nanodiscs reconstitution mixture from 15 to 28 minutes, by Coomassie staining of reducing SDS-PAGE. Fractions containing P-gp that co-eluted with histidine-tag cleaved MSP1D1 were pooled together (fractions 17 to 20) and concentrated using a 100 kDa MWCO spin filter.

Table 2.1. Kinetic parameters for substrate inhibition (two binding sites) of ATPase activity with drugs and fluorescent analogs

	V_1 (nmol P_i/min/mg)	V_2 (nmol P_i/min/mg)	K_1 (μM)	K_2 (μM)
		DMPC Nanodiscs		
Verapamil	1004 ± 160	> 0 [a]	55.7 ± 14.8	118.9 ± 38.8
BD-Verapamil	492 ± 10	107 ± 13	0.08 ± 0.008	12.1 ± 1.6
Vinblastine	276 ± 31	> 0 [a]	2.6 ± 1.0	40.1 ± 9.7
BD-Vinblastine	105 [b]	21 ± 4	0.04 ± 0.01	0.7 ± 0.1
Paclitaxel	199 ± 23	48 ± 6	1.3 ± 0.5	16.3 ± 24.7 [c]
Flutax-2	65 [b]	18 ± 2	0.3 ± 0.7 [d]	13.8 ± 3
		***E. coli* Lipid Nanodiscs**		
BD-Verapamil	627.5 ± 11.2	218.4 ± 223.9	0.07 ± 0.02	113.5 ± 118.4 [c]
BD-Vinblastine	465 [b]	156.5 ± 24.8	0.05 ± 0.1 [d]	1.1 ± 0.4
Flutax-2	500 [b]	33.2 ± 46.8	0.2 ± 0.3 [d]	2.6 ± 0.9

[a] denotes parameter reaching constraint set at greater than 0. [b] denotes parameter held at a constant value. [c] Large errors due to modest inhibition at the highest drug concentration used. [d] Ambiguous,because of a lack of ATPase stimulation by these ligands (V_1 is close to V_0) Fits for the DMPC nanodiscs and *E. coli* nanodiscs with three probes are shown in Figure 2.4.

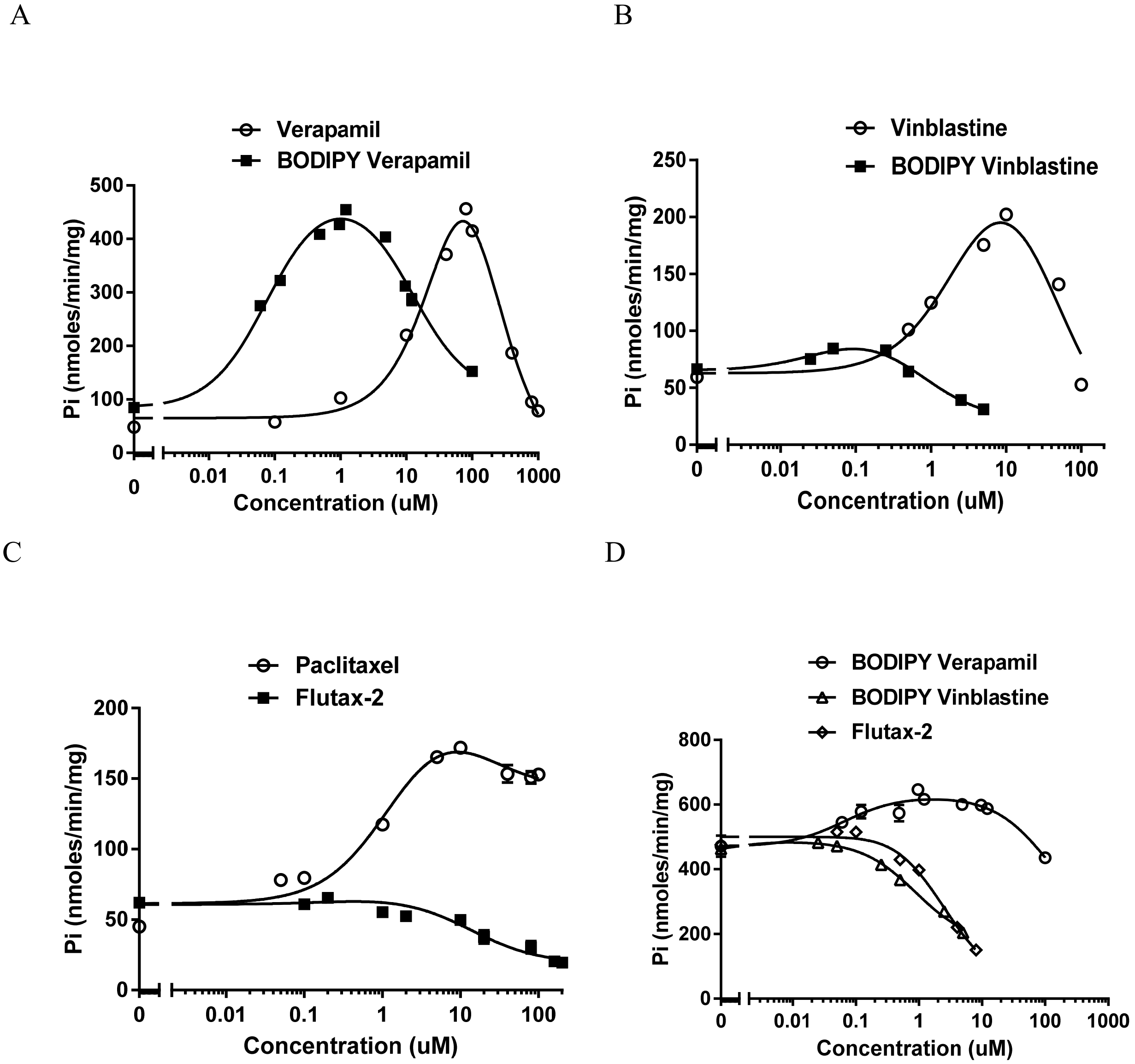

Figure 2.4. Modulation of ATPase activity of P-gp by drugs and fluorescent analogs. P-gp DMPC nanodiscs (0.5 µg), in presence of 1 mM ATP, were used for ATPase activity assays with ligands (A-C). A) ○ Verapamil and ■ BD-verapamil; B) ○ Vinblastine and ■ BD-Vinblastine C) ○ Paclitaxel and ■ Flutax-2. D) Effect of fluorescent probes on the ATPase activity of P-gp reconstituted into *E. coli* nanodiscs. See (16) for details on *E. coli* lipid nanodiscs reconstitution. Each data point represents mean ± standard deviation of triplicates.

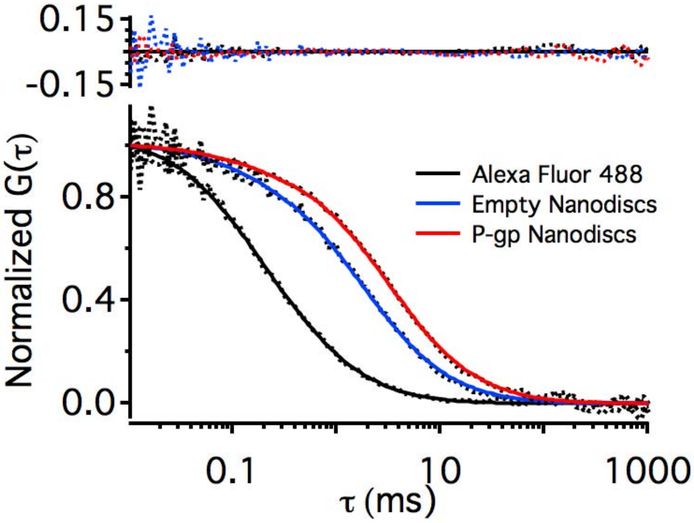

Figure 2.5. Calibration of diffusion times for free dye (Alexa fluor 488), empty nanodiscs labeled with DiOC16 and P-gp nanodiscs labeled with DiOC16. The autocorrelation curves yielded the diffusion time of each species reported in the main body of the manuscript.

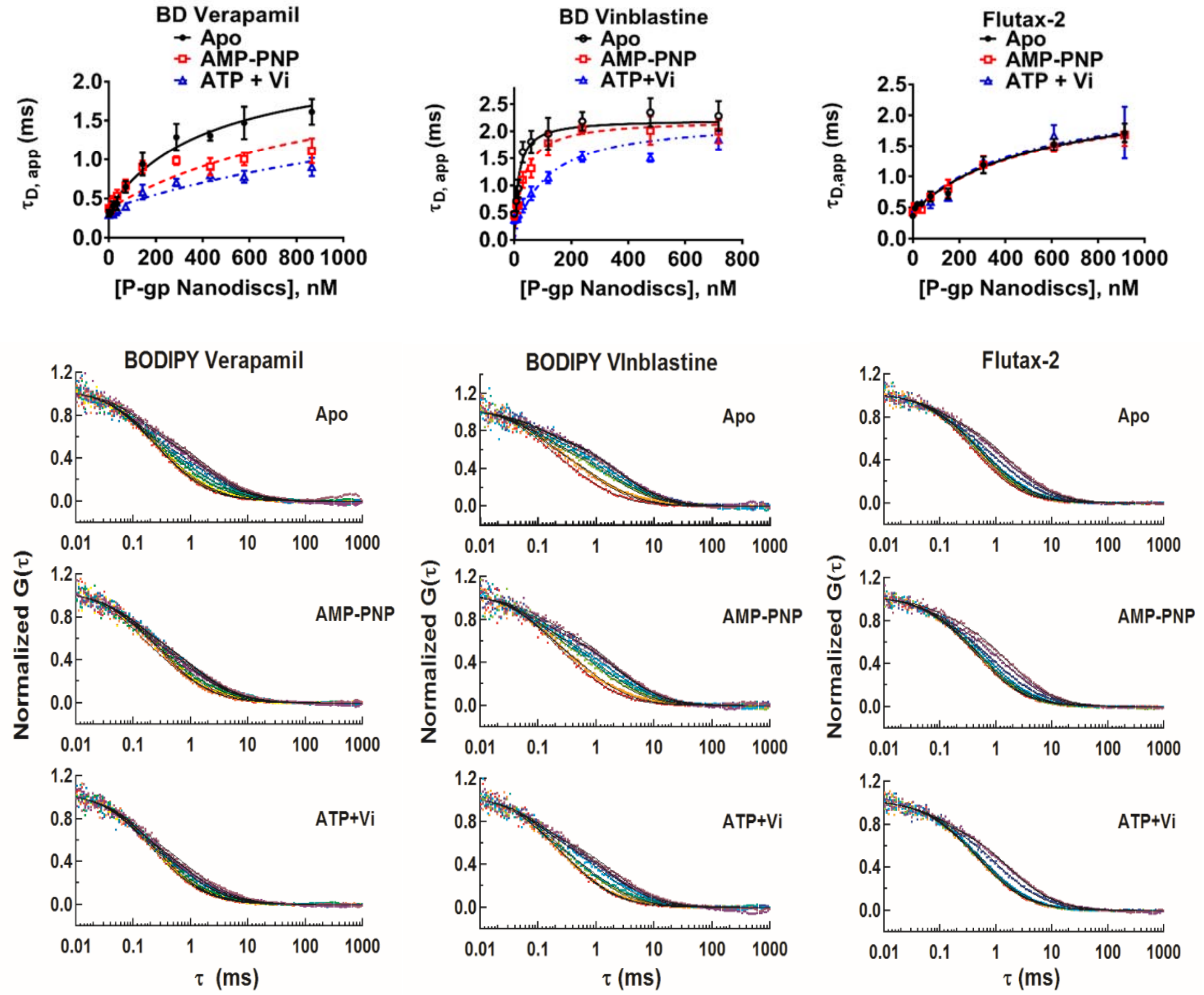

Figure 2.6. Equilibrium binding of fluorescent probes to P-gp nanodiscs under different nucleotide-bound conditions. *Top panel:* Saturation binding isotherms plotted as apparent diffusion time of probes as a function of P-gp concentration. *Bottom panels*: Normalized FCS autocorrelation curves of fluorescent probes with increasing nanodiscs concentrations (shifts from red to purple/left to right).

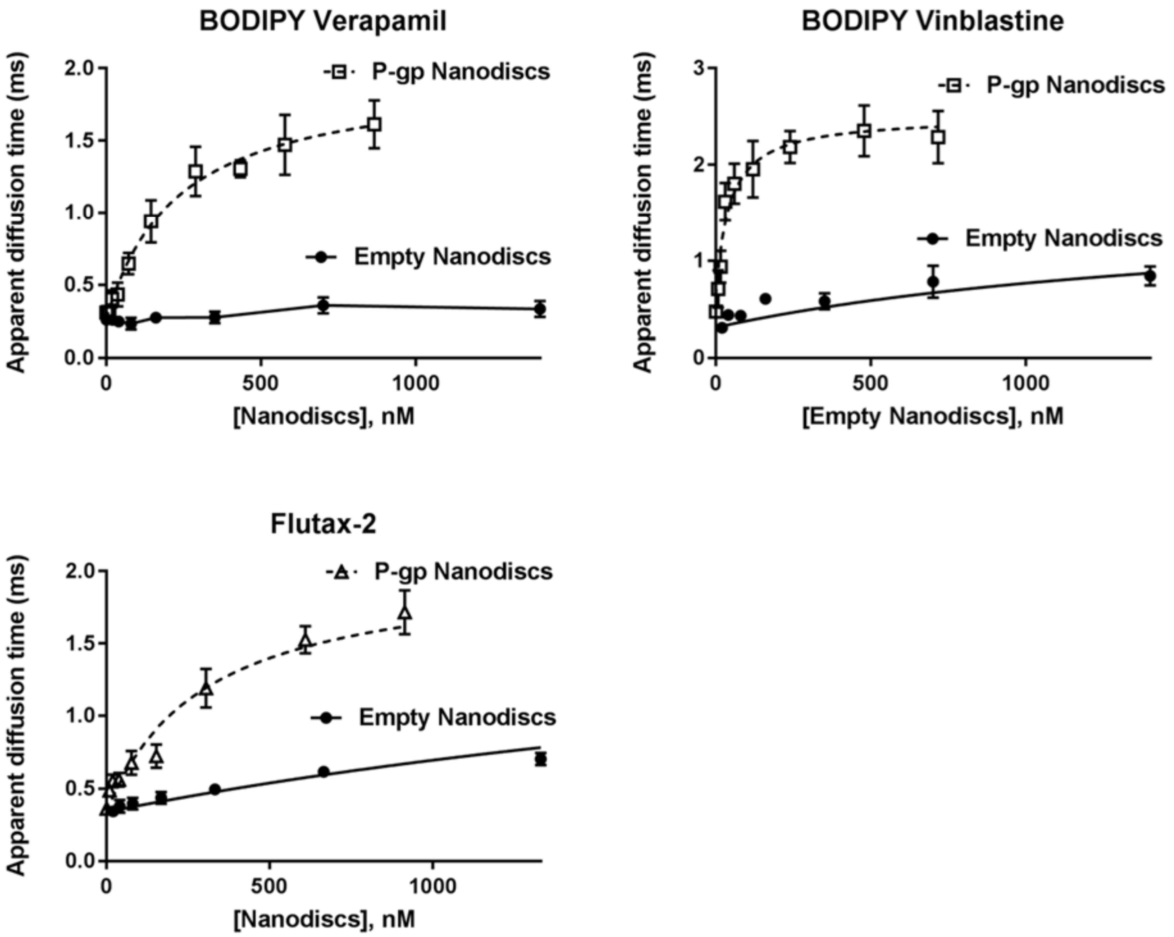

Figure 2.7. Binding of dyes to empty nanodiscs compared to P-gp nanodiscs.

Table 2.2. Nucleotide-dependent changes in affinity to fluorescent probe-ligands [a]

Nucleotide bound states	BD-Verapamil K_D (μM)	BD-Vinblastine K_D (μM)	Flutax-2 K_D (μM)
Apo (control)	0.23 ± 0.08	0.042 ± 0.006	0.52 ± 0.09
AMP-PNP	1.16 ± 0.3	0.083 ± 0.012	0.53 ± 0.09
ATP + V_i	2.35 ± 0.7	0.29 ± 0.04	0.49 ± 0.08
Empty nanodiscs	ND	1.67 ± 0.46	3.63 ± 0.32

ND = Not determined due to minimal binding at concentrations of nanodiscs used.

[a] Average values calculated based on global fits of at least two independent experiments

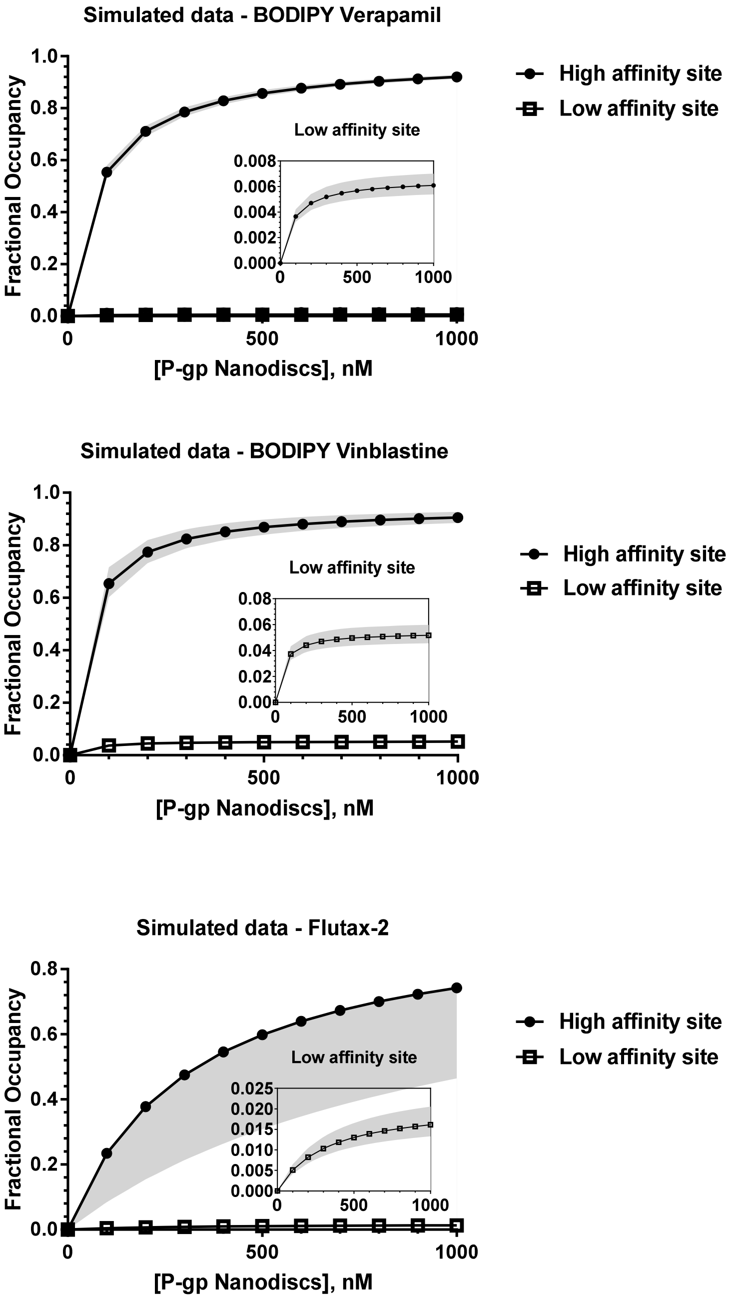

Figure 2.8. Simulated binding isotherms for BD-verapamil (top), BD-vinblastine (middle), and Flutax-2 (bottom) binding to the high affinity site (main panel) and the low affinity site (inset) based on the K_1 and K_2 values from ATPase assays. Flutax-2 did not stimulate ATPase activity and resulted in a larger prediction uncertainty of the high affinity site. For each probe, less than

0.5% of the second binding site is populated at the highest level of occupancy used in the FCS experiments.

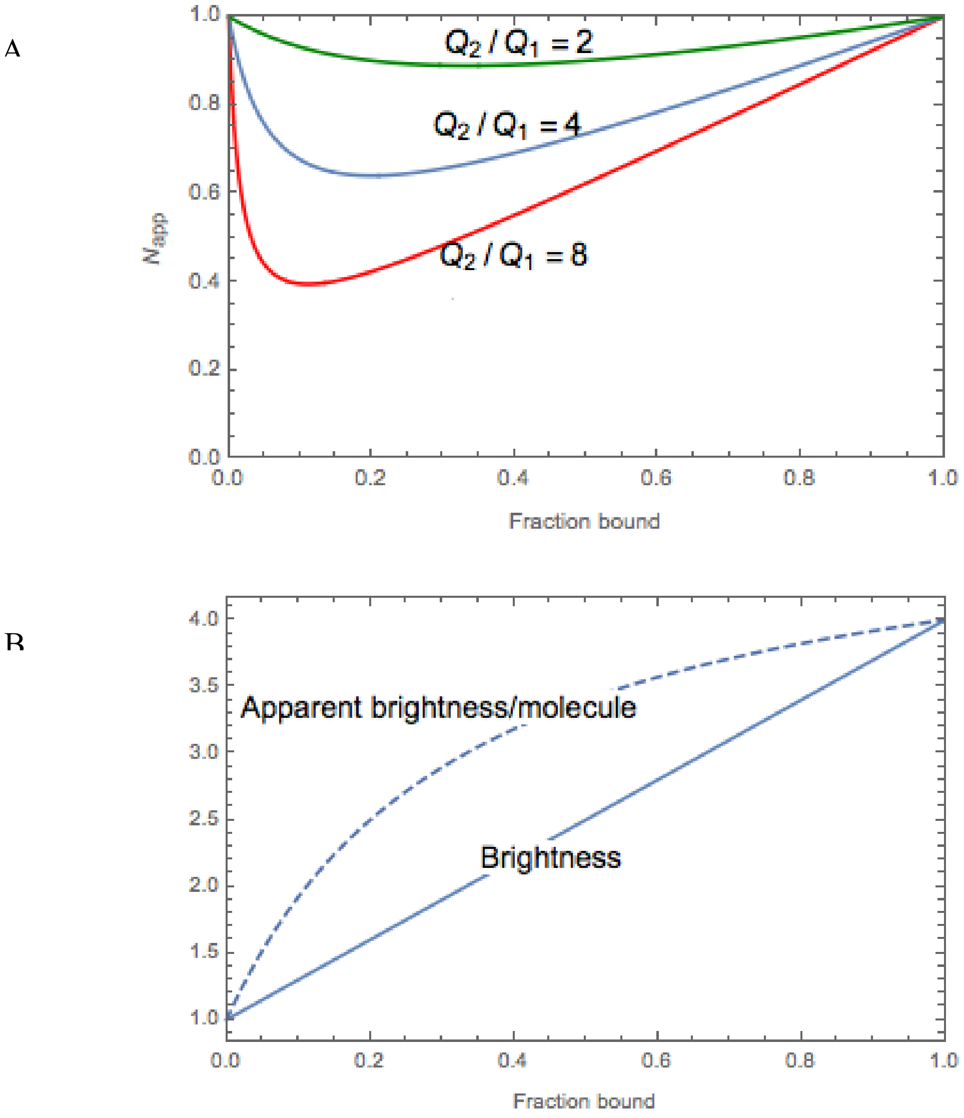

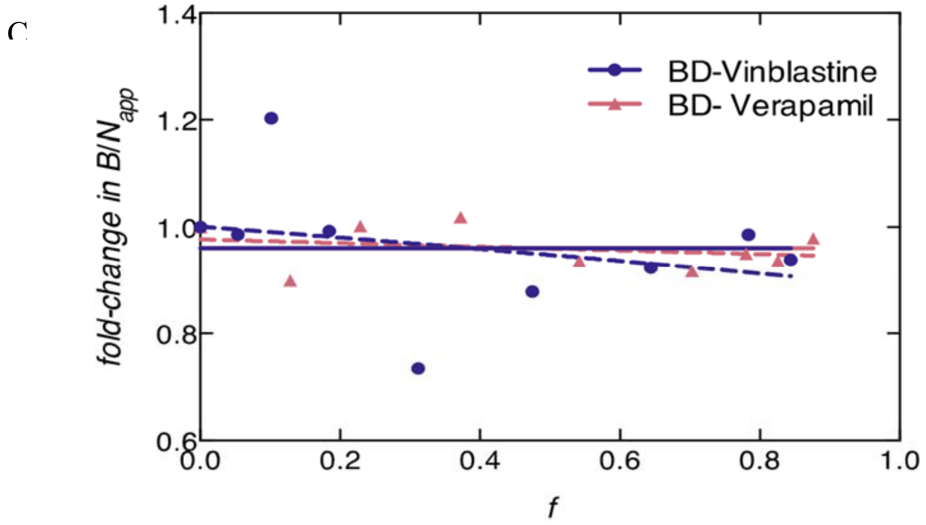

Figure 2.9. Analyses on increased brightness of BODIPY-drugs binding to P-gp nanodiscs. A) Apparent number of molecules (N_{app}) as a function of the molar fraction of the brighter species 2 (bound), under different ratios of quantum yields of species 1 and 2. Note that N_{app} remains constant and is reflective of the true N, at $f = 0$ and 1, when only species 1 or 2 exist. At intermediate concentrations where there is a mixture of species 1 and 2, N_{app} appears to decrease. B) Relationship between change in apparent molecular brightness or overall brightness, as a function of fraction bound, when $N = 1$ and $Q_2/Q_1 = 4$. As the fraction of the bound species 2 increases over the course of a titration, it is predicted that the overall brightness increase linearly with fraction bound, however the apparent brightness per molecule increases asymptotically. C) Fitting the experimentally observed changes in B/Napp for BD-verapamil and BD-vinblastine indicate that there is no evidence for a significant change in molecular brightness (F-test: $P > 0.4$ for both compounds).

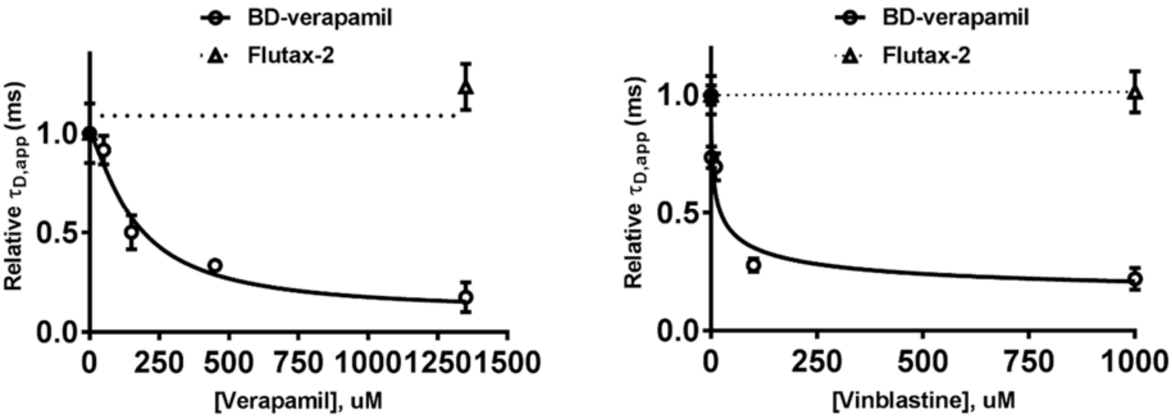

Figure 2.10. A comparison of dose-dependent effect of drugs on fluorescent probes binding to P-gp nanodiscs. Apparent diffusion time of BD-verapamil (open circles) and Flutax-2 (open triangles) measured as a function of concentration of unlabeled drug verapamil (left panel), or vinblastine (right panel). For this experiment 25 nM BD-verapamil or Flutax-2 was used in presence of 300 nM P-gp nanodiscs. Error bars represent standard deviation of 5 measurements. Verapamil and vinblastine displace BD-verapamil but not Flutax-2. Results from this experiment and competition experiments are summarized in Table 3.

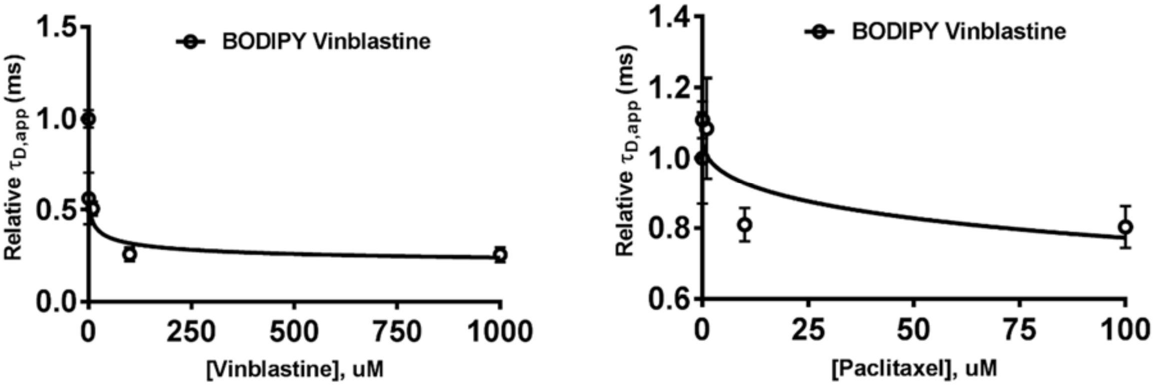

Figure 2.11. Competition experiments with BD-vinblastine and either vinblastine (left) or paclitaxel (right). BD-vinblastine is displaced by both vinblastine and paclitaxel.

Table 2.3. Effect and potency of modulators on fluorescent analogs binding to P-gp [a]

	Verapamil		Vinblastine		Paclitaxel	
	IC_{50} (μM)	*n*	IC_{50} (μM)	*n*	IC_{50} (μM)	*n*
BD-Verapamil	173 ± 69	0.95 ± 0.3	17.5 ± 11	0.5 ± 0.1	ND	
BD-Vinblastine	ND		8.8 ± 6	0.4 ± 0.1	327 ± 567	0.5 ± 0.5
Flutax-2	ND		ND		ND	

ND = No detectable changes in apparent diffusion time. *n* refers to the Hill coefficient

[a] Average values calculated from two independent experiments

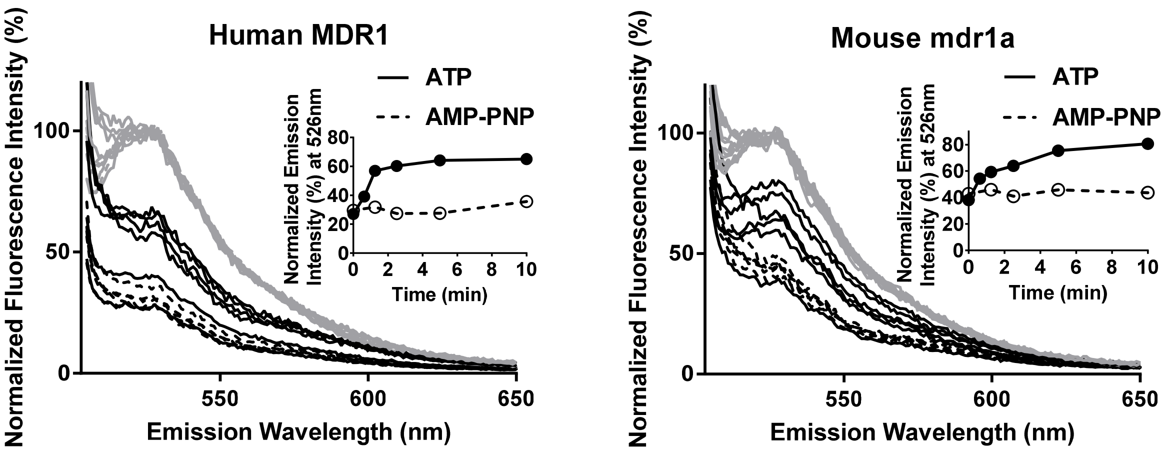

Figure 2.12. Transport of Flutax-2 into human or mouse P-gp vesicles. P-gp vesicles (50 μg protein) were incubated in the presence of 117 nM Flutax-2 and 4.7 mM ATP or AMP-PNP for various times before quenching the remaining free dye by anti-fluorescein IgG. A) and B) Overlaid emission spectra of Flutax-2 incubated with human or mouse P-gp vesicles respectively, excited at 495nm, with fluorescence intensity normalized to the intensity measured after addition of nucleotides (grey, taken as 100%). Normalized emission spectra measured immediately after addition of anti-fluorescein IgG to incubations with ATP or AMP-PNP were depicted in solid

black and dotted lines respectively. Inset: Normalized emission intensity measured at 526 nm, after quenching by antibody, plotted as a function of time.

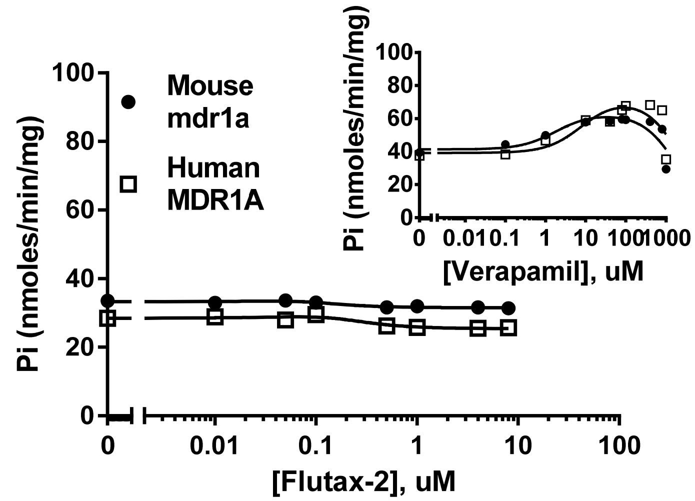

Figure 2.13. Modulation of ATPase activity of human and murine P-gp vesicles (Genomembrane) by Flutax-2. 5 µg total protein in vesicles were incubated in buffer containing 150 mM NH_4Cl, 50 mM Tris, 5 mM $MgSO_4$, 0.02% NaN_3, 5 mM TCEP, 100 µM EGTA, in presence of 1 mM ATP and varying Flutax-2 concentrations (1% final DMSO concentration) for one hour at 37 ºC. Parallel reactions containing 240 µM orthovanadate were carried out to subtract vanadate-insensitive ATPase activity. Inset: Positive control showing verapamil stimulated ATPase activity of human and mouse P-gp vesicles.

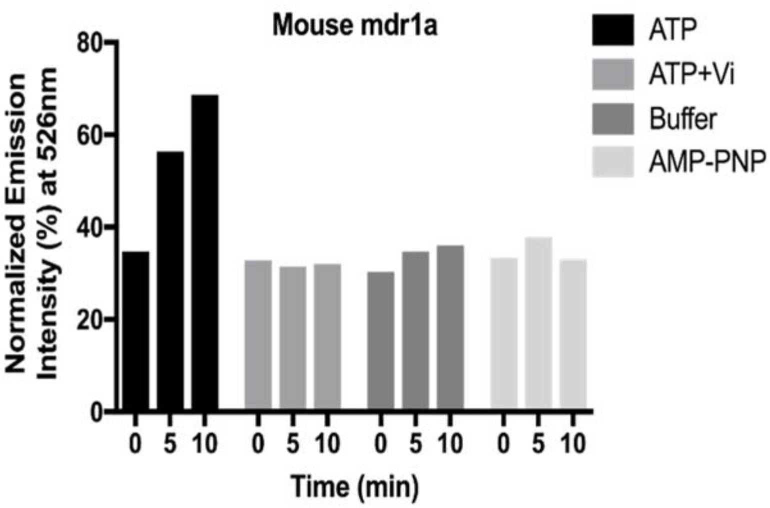

Figure 2.14. ATP-dependent transport of Flutax-2 by mouse P-gp inside-out vesicles. Negative controls using 4.7 mM ATP and 1.1 mM orthovanadate, 4.7 mM AMP-PNP or equal volume of buffer were performed according to the transport assay described in Methods for 0, 5 and 10 minutes of incubation time.

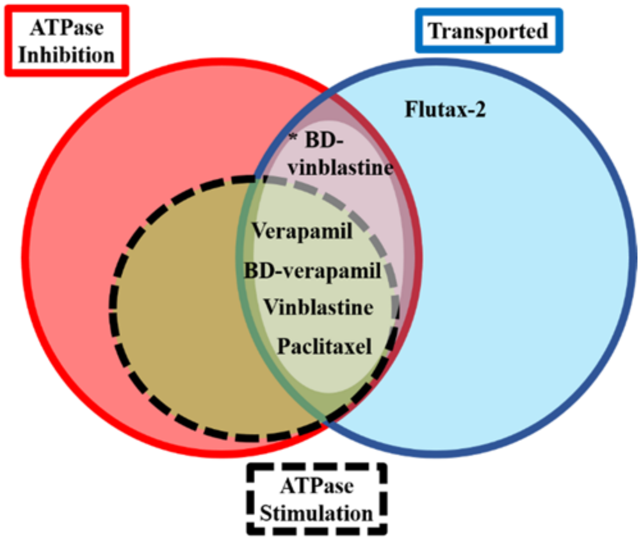

Figure 2.15. Venn diagram summarizing the interactions of drugs and fluorescent analogs used in this paper with P-glycoprotein. Dotted circle represents compounds that stimulate ATPase activity and also inhibit activity at high concentrations. Transport of compounds has been demonstrated

for both human MDR1 and mouse mdr1a (41-43). * Transport of BD- vinblastine demonstrated for human MDR1 (39).

2.5 References

1. Endicott, J. A., and Ling, V. (1989) The biochemistry of P-glycoprotein-mediated multidrug resistance. *Annual review of biochemistry* **58**, 137-171
2. Ferry, D. R., and Kerr, D. J. (1994) P-glycoprotein, a transporter with allosterically coupled drug-acceptor sites as a target for rational drug design. *New Molecular Targets For Cancer Chemotherapy*, 177-193
3. Ambudkar, S. V., Dey, S., Hrycyna, C. A., Ramachandra, M., Pastan, I., and Gottesman, M. M. (1999) Biochemical, cellular, and pharmacological aspects of the multidrug transporter 1. *Annual review of pharmacology and toxicology* **39**, 361-398
4. Aller, S. G., Yu, J., Ward, A., Weng, Y., Chittaboina, S., Zhuo, R., Harrell, P. M., Trinh, Y. T., Zhang, Q., and Urbatsch, I. L. (2009) Structure of P-glycoprotein reveals a molecular basis for poly-specific drug binding. *Science* **323**, 1718-1722
5. Li, J., Jaimes, K. F., and Aller, S. G. (2014) Refined structures of mouse P-glycoprotein. *Protein Science* **23**, 34-46
6. Dawson, R. J., and Locher, K. P. (2007) Structure of the multidrug ABC transporter Sav1866 from Staphylococcus aureus in complex with AMP-PNP. *FEBS Lett* **581**, 935-938
7. Higgins, C. F., and Linton, K. J. (2004) The ATP switch model for ABC transporters. *Nat Struct Mol Biol* **11**, 918-926
8. Hollenstein, K., Dawson, R. J., and Locher, K. P. (2007) Structure and mechanism of ABC transporter proteins. *Current opinion in structural biology* **17**, 412-418
9. Urbatsch, I. L., Tyndall, G. A., Tombline, G., and Senior, A. E. (2003) P-glycoprotein catalytic mechanism: studies of the ADP-vanadate inhibited state. *J Biol Chem* **278**, 23171-23179
10. Lomize, M. A., Lomize, A. L., Pogozheva, I. D., and Mosberg, H. I. (2006) OPM: orientations of proteins in membranes database. *Bioinformatics* **22**, 623-625
11. Ledwitch, K. V., Gibbs, M. E., Barnes, R. W., and Roberts, A. G. (2016) Cooperativity between verapamil and ATP bound to the efflux transporter P-glycoprotein. *Biochem Pharmacol* **118**, 96-108
12. Martin, C., Higgins, C. F., and Callaghan, R. (2001) The vinblastine binding site adopts high- and low-affinity conformations during a transport cycle of P-glycoprotein. *Biochemistry* **40**, 15733-15742
13. Qu, Q., Chu, J. W., and Sharom, F. J. (2003) Transition state P-glycoprotein binds drugs and modulators with unchanged affinity, suggesting a concerted transport mechanism. *Biochemistry* **42**, 1345-1353
14. Sauna, Z. E., and Ambudkar, S. V. (2000) Evidence for a requirement for ATP hydrolysis at two distinct steps during a single turnover of the catalytic cycle of human P-glycoprotein. *Proceedings of the National Academy of Sciences of the United States of America* **97**, 2515-2520

15. Ritchie, T. K., Kwon, H., and Atkins, W. M. (2011) Conformational analysis of human ATP-binding cassette transporter ABCB1 in lipid nanodiscs and inhibition by the antibodies MRK16 and UIC2. *J Biol Chem* **286**, 39489-39496
16. Ritchie, T. K., Grinkova, Y. V., Bayburt, T. H., Denisov, I. G., Zolnerciks, J. K., Atkins, W. M., and Sligar, S. G. (2009) Chapter 11 - Reconstitution of membrane proteins in phospholipid bilayer nanodiscs. *Methods Enzymol* **464**, 211-231
17. Lerner-Marmarosh, N., Gimi, K., Urbatsch, I. L., Gros, P., and Senior, A. E. (1999) Large scale purification of detergent-soluble P-glycoprotein from Pichia pastoris cells and characterization of nucleotide binding properties of wild-type, Walker A, and Walker B mutant proteins. *J Biol Chem* **274**, 34711-34718
18. Chifflet, S., Torriglia, A., Chiesa, R., and Tolosa, S. (1988) A method for the determination of inorganic phosphate in the presence of labile organic phosphate and high concentrations of protein: application to lens ATPases. *Anal Biochem* **168**, 1-4
19. Litman, T., Zeuthen, T., Skovsgaard, T., and Stein, W. D. (1997) Structure-activity relationships of P-glycoprotein interacting drugs: kinetic characterization of their effects on ATPase activity. *Biochim Biophys Acta* **1361**, 159-168
20. Diaz, J. F., Strobe, R., Engelborghs, Y., Souto, A. A., and Andreu, J. M. (2000) Molecular recognition of taxol by microtubules. Kinetics and thermodynamics of binding of fluorescent taxol derivatives to an exposed site. *J Biol Chem* **275**, 26265-26276
21. Petrasek, Z., and Schwille, P. (2008) Precise measurement of diffusion coefficients using scanning fluorescence correlation spectroscopy. *Biophys J* **94**, 1437-1448
22. Yang, J., Yan, R., Roy, A., Xu, D., Poisson, J., and Zhang, Y. (2015) The I-TASSER Suite: protein structure and function prediction. *Nat Methods* **12**, 7-8
23. Szewczyk, P., Tao, H., McGrath, A. P., Villaluz, M., Rees, S. D., Lee, S. C., Doshi, R., Urbatsch, I. L., Zhang, Q., and Chang, G. (2015) Snapshots of ligand entry, malleable binding and induced helical movement in P-glycoprotein. *Acta Crystallogr D Biol Crystallogr* **71**, 732-741
24. Senior, A. E. (2011) Reaction chemistry ABC-style. *Proc Natl Acad Sci U S A* **108**, 15015-15016
25. Urbatsch, I. L., Sankaran, B., Weber, J., and Senior, A. E. (1995) P-glycoprotein is stably inhibited by vanadate-induced trapping of nucleotide at a single catalytic site. *J Biol Chem* **270**, 19383-19390
26. Frank, G. A., Shukla, S., Rao, P., Borgnia, M. J., Bartesaghi, A., Merk, A., Mobin, A., Esser, L., Earl, L. A., Gottesman, M. M., Xia, D., Ambudkar, S. V., and Subramaniam, S. (2016) Cryo-EM Analysis of the Conformational Landscape of Human P-glycoprotein (ABCB1) During its Catalytic Cycle. *Mol Pharmacol* **90**, 35-41
27. Moeller, A., Lee, S. C., Tao, H., Speir, J. A., Chang, G., Urbatsch, I. L., Potter, C. S., Carragher, B., and Zhang, Q. (2015) Distinct conformational spectrum of homologous multidrug ABC transporters. *Structure* **23**, 450-460
28. Patwardhan, G., Gupta, V., Huang, J., Gu, X., and Liu, Y.-Y. (2010) Direct assessment of P-glycoprotein efflux to determine tumor response to chemotherapy. *Biochemical pharmacology* **80**, 72-79
29. Martin, C., Berridge, G., Higgins, C. F., Mistry, P., Charlton, P., and Callaghan, R. (2000) Communication between Multiple Drug Binding Sites on P-glycoprotein. *Molecular Pharmacology* **58**, 624-632

30. Pascaud, C., Garrigos, M., and Orlowski, S. (1998) Multidrug resistance transporter P-glycoprotein has distinct but interacting binding sites for cytotoxic drugs and reversing agents. *Biochemical Journal* **333**, 351-358
31. Polli, J. W., Wring, S. A., Humphreys, J. E., Huang, L., Morgan, J. B., Webster, L. O., and Serabjit-Singh, C. S. (2001) Rational Use of in Vitro P-glycoprotein Assays in Drug Discovery. *Journal of Pharmacology and Experimental Therapeutics* **299**, 620-628
32. Sharom, F. J. (2014) Complex Interplay between the P-Glycoprotein Multidrug Efflux Pump and the Membrane: Its Role in Modulating Protein Function. *Frontiers in Oncology* **4**, 41
33. Liu, R., and Sharom, F. J. (1996) Site-directed fluorescence labeling of P-glycoprotein on cysteine residues in the nucleotide binding domains. *Biochemistry* **35**, 11865-11873
34. Taylor, J. C., Ferry, D. R., Higgins, C. F., and Callaghan, R. (1999) The equilibrium and kinetic drug binding properties of the mouse P-gp1a and P-gp1b P-glycoproteins are similar. *Br J Cancer* **81**, 783-789
35. Nath, A., Atkins, W. M., and Sligar, S. G. (2007) Applications of phospholipid bilayer nanodiscs in the study of membranes and membrane proteins. *Biochemistry* **46**, 2059-2069
36. Nath, A., Trexler, A. J., Koo, P., Miranker, A. D., Atkins, W. M., and Rhoades, E. (2010) Single-molecule fluorescence spectroscopy using phospholipid bilayer nanodiscs. *Methods Enzymol* **472**, 89-117
37. Trahey, M., Li, M. J., Kwon, H., Woodahl, E. L., McClary, W. D., and Atkins, W. M. (2015) Applications of Lipid Nanodiscs for the Study of Membrane Proteins by Surface Plasmon Resonance. *Curr Protoc Protein Sci* **81**, 29 13 21-16
38. Ambudkar, S. V., Kimchi-Sarfaty, C., Sauna, Z. E., and Gottesman, M. M. (0000) P-glycoprotein: from genomics to mechanism. *Oncogene* **22**, 7468-7485
39. Bársony, O., Szalóki, G., Türk, D., Tarapcsák, S., Gutay-Tóth, Z., Bacsó, Z., Holb, I. J., Székvölgyi, L., Szabó, G., Csanády, L., Szakács, G., and Goda, K. (2016) A single active catalytic site is sufficient to promote transport in P-glycoprotein. *Scientific Reports* **6**, 24810
40. Sarkadi, B., Price, E. M., Boucher, R. C., Germann, U. A., and Scarborough, G. A. (1992) Expression of the human multidrug resistance cDNA in insect cells generates a high activity drug-stimulated membrane ATPase. *J Biol Chem* **267**, 4854-4858
41. Candussio, L., Crivellato, E., Rosati, A. M., Klugmann, F. B., Granzotto, M., Giraldi, T., and Decorti, G. (2001) Expression and function of P-glycoprotein and absence of multidrug resistance-related protein in rat and beige mouse peritoneal mast cells. *Histochem J* **33**, 259-266
42. Sadiq, M. W., Uchida, Y., Hoshi, Y., Tachikawa, M., Terasaki, T., and Hammarlund-Udenaes, M. (2015) Validation of a P-Glycoprotein (P-gp) Humanized Mouse Model by Integrating Selective Absolute Quantification of Human MDR1, Mouse Mdr1a and Mdr1b Protein Expressions with In Vivo Functional Analysis for Blood-Brain Barrier Transport. *PLoS One* **10**, e0118638
43. Schinkel, A. H., Wagenaar, E., Mol, C. A., and van Deemter, L. (1996) P-glycoprotein in the blood-brain barrier of mice influences the brain penetration and pharmacological activity of many drugs. *J Clin Invest* **97**, 2517-2524

Chapter 3

Slow, Asymmetric Conformational Dynamics of P-glycoprotein in Lipid Nanodiscs

Parts of this chapter have been taken from a manuscript in preparation.

3.1 Introduction

It is well-established in the literature, and from results in the previous chapter, that drug transport is an energy-coupled process which involves large scale conformational rearrangements. The available crystal structures from multiple homologous ABC transporters, including Sav1866 and MsbA (1-3), combined with cryoEM structures, DEER studies with spin-labeled variants, and FRET with fluorescently-labeled NBDs, suggest that P-gp undergoes large scale opening and closing motions, between an inward facing (IF) conformational ensemble and outward-facing (OF) conformational ensemble (4-6). For some ABC transporters, nucleotides drive formation of a stable OF conformation with the NBDs in intimate contact. In addition, the transition state for ATP hydrolysis can be mimicked by addition of ATP, or ADP, and vanadate, which 'traps' a quasi-stable OF conformation (7,8). In contrast to Sav1886 or MsbA, however, recent data suggest that the IF to OF conformational transition of P-gp is less tightly coupled to nucleotide binding or hydrolysis (9); even in the presence of excess nucleotide and vanadate, P-gp retains a substantial population of IF states with varying degrees of separation between NBDs (10,11). Apparently, the 'nucleotide-trapped' OF conformations of P-gp are less stable than in other ABC proteins, although vanadate trapping leads to near complete inhibition of ATPase activity even for P-gp. The emerging model suggests that drug-free P-gp samples a wide range of IF conformations that could bind different substrates or inhibitors, even with nucleotide bound. Apparently, the drug free P-gp explores an expansive conformational landscape with a dynamic equilibrium of states defined by different inter-NBD distances.

However, little is known about the local conformational status of discrete regions within either the IF or OF ensembles. Molecular dynamics simulations and X-ray structures suggest that, in addition to the large amplitude motions associated with switching between IF and OF states, some regions undergo local fluctuations in secondary structure, including 'hinge regions' in the TMHs (6,12,13). It is possible that low amplitude, local, transitions in these hinge regions could be propagated to the NBDs to account for the wide range of inter-NBD distances. However, no experimental methods have revealed specific conformational changes within the IF ensemble that could participate in the recruitment of substrates or coupling of binding and ATP hydrolysis. In fact, little information is available concerning the time scales for conformational relaxation within the ensemble. In addition, the structural models are obtained in the absence of a membrane, so the effects of a lipid bilayer on the conformational status remain uncharacterized.

In order to map the local dynamics of P-gp with increased spatial and temporal resolution, we have performed H/D exchange mass spectrometry (H/DX MS) with P-gp in lipid nanodiscs compared with P-gp in detergent solution. The results indicate complex local dynamics superimposed on the IF conformational ensemble. Interestingly, the dynamics include relaxations on a remarkably wide range of time scales.

3.2 Materials and Methods

3.2.1 P-gp and MSP1D1 Protein Expression and Purification

Hexa-histidine tagged MSP1D1 was expressed in *Escherichia coli* and purified as described in Chapter 2. Expression of his-tagged P-gp in Pichia pastoris and purification were carried out as in Chapter 2.

3.2.2 P-gp in Detergent-Lipid Micelles or Nanodiscs

1mg/ml purified P-gp was solubilized in buffer containing 20 mM Tris, 100 mM NaCl, 1 mM TCEP, 0.1% DDM, pH 7.4. DMPC lipid was added to a final lipid-protein ratio of 2:1 (w/w) for activation of P-gp, and for optimal micelle formation with a lipid-detergent ratio (or R_{sol}) of around 2 (w/w) (14,15). Reconstitution of P-gp into DMPC nanodiscs was carried out as described (16). P-gp nanodiscs were separated from empty nanodiscs by SEC-HPLC chromatography (Superdex 200 10/300 GL column, GE Healthcare) and concentrated up to 1 µM using a 100 kDa MWCO spin filter (Millipore).

3.2.3 Hydrogen Deuterium Exchange

P-gp micelles or nanodiscs were incubated in the absence or presence of 10 mM MgATP and 2.4 mM vanadate for 15 minutes at 25 ºC, prior to hydrogen deuterium exchange experiments. Exchange reactions for P-gp nanodiscs were initiated by a 10-fold dilution into deuterated buffer containing 95% D_2O (Cambridge Isotope Labs), 20 mM Tris, 100 mM NaCl, 2 mM MgCl, pD 7.4 and samples were incubated at 25 ºC for various times. Deuterated buffer including 0.1% DDM was used for exchange reactions with P-gp micelles. Samples were quenched with an equal volume of ice-cold quench buffer (300 mM KPi, 4 M guanidine hydrochloride, 250 mM TCEP [tris(2-carboxyethyl)phosphine], pH 2.5), followed by an addition of 25:1 sodium cholate/DMPC, and the entire mixture was transferred rapidly to ice-cold immobilized pepsin (Pierce) for a 5 minute digestion. At the last minute of digestion, 3 mg of ZrO_2 coated silica resin (Hybrid SPE resin, Sigma) (or 10 mg for P-gp micelles) was added to the mixture and incubated on ice for the remaining duration to remove excess lipid. The final mixture was filtered using a cold microcentrifuge spin filter (0.45 μm cellulose acetate) at 4 ºC for 30 seconds, before rapidly frozen in liquid nitrogen and stored at -80 ºC until analysis. All reactions contained the tetrapeptide, PPPI, as an internal standard to ensure consistency in exchange conditions across samples. Undeuterated samples were prepared with the steps described above, except that Optima LC-MS grade H_2O was used in place of D_2O.

3.2.4 Mass Spectrometry

Samples were thawed on ice for 5 minutes and injected onto a refrigerated Waters nanoAcquity HDX-UPLC system coupled to a Synapt G2-S QTOF mass spectrometer (Waters). Peptides were trapped and desalted on a trap C8 column flowing 0.1% formic acid (FA) with 0.02% trifluoroacetic acid (TFA) at 100 μL/min for 3 min (ACUITY UPLC BEH C8 1.7 μm VanGuard column, Waters), followed by separation using an analytical C8 column (ACUITY UPLC BEH C8 1.7 μm, 1 x 100 mm column, Waters) running a gradient of 5- 40% solvent B for 8 min (solvent A, 0.1% FA, 0.02% TFA and 5% acetonitrile (ACN); solvent B, 0.1% FA, 0.02% TFA and 80% ACN). At the end of UPLC gradient, sample flow from the column was diverted to waste to prevent excess cholate from entering the mass spectrometer. To minimize sample carryover, the column was cleaned with two rapid cycles of 10-100% solvent B while the syringe, loop and trap column were washed with a series of 10% FA, 80% methanol, 2:1 isopropanol/ACN and 80% ACN. The electrospray ionization source was operated in the positive ion mode and ion mobility was enabled for the instrument. Peptide identification were done by tandem MS/MS using a combination of data independent acquisition method with ion mobility (High Definition MS^E) and data-dependent MS/MS acquisition. Peptic fragments of P-gp were identified through database searching in ProteinLynx Global Server Version 3 (Waters) as well as through Protein Prospector. Relative deuterium uptake based on the centroid of isotopic distribution was processed by DynamX Version 3 (Waters) and deuterium incorporation was not corrected for back-exchange. Bimodal mass spectra were deconvoluted using HX-Express 2 to extract fractional contribution by individual mass envelopes. The rate of relaxation was determined by fitting the fractional decay of the lower mass species with a first-order exponential.

3.2.5 Activity Assay

The hydrolysis of ATP by P-gp (ATPase activity) was determined from the amount of inorganic phosphate released from ATP hydrolysis, based on a colorimetric method adapted from Chifflet (17). P-gp in nanodiscs (1 µg) or detergent-lipid micelles (3 µg) were aliquoted into tubes and incubated at 25 °C for varying duration (0 to 4 hours). At the end of incubation, assay buffer (50 mM Tris, 150 mM NH_4Cl, 5 mM $MgCl_2$, 0.02% NaN_3, 10 mM TCEP, 100 µM verapamil, 1 mM ATP, pH 7.4) in the absence or presence of 240 µM Vi was added to initiate the reaction. After 30 minutes at 37 °C, the reaction was stopped by adding EDTA to a final concentration of 10 mM. The absorbance intensity from the formation of phosphomolybdate was measured at 850 nm using a Tecan Infinite M200 microplate reader.

3.3 Results

3.3.1 Comparison of P-gp in Nanodiscs Compared to Detergent Solubilized P-gp

In order to determine whether the lipid or detergent environment has an impact on local dynamics, we performed H/DX MS on P-gp reconstituted in DMPC nanodiscs and detergent-lipid micelles. At various times after dilution into buffer containing D_2O, the exchange reactions were quenched, the protein was digested, and peptides were analyzed for deuterium uptake. The recovered peptides spanned 37.7 % and 40.1 % of the total protein primary sequence for P-gp in nanodiscs vs. P-gp in detergent, respectively. As expected this included mainly peptides in the NBDs. Considering only NBDs, the sequence coverage in H/DX experiments was 68.2 % and 70.3 % for the P-gp in nanodiscs vs. in detergent, respectively (Table 3.1 and Figure 3.1). Thus, the H/DX provides a good characterization of the backbone dynamics for the NBDs. The fractional incorporation of deuterium into all recovered peptides at varying times is shown in Figure 3.2A for the nucleotide-free P-gp as well as for ATP/Vanadate trapped P-gp ("Vi Trapped" in Figure 3.2A). The individual points represent the midpoint of each recovered peptide and they report the percent of amide protons that have been exchanged for that peptide. Note that the density of points within the sequences corresponding to the TMHs is much lower than the density of points in the regions corresponding to NBDs. This reflects the lower recovery of peptides in the TMHs. The 'butterfly plots' in Figure 3.2A indicate only modest changes in H/D exchange upon vanadate trapping (lower half of each butterfly plot) compared to the apo P-gp (upper half of each butterfly plot). The differences are most easily identified in the difference plots in Figure 3.2B, where positive values indicate peptides with lower deuterium exchange in the vanadate trapped samples compared to apo samples and negative values indicate greater exchange in the vanadate trapped protein. These plots demonstrate that the deuterium exchange properties are very similar in detergent and in nanodiscs with a few notable differences. Specifically, sequences throughout both NBDs become modestly less susceptible to exchange upon vanadate trapping, and the differences is slightly larger for the P-gp in detergent than in nanodiscs. That is, P-gp in detergent adopts more distinct IF and OF conformations for the nucleotide-free vs. vanadate trapped, states based on the difference in exchange. Also, the data for both environments are consistent with vanadate trapping causing a redistribution of the IF conformations toward a more closed OF ensemble without forming a 'tight' or rigid OF state.

A few specific peptides are of particular interest. It is notable that the intracellular loops ICL 1, ICL3, and ICL4 that are thought to mediate coupling between drug binding sites in the TMHs and the NBDs (ICL2 was not recovered) are also protected from exchange upon vanadate trapping, indicating that their local conformation is altered, as expected for a greater population of the OF upon Vi trapping. These ICLs exhibit a significantly greater sensitivity to vanadate trapping in detergent than in nanodiscs. Consistently in both detergent and lipid environments, ICL4 is more exchange-protected in the presence of vanadate than ICL1. Asymmetry in the ATP binding sites is also observed. The Walker A (WA) peptide and the Q loop in NBD1 undergo a larger decrease in solvent accessibility with vanadate trapping, compared to NBD2. D and H loops in NBD2 appear to be modestly more solvent-exposed in the presence of Vi-trapping than in NBD1. In addition, although the coverage throughout the TMHs is low, the peptide 69-78 behaves according to our expectations. Specifically, peptide 69-78 exhibits an observable increase in HDX upon addition of ATP and vanadate, in marked contrast to the vast majority of peptides in the NBDs. This is expected for the OF conformation which allows for solvent access to the drug binding sites and this is discussed in further detail in Discussion.

In general, the relative changes with vanadate trapping of peptides throughout P-gp are qualitatively the same in nanodiscs as they are in detergent, although NBD1 is more sensitive to ATP/vanadate than NBD2. These results for the P-gp in detergent and in nanodiscs, in the presence and absence of ATP/Vanadate are superimposed on the three dimensional structure of murine P-gp in Figures 3.2C and D.

3.3.2 Direct Observation of Conformational Relaxation, Mixed EX1/EX2 Kinetics

Closer examination of the time course of deuterium exchange revealed a large number of peptides with time-dependent bimodal distributions of deuterated peptide ions or 'EX1 kinetics.' This behavior results when a slow change in solvent accessibility or slow folding-refolding equilibrium occurs more slowly than amide deuterium exchange. A total of 4 peptides exhibited mixed EX1/EX2 kinetics for P-gp in detergent and 15 peptides demonstrated this behavior in nanodiscs, suggesting that the lipid bilayer slows down local dynamics that are otherwise too fast to observe, in the detergent preparations. The deuterium uptake data for exemplary mixed EX1/EX2 behavior are shown in Figure 3.3. The widespread distribution of peptides with EX1 kinetic behavior throughout the NBDs suggests a wide range of conformational diversity on biologically relevant time scales (Figure 3.3B).

It is particularly striking that the EX1 kinetics occur on a such wide range of time scales for different peptides; some peptides undergo conformational relaxation over the course of a minute while others take several hours to relax. The most solvent-exposed peptide in both nanodiscs and detergent mixtures, 1036-1053, undergoes the fastest rate of relaxation with a half-life of 47s (Figure 3.3A). It is located in a large, unstructured loop connecting two beta sheets after TM12 but prior to WA (NBD2). Interestingly, distant peptides based on the linear sequence of P-gp display similar kinetics when they are located near each other or are expected to interact in the tertiary structure. For example in both detergent and nanodiscs preparations, peptides containing the C motif of NBD1 (520-549) and WA of NBD2 (1065-1078) exhibit slow EX1 kinetics and are involved in the formation of a sandwich dimer (Figure 3.4). In addition, peptides from ICL1 (153-167) and ICL4 (901-915), although far apart based on the primary sequence, extend as coupling helices in close contact to NBD1 and they exhibit EX1 kinetics on a similar time scale (Figure 3.3D).

Generally, all of the peptides that display bimodal kinetics are found in connecting loop regions between beta strands or alpha-helices in the NBDs or ICLs, which is consistent with a MD simulations where local fluctuations in these regions contribute to global, conformational dynamics of P-gp (11). Peptides with moderate conformational relaxation rates (half-life between minutes to 4h) are found to be distributed across the protein, including ICL1 and ICL4. Peptides with slow relaxation rates are found at both of the NBDs in the ATP binding sites. These peptides are mapped onto the structure of P-gp in Figures 3.3C and D.

Vanadate trapping slows down the rate of relaxation for some of these peptides. For most of the peptides, especially those with slow relaxation rates in the free enzyme, the increase in half-life for exchange in the presence of ATP and Vi could not be measured within the resolution of these experiments. However, for peptide 1036-1053, it is observed that vanadate trapping results in a ~10 fold increase in half-life of relaxation, from 47 s to 9.6 min (Figure 3.5). This is consistent with the general 'tightening' of the NBDs noted in Figure 3.2.

3.3.3 Functional Stability in Nanodiscs and Detergent-Lipid Micelles

In order to determine whether the unusually slow conformational exchange revealed by the bimodal EX1 kinetics P-gp denaturation was due to time-dependent denaturation of P-gp, we monitored the functional properties of P-gp in detergent and nanodiscs during the time course used to monitor H/DX. P-gp in nanodiscs and detergent-lipid micelles were pre-incubated at 25°C for varying duration before they were assayed for ATPase activity by a standard method (see Methods). Because of the low basal activity of P-gp in detergent, verapamil was added as part of the ATPase buffer to produce an appreciable increase in phosphate release. The results are shown in Figure 3.6. The stimulated ATPase activities of P-gp in detergent and nanodiscs are constant throughout the entire course of the 4 hour H/DX experiment. As an additional probe of the functional effects of the time-dependent changes in conformation observed by H/DX, we pre-incubated a sample of P-gp nanodiscs for 4 hrs at 25°C prior to H/D exchange. After 4 hrs we performed an exchange experiment and monitored deuterium uptake after 1 minute. The results were identical to the deuterium uptake observed at 1 minute without pre-incubation (Figure 3.7). This result demonstrates that the slow conformational exchange observed in the EX1 kinetic behavior is not the result of an irreversible, non-equilibrium, change. Rather the slow EX1 kinetics reflect an equilibrative exchange process.

3.4 Discussion

The results reveal several features of P-gp dynamics. The direct comparison of the global exchange kinetics demonstrates that P-gp dynamics in lipid nanodiscs are qualitatively similar to the dynamics in detergent solubilized preparations. In both cases, the NBDs yielded good peptide coverage and 68.2 %- 70.3 % of the NBDs was amenable to analysis in nanodiscs and micelles.

For both the P-gp in the lipid membrane and in detergent, treatment with ATP and vanadate resulted in modest reductions in the deuterium exchange rates for most peptides in the NBDs, consistent with a redistribution of the IF vs. OF macroconformations toward the OF state, which is expected to have more intimate contact between NBDs and slower exchange. Notably however, the vanadate trapping did not result in a major decrease in exchange for any peptides, suggesting that the vanadate trapped state of P-gp is not as long-lived or well populated as it is for other ABC transporters, despite its persistent lack of ATPase activity. In addition, several peptides from the TMHs of P-gp in detergent were recovered and their exchange behavior was consistent with expectations. Specifically, the peptide corresponding to residues 69-78 in TMH1 undergoes a moderate shift to greater solvent accessibility upon addition of ATP and vanadate, consistent with shift toward the OF state. Inspection of different OF conformations from homology modelling suggest that this observation may be due to the movement of TM1 itself, accentuated by the proline kink (Pro 66), or due to movement of neighboring helices away from TM1 (Figure 3.8). Other peptides in the TMHs (eg. TM7) behave as expected of highly ordered, alpha-helical structures and are highly solvent-protected with a low rate of deuterium uptake (Figure 3.9). Taken together the current results with H/DX MS and other studies based on cryoEM and DEER suggest that P-gp cannot be trapped in tightly closed OF state with persistent long-lived NBD-NBD interactions although the ensemble shifts toward an equilibrium mixture that resembles the OF conformation to a greater extent than in the absence of ATP and vanadate.

The results for these H/DX experiments address an apparent discrepancy between two EM studies with P-gp in different lipid environments (4,10). For the current results, a larger difference in deuterium uptake between the ligand-free and vanadate-trapped P-gp in detergent micelles suggests that P-gp adopts more distinct IF and OF conformations under these conditions, in agreement with the recent cryoEM results that demonstrated that P-gp exists in a mixture of IF and OF conformations that converts more completely to OF conformation in presence of ATP and Vi. Together, those cryoEM studies and the current H/DX results suggest that P-gp behaves more like a two-state system, IF and OF, in detergent micelles. In contrast, a more modest difference in deuterium uptake between ligand-free and vanadate-trapped protein is observed for P-gp nanodiscs, which suggests that there is a shift in equilibria to more OF-like conformations without static association of the NBDs due to the intrinsic flexibility of P-gp in a lipid membrane. Our results demonstrate that there are differences in the conformational dynamics of P-gp in a lipid vs. detergent environment.

The most striking aspect of the results is the large number of peptides that exhibit mixed EX1/EX2 kinetics. The fact that several peptides within the NBDs and at least two of the ICLs exhibit conformational exchange on a wide range of time scales is consistent with the suggestion based on other methods that P-gp is conformationally heterogeneous. The conformational exchange detected by H/DX makes structural sense, in as much as the peptides that display this behavior consist of regions where helices or β-strands defined by crystallographic models terminate. The unwinding of the ends of helices or the fraying of β -sheets at the ends of strands is expected to occur on slower time scales than deuterium uptake of solvent exposed amides, and the fluctuation between a random coil and a local folded structure is what gives rise to ‘EX1’ exchange kinetics.

An additional observation of significance is the asymmetric distribution of the H/D exchange behavior, between the two NBDs. As noted above and shown in Figure 3.2, WA and Q loop in NBD1 undergo a larger decrease in solvent accessibility with vanadate trapping compared to NBD2. Although these differences are modest, they demonstrate that the well-established functional asymmetry of the NBDs which leads to their alternate occupancy by nucleotides is recapitulated in the dynamics of the different NBDs; they are dynamically asymmetric as well as functionally asymmetric.

These experiments have implications for mechanisms of promiscuous substrate recognition by P-gp. The results do not directly address the effects of substrates on the conformational landscape of P-gp; additional studies with multiple substrates or inhibitors will be necessary to map such effects. However, to the extent that the extraordinary conformational diversity of the substrate-free IF ensemble in the NBDs can be extrapolated to the TMHs, it is reasonable to expect that substrates in the membrane would encounter many TMH conformations at any instant, and this in turn leads to the possibility that different substrates have different affinities for different conformations. For single substrate enzymes, the situation in which a substrate encounters a range of conformations and binds preferentially to one member of the ensemble represents the limiting case model for ligand-dependent conformational dynamics known as 'conformational selection.' Conformational selection is distinct from the other commonly used limiting case model of 'induced fit' in which a substrate encounters and binds to a single enzyme conformation, which subsequently undergoes conformational change to an active, higher affinity form (Figure 3.10). Importantly, conformational selection and induced fit are not mutually exclusive models. In fact, the detoxication enzyme glutathione transferase A1 (GSTA1) includes a dynamic C-terminal helix that presents an ensemble of active sites, and kinetic data suggest that different substrates select different conformations. Furthermore, crystallographic structures suggest that the C-terminus of GSTA1 adopts different locations with different substrates bound (18-21). Thus, it appears that GSTA1 utilizes both substrate-dependent conformational selection and substrate-dependent active site 'fits.' Based on the data here for the IF of P-gp, conformational selection is likely to contribute in the case of P-gp. Further studies are necessary to explore this and to determine the potential contribution of induced fit, and whether different substrates select or induce different conformations.

Figures

Table 3.1. Percent coverage of major domains of P-gp and number of peptides (total and bimodal) recovered for P-gp in detergent and nanodiscs.

	P-gp in detergent-lipid micelles	P-gp nanodiscs
Overall coverage (%)	40.1	37.7
TMD1 coverage (%)	15.6	13
TMD2 coverage (%)	19	15.7
NBD1 coverage (%)	76.2	73.8
NBD2 coverage (%)	64.2	62.7
Redundancy	2.2	1.55
Total peptides	91	59
Bimodal peptides (clearly resolved)	4	15

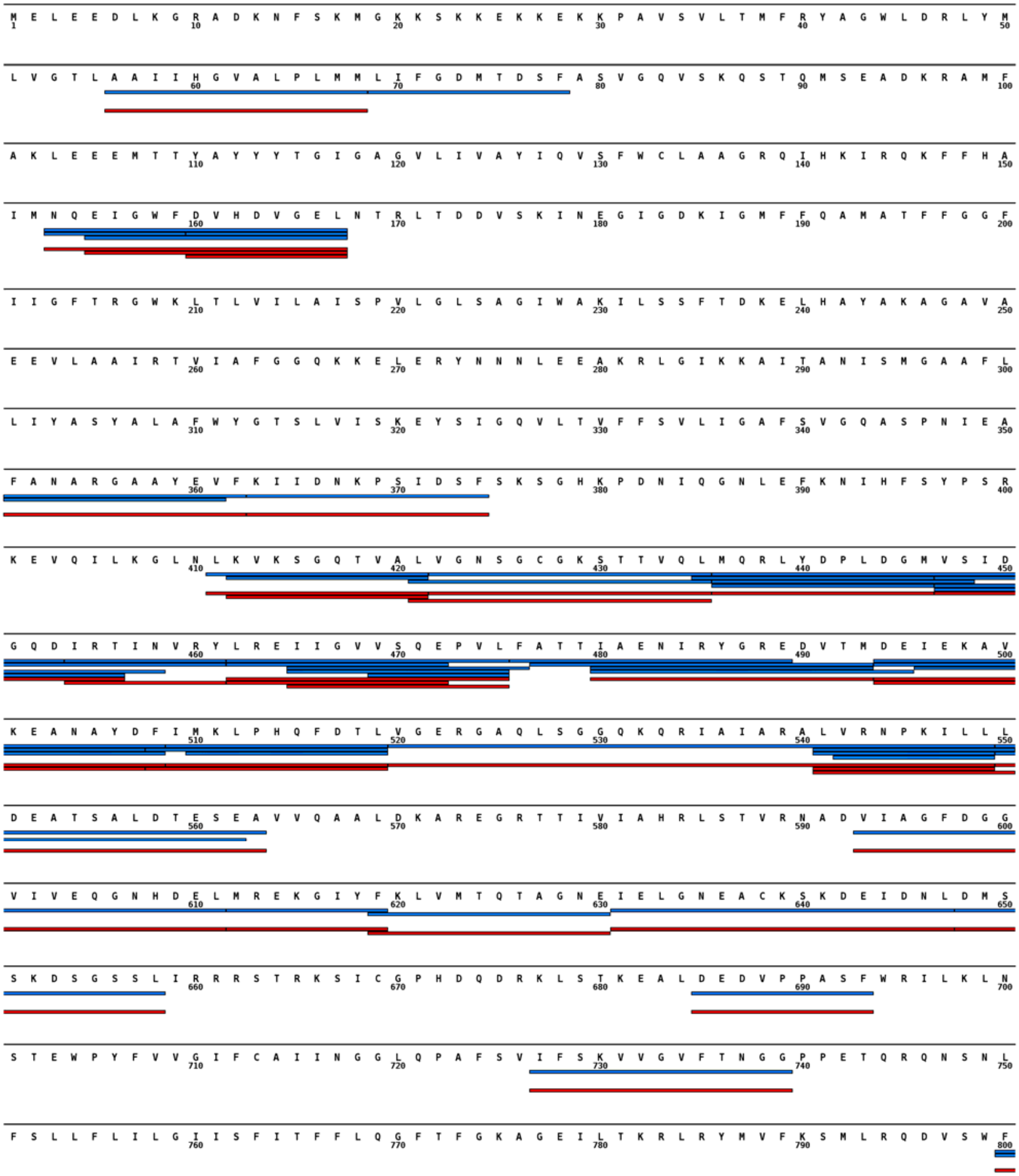M E L E E D L K G R A D K N F S K M G K K S K K E K K E K K P A V S V L T M F R Y A G W L D R L Y M
1 10 20 30 40 50
L V G T L A A I I H G V A L P L M M L I F G D M T D S F A S V G Q V S K Q S T Q M S E A D K R A M F
60 70 80 90 100
A K L E E E M T T Y A Y Y Y T G I G A G V L I V A Y I Q V S F W C L A A G R Q I H K I R Q K F F H A
110 120 130 140 150
I M N Q E I G W F D V H D V G E L N T R L T D D V S K I N E G I G D K I G M F F Q A M A T F F G G F
160 170 180 190 200
I I G F T R G W K L T L V I L A I S P V L G L S A G I W A K I L S S F T D K E L H A Y A K A G A V A
210 220 230 240 250
E E V L A A I R T V I A F G G Q K K E L E R Y N N N L E E A K R L G I K K A I T A N I S M G A A F L
260 270 280 290 300
L I Y A S Y A L A F W Y G T S L V I S K E Y S I G Q V L T V F F S V L I G A F S V G Q A S P N I E A
310 320 330 340 350
F A N A R G A A Y E V F K I I D N K P S I D S F S K S G H K P D N I Q G N L E F K N I H F S Y P S R
360 370 380 390 400
K E V Q I L K G L N L K V K S G Q T V A L V G N S G C G K S T T V Q L M Q R L Y D P L D G M V S I D
410 420 430 440 450
G Q D I R T I N V R Y L R E I I G V V S Q E P V L F A T T I A E N I R Y G R E D V T M D E I E K A V
460 470 480 490 500
K E A N A Y D F I M K L P H Q F D T L V G E R G A Q L S G G Q K Q R I A I A R A L V R N P K I L L L
510 520 530 540 550
D E A T S A L D T E S E A V V Q A A L D K A R E G R T T I V I A H R L S T V R N A D V I A G F D G G
560 570 580 590 600
V I V E Q G N H D E L M R E K G I Y F K L V M T Q T A G N E I E L G N E A C K S K D E I D N L D M S
610 620 630 640 650
S K D S G S S L I R R R S T R K S I C G P H D Q D R K L S T K E A L D E D V P P A S F W R I L K L N
660 670 680 690 700
S T E W P Y F V V G I F C A I I N G G L Q P A F S V I F S K V V G V F T N G G P P E T Q R Q N S N L
710 720 730 740 750
F S L L F L I L G I I S F I T F F L Q G F T F G K A G E I L T K R L R Y M V F K S M L R Q D V S W F
760 770 780 790 800

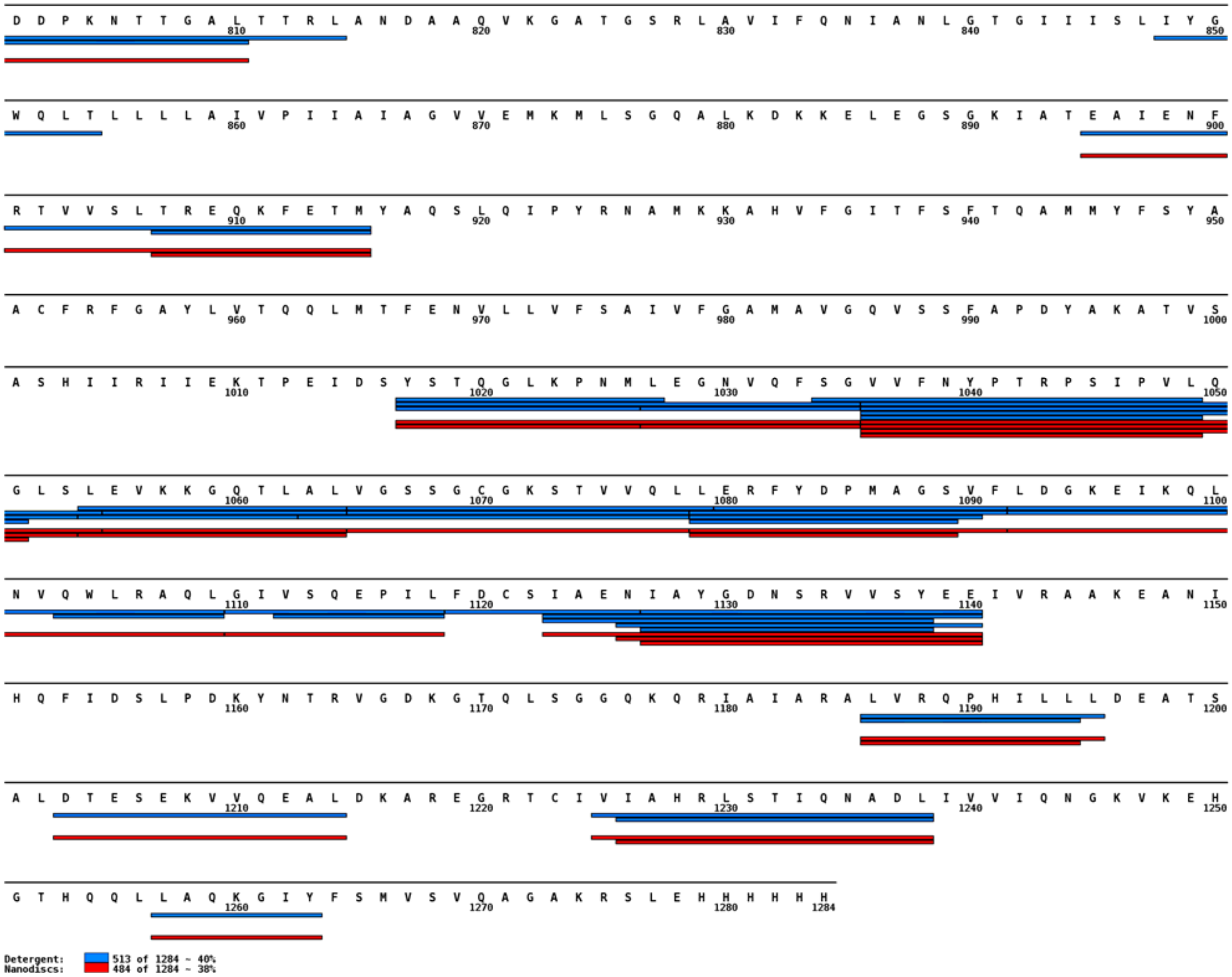

Figure 3.1. Peptide coverage map of P-gp. Recovered peptides of P-gp in detergent-lipid micelles (blue bars) and in nanodiscs (red bars) are shown below the primary sequence of P-gp (4Q9H). More peptides were observed for P-gp in detergent than in nanodiscs. Figure was created using MS Tools(22).

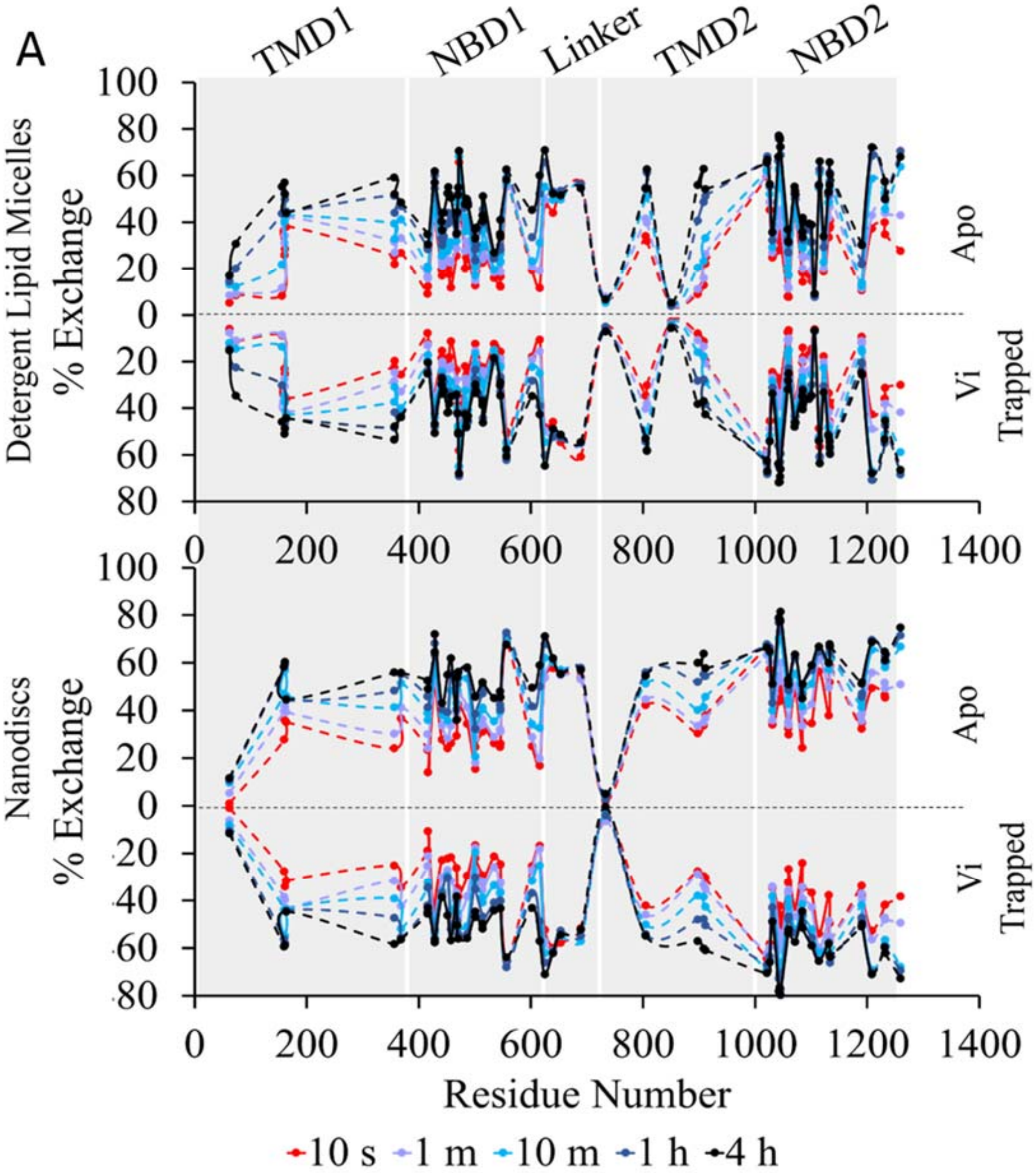
A
TMD1
NBD1
Linker
TMD2
NBD2
Detergent Lipid Micelles
% Exchange
Apo
Vi
Trapped
100
80
60
40
20
0
20
40
60
80
0
200
400
600
800
1000
1200
1400
Nanodiscs
% Exchange
Apo
Vi
Trapped
Residue Number
10 s
1 m
10 m
1 h
4 h

B

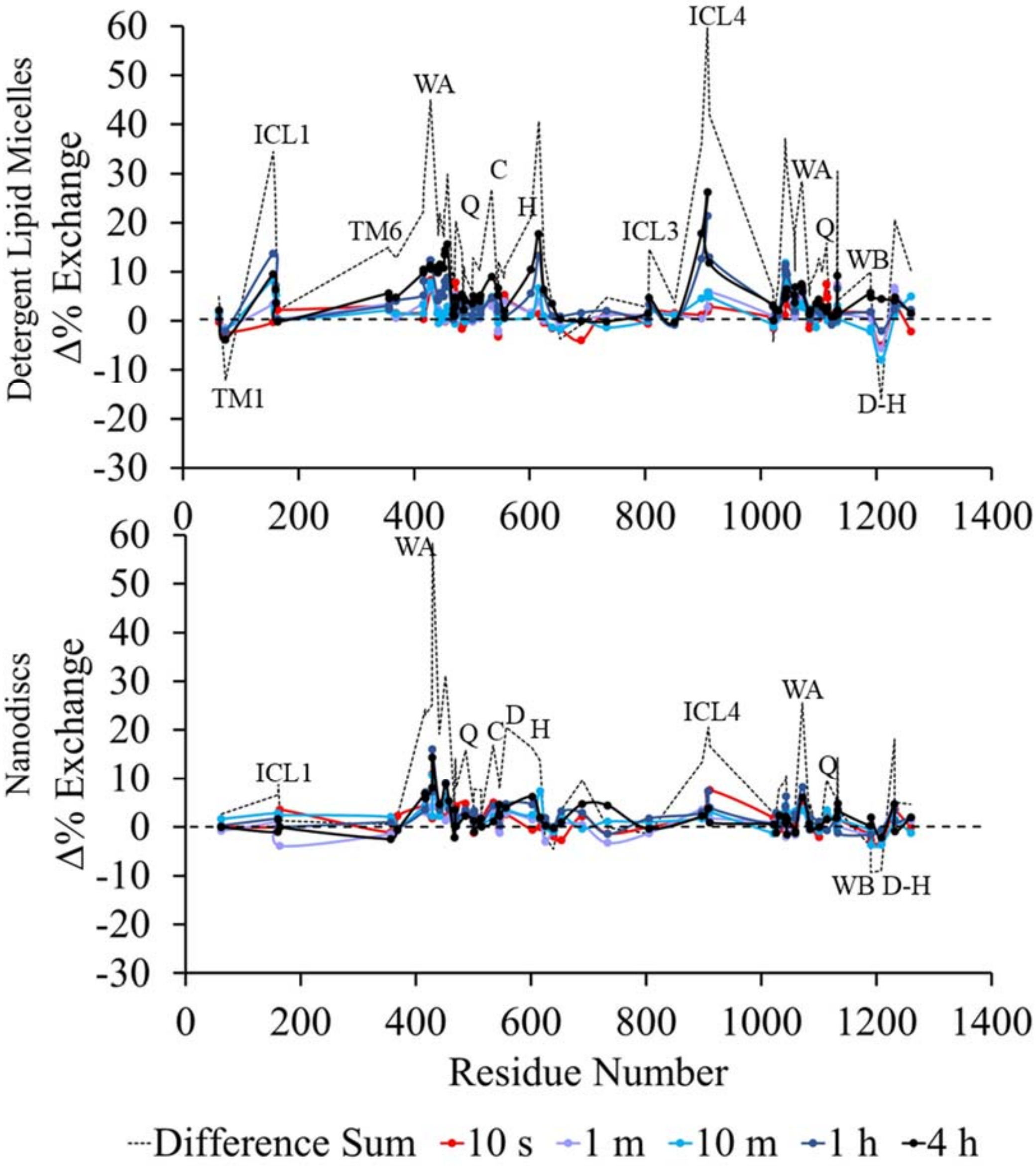

Detergent Lipid Micelles
Δ% Exchange
Nanodiscs
Δ% Exchange
Residue Number
60
50
40
30
20
10
0
-10
-20
-30
0
200
400
600
800
1000
1200
1400
ICL1
TM1
TM6
WA
Q
C
H
ICL3
ICL4
WA
Q
WB
D-H
ICL1
WA
Q
C
D
H
ICL4
WA
Q
WB
D-H
Difference Sum
10 s
1 m
10 m
1 h
4 h

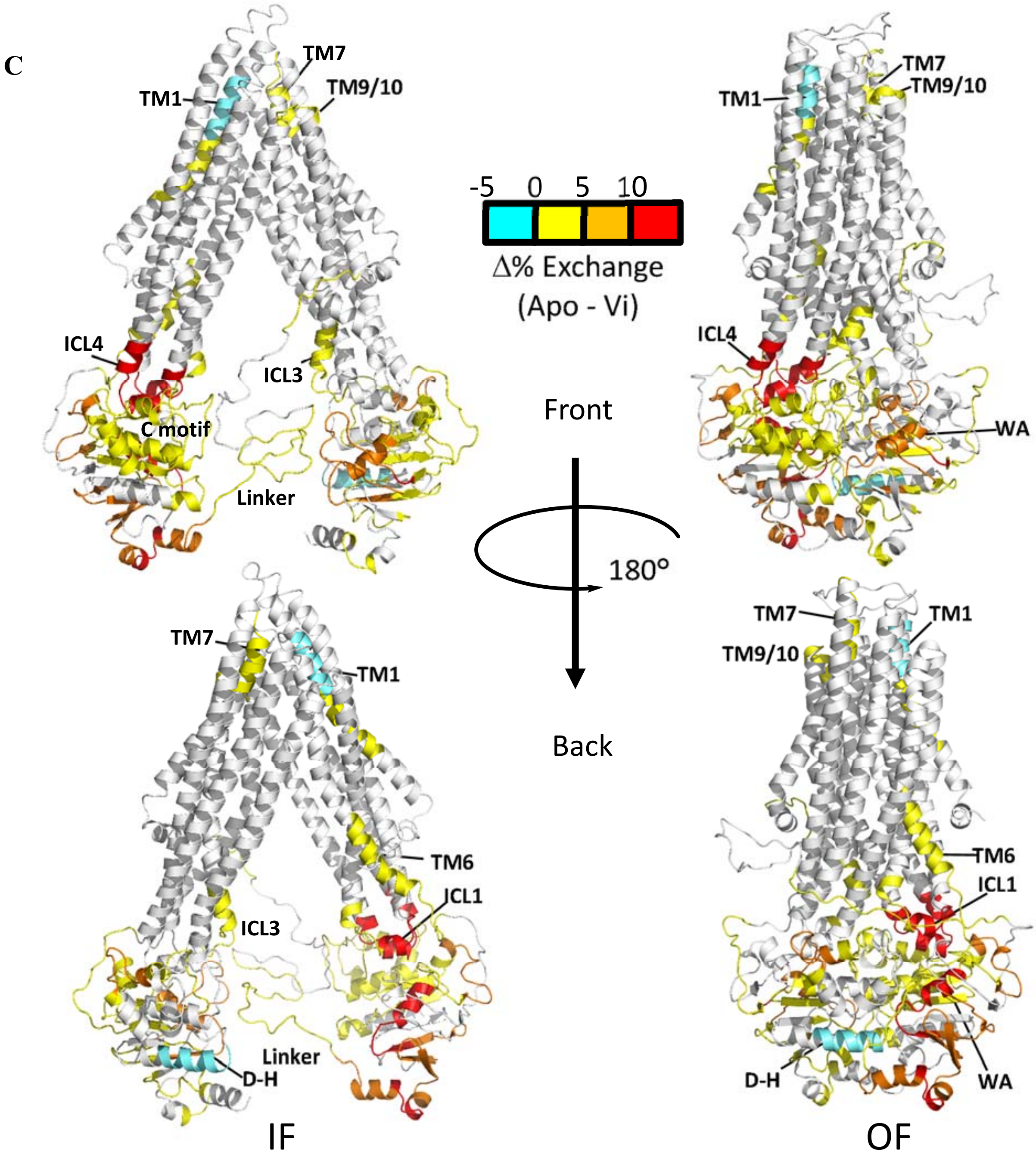
C
TM1
TM7
TM9/10
ICL4
ICL3
C motif
Linker
-5
0
5
10
Δ% Exchange
(Apo - Vi)
Front
180°
Back
TM1
TM7
TM9/10
ICL4
WA
TM7
TM1
TM6
ICL1
ICL3
Linker
D-H
IF
TM7
TM1
TM9/10
TM6
ICL1
D-H
WA
OF

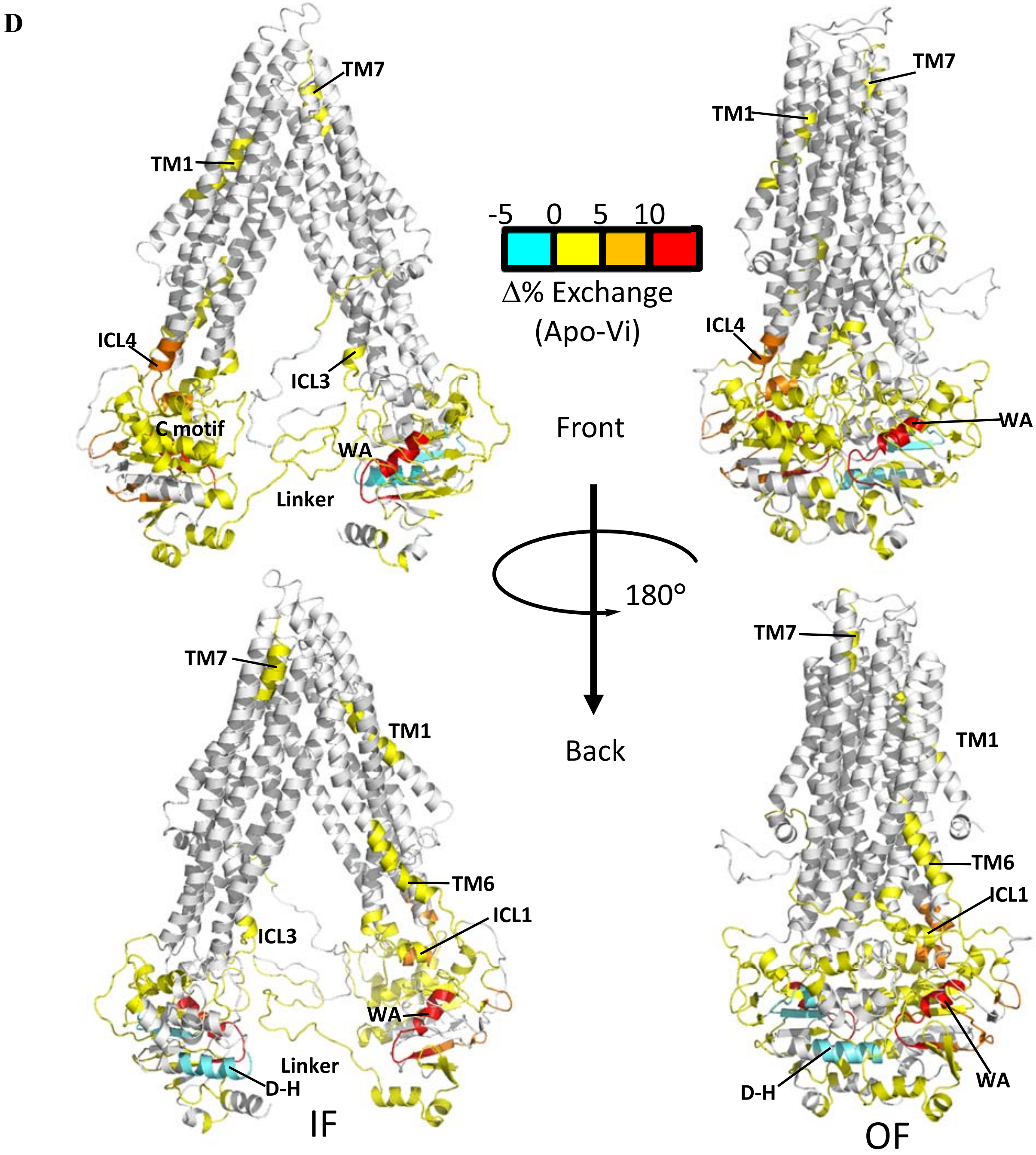
D
TM7
TM1
ICL4
ICL3
C motif
WA
Linker
-5 0 5 10
Δ% Exchange
(Apo-Vi)
Front
180°
Back
TM7
TM1
ICL4
WA
TM7
TM1
TM6
ICL1
ICL3
WA
Linker
D-H
IF
TM7
TM1
TM6
ICL1
D-H
WA
OF

Figure 3.2. HDX comparison of apo P-gp versus vanadate trapped P-gp in detergent lipid micelles or nanodiscs. (A) Butterfly plots showing hydrogen/deuterium exchange profiles of P-gp in either micelles (top butterfly plot) or nanodiscs (bottom butterfly plot). Each plot compares the deuterium uptake profile for the apo P-gp with the vanadate-trapped state and percent deuterium uptake is plotted at the midpoint of the peptide sequence. Solid connecting lines indicate continuous coverage, whereas dotted lines reflect missing sequence coverage. (B) Difference deuterium exchange profile of P-gp peptides in apo P-gp and vanadate-trapped P-gp (apo minus vi-trapped = Δ% exchange) at varying times of exposure to D_2O. Dotted line represents the sum of differences between the two conditions across all time points, and thus the cumulative difference in deuterium exchange. Positive values or negative values indicate regions of P-gp that become more or less protected in the vanadate-trapped state respectively. (C) Difference in solvent accessibility between the apo and vi-trapped states for P-gp detergent micelles at 1 hour, mapped onto P-gp structures in the inward- and outward-facing conformations (IF and OF; PDB: 49QH (murine p-gp) and PMDB: PM0075213 (human P-gp based on SAV1866 OF conformation)). Regions in P-gp that become moderately exposed (cyan, 0 to -5%), moderately protected (yellow, 0-5%), highly protected (orange and red, >5 and >10%) in the vanadate-trapped state relative to the apo state are shown. Structures are rotated 180º and shown in the lower panel. (D) Same as (C) but for P-gp nanodiscs. Abbreviations used: TMH, trans membrane helix; NBD, nucleotide binding domain; WA, Walker-Ames motif; ICL, intracellular loop; D-H, D and H loops).

A

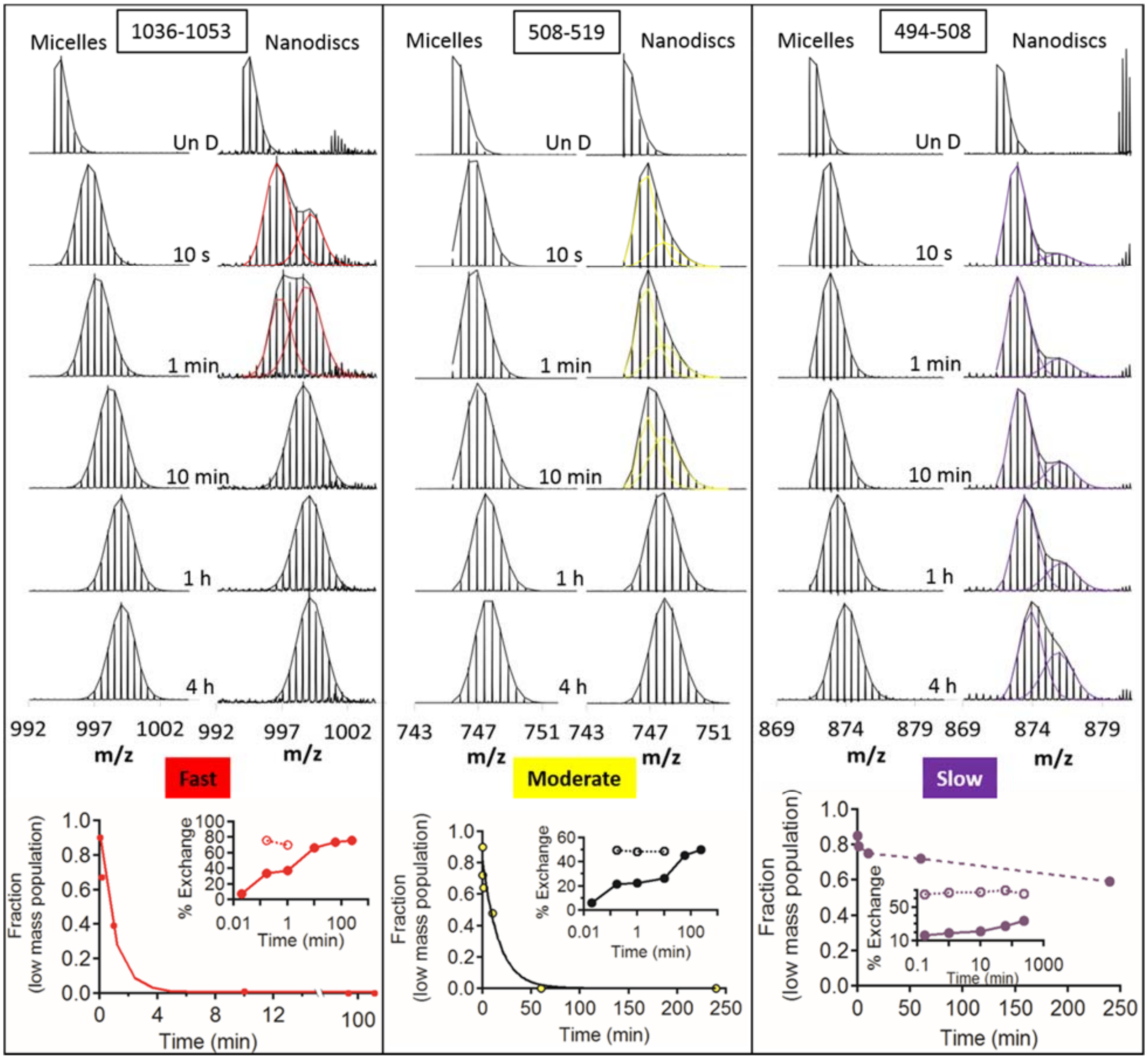
Micelles
1036-1053
Nanodiscs
Un D
10 s
1 min
10 min
1 h
4 h
992
997
1002
992
997
1002
m/z
m/z
Fast
Fraction (low mass population)
Time (min)
% Exchange
Time (min)
Micelles
508-519
Nanodiscs
743
747
751
743
747
751
m/z
m/z
Moderate
Micelles
494-508
Nanodiscs
869
874
879
869
874
879
m/z
m/z
Slow

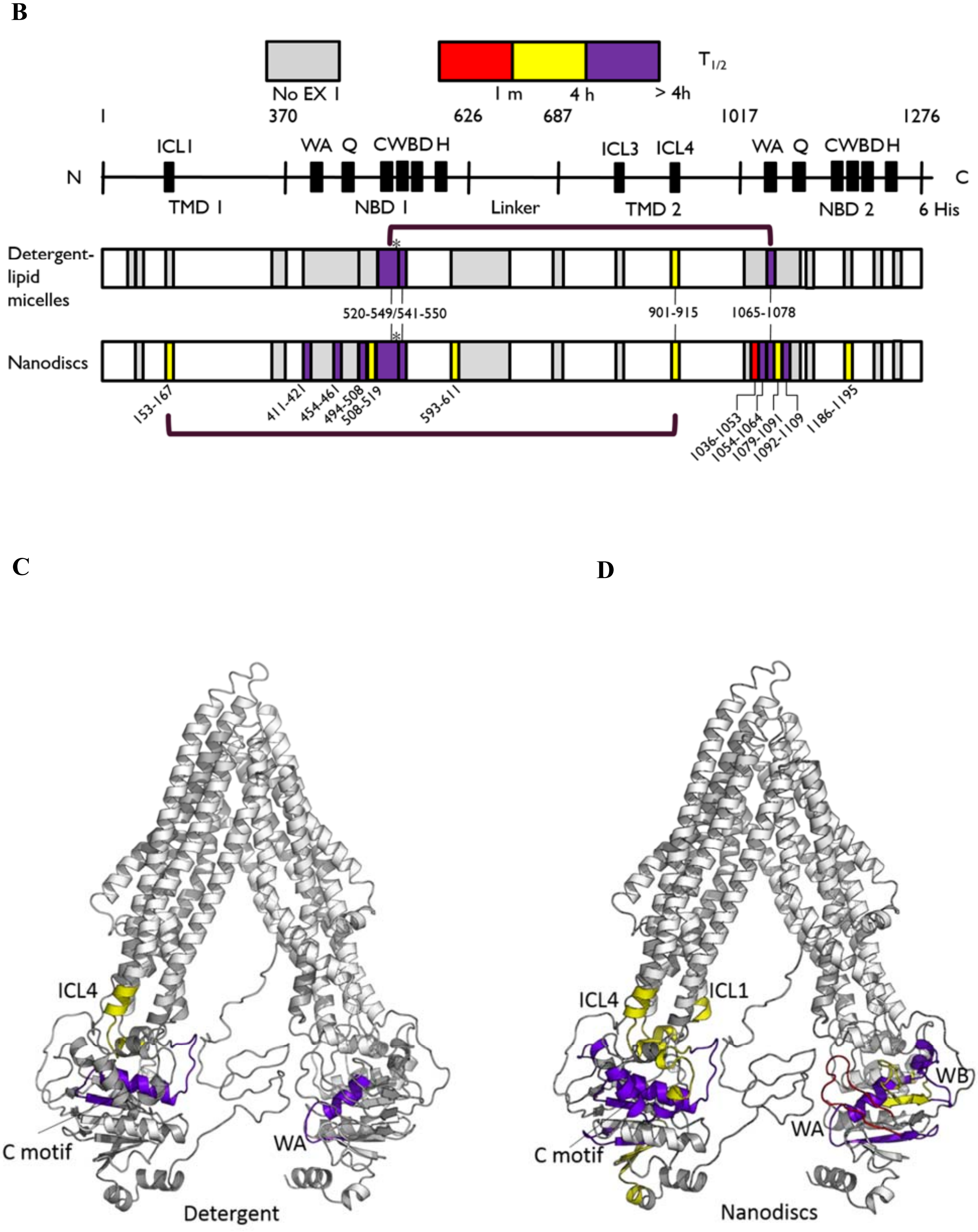
B
No EX I
1 m
4 h
> 4h
T1/2
1
370
626
687
1017
1276
ICL1
WA
Q
CWBDH
ICL3
ICL4
WA
Q
CWBDH
N
C
TMD 1
NBD 1
Linker
TMD 2
NBD 2
6 His
Detergent-lipid micelles
520-549/541-550
901-915
1065-1078
Nanodiscs
153-167
411-421
454-461
494-508
508-519
593-611
1036-1053
1054-1064
1079-1091
1092-1109
1186-1195
C
D
ICL4
C motif
WA
Detergent
ICL4
ICL1
C motif
WA
WB
Nanodiscs

Figure 3.3. Peptides displaying EX1-related kinetics in P-gp lipid-detergent micelles or nanodiscs. (A) Representative isotopic mass envelopes of peptides (residues labeled at top of the panels) with bimodal kinetics in nanodiscs (right) but not in lipid-detergent micelles (left). Rates of relaxation are measured by fitting the decay of the low mass population to a single exponential function (bottom graph in each panel, data from nanodiscs), and peptides are categorized into fast (red), moderate (yellow), and slow (purple) based on relaxation half-lives. Inset: The centroid of the low and high mass distributions was used to plot the deuterium uptake for the two populations (low mass- solid line; high mass-dashed line). (B) Diagram comparing the localization of bimodal peptides across the linear sequence for P-gp in lipid-detergent micelles or nanodiscs. Peptides are colored according to relaxation half-lives (fast-red, moderate-yellow, slow-purple). Regions colored gray did not show EX1-like behavior under experimental conditions. Lines indicate pairs of distant peptides based on the primary sequence of P-gp but are in close proximity/interact with each other in the tertiary structure of P-gp. (C) and (D) Location of these peptides plotted onto the IF conformation of P-gp for lipid-detergent micelles or nanodiscs respectively.

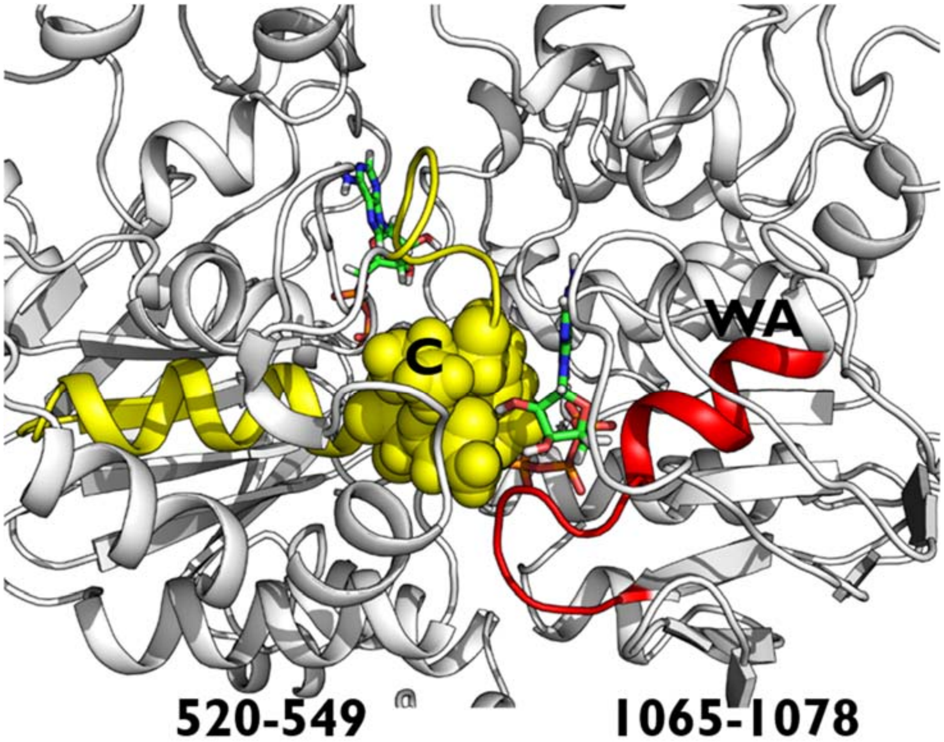

Figure 3.4. Bimodal peptides 520-549 (containing C motif, yellow spheres) and 1065-1078 (containing WA motif, red) found in P-gp in detergent and nanodiscs. The peptides from NBD1 and NBD2 interact with each other to form a sandwich dimer in the presence of nucleotide (ATP, carbon, phosphorus, nitrogen and oxygen atoms shown in green, orange, blue and red respectively).

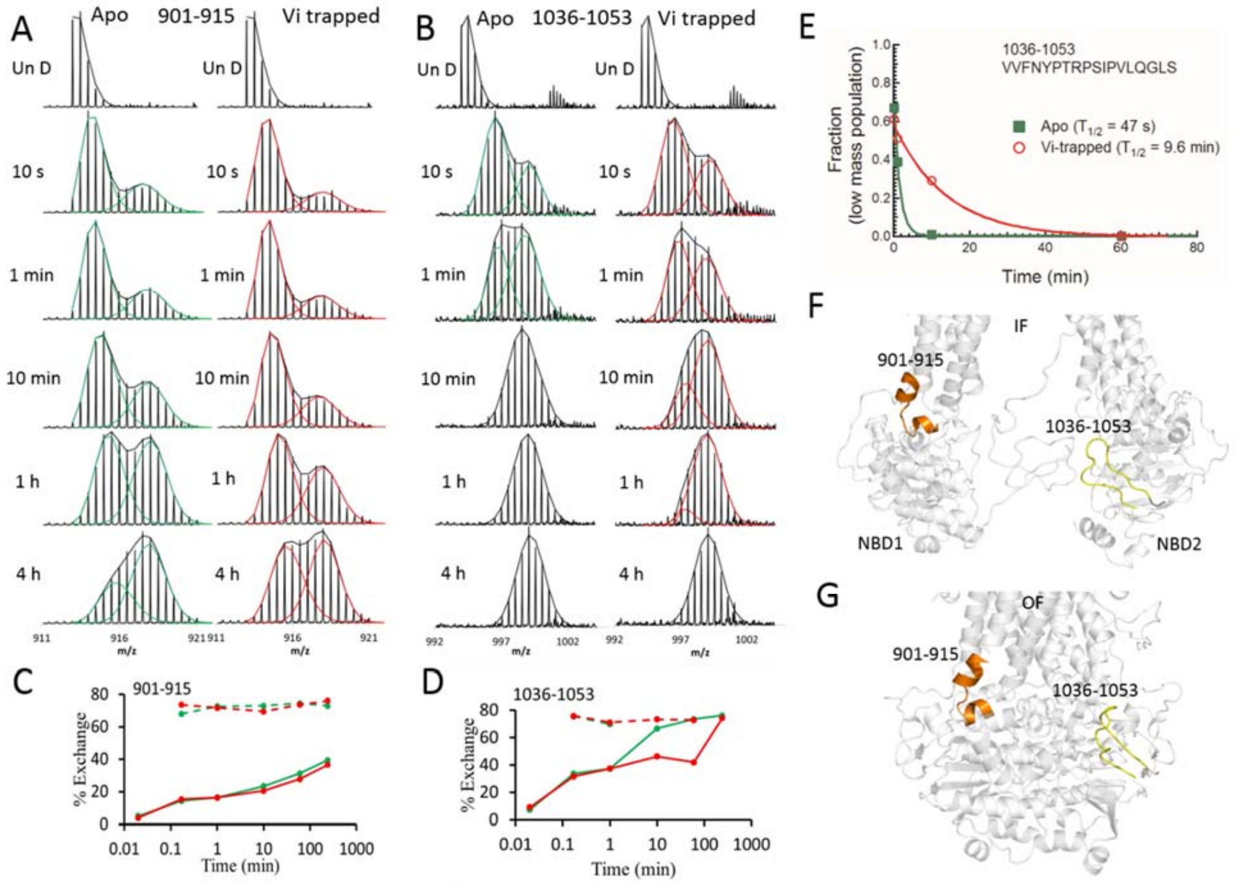

Figure 3.5. (A-D) Mass spectra and deuterium uptake plots for specific peptides in the apo (green) and vanadate trapped (red) states, with residues indicated at the top of each plot. Peptides with EX1 kinetics display bimodal isotopic distributions, which can be fitted with two Gaussian distributions. The centroid of these distributions was used to plot the deuterium uptake for the low (solid line) and high mass (dashed line) populations. (E) Kinetics of unfolding in the two states determined by plotting fraction of low mass population over time, for peptide 1036-1053. (F-G) Localization of these peptides in inward- or outward facing P-gp; yellow or orange indicates modest to high solvent protection (or increased rigidity) in the vanadate trapped state relative to the apo state.

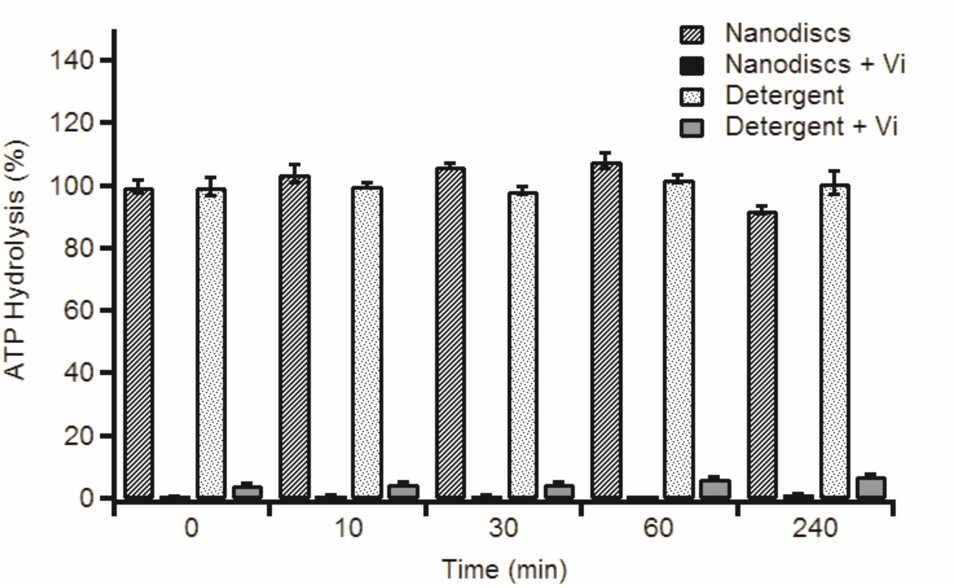

Figure 3.6. Functional activity of P-gp in detergent or nanodiscs during HDX time points. P-gp in lipid-detergent micelles or nanodiscs was incubated at 25ºC for varying duration, before initiation of reaction by addition of assay buffer (50 mM Tris, 150 mM NH_4Cl, 5 mM $MgSO_4$, 0.02% NaN_3, 100μM verapamil, 1 mM ATP, pH 7.4) with or without 240 μM Vi for 30 minutes at 37ºC, and Pi released was measured by a colorimetric assay (Chifflet). Activity is depicted as % of the control ATPase activity without prior preincubation, which is 604 nmol/min/mg for nanodiscs and 233 nmol/min/mg for detergent micelles. Error bar represents standard deviation of triplicates.

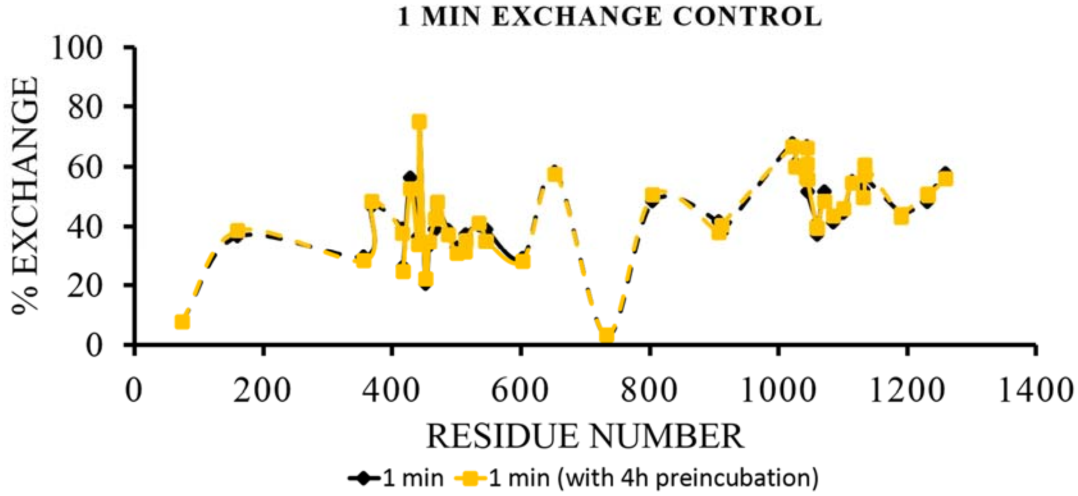

Figure 3.7. Comparison of H/DX with and without 4 hour pre-incubation in buffer. The percent deuterium uptake by P-gp nanodiscs at 1 minute, before and after 4-hr pre-incubation at 25ºC, were identical to each other, indicating that P-gp is structurally stable during HD exchange. The same peptides were observed for both data sets, and the peak ion intensities of the peptides were mostly similar, with 83% of the peptides not having CV exceeding 30% (Coefficient of variation, CV = standard deviation of peptide ion intensities/ mean of peptide ion intensities). This suggests minimal sample aggregation over 4 hours.

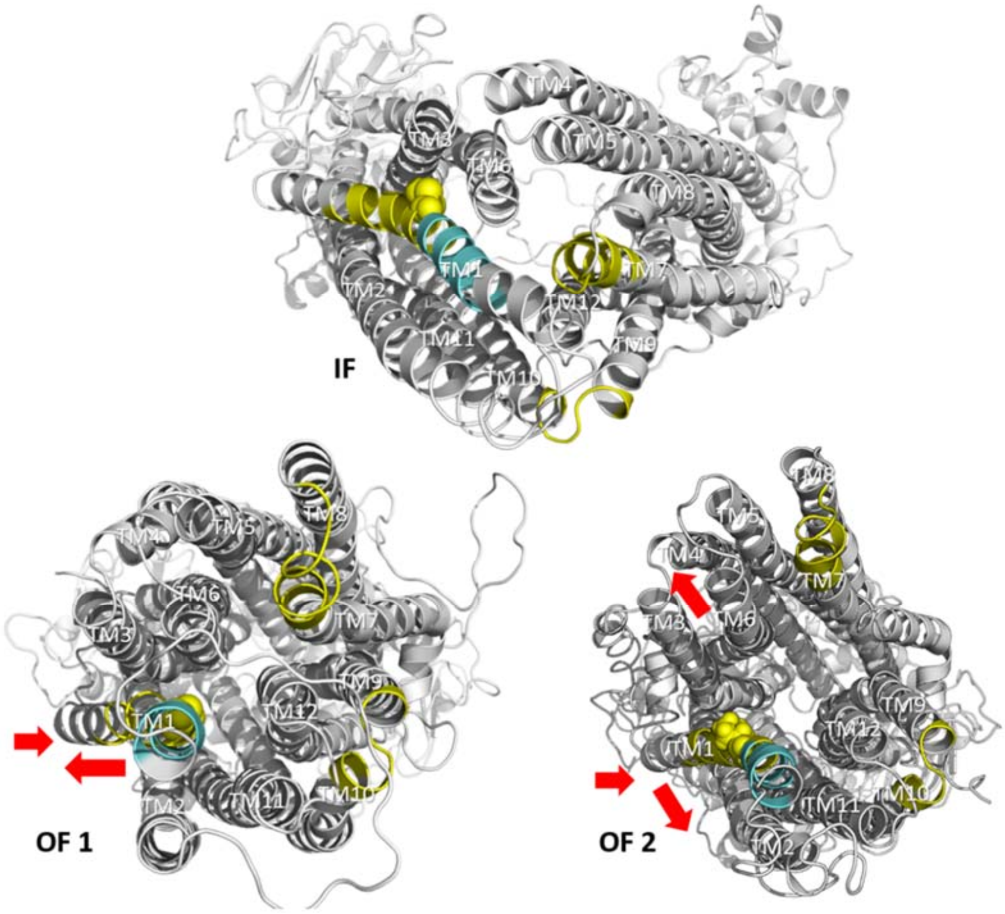

Figure 3.8. Rearrangements of TM1 and neighboring helices as P-gp switches from IF to OF conformations. Top: P-gp in the apo state, in IF conformation (PDB 4Q9H). Regions that are more solvent-exposed in the apo state are shown in yellow and regions that are more solvent-exposed in the vi-trapped state are shown in light blue. Proline kink at position 66, displayed as spheres. OF structures obtained from homology modelling of P-gp using SAV1866, OF1: PMDB PM0075213; OF2: from (16). Red arrows indicate possible movements of the TM helices. In OF 1, the yellow region of TM1 moves towards the central hydrophobic core of P-gp and becomes more solvent protected, whereas the blue region moves away from the core and becomes more solvent exposed. Alternatively, in OF 2, movement of other helices such as TM6 away from the hydrophobic core may also result in the top region of TM1 becoming more solvent exposed during a conformational change.

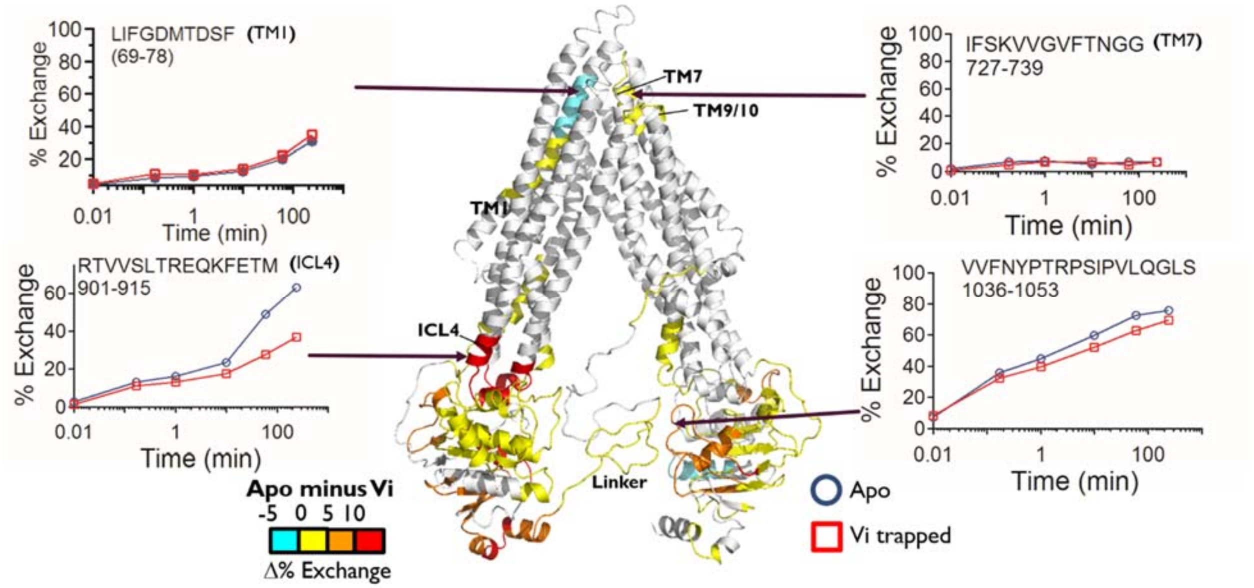

Figure 3.9. Exchange profiles at selected regions of P-gp. Note the relatively lower deuterium uptake at the TMHs, and higher deuterium uptake at the ICL and NBD. Overall, the warmer colors highlight regions of P-gp that are more solvent-exposed in the apo state than in the vanadate-trapped state. Of particular interest is the peptide 69-78 located in TM1, where the vanadate-trapped state (red) is more solvent-exposed than the apo state (blue).

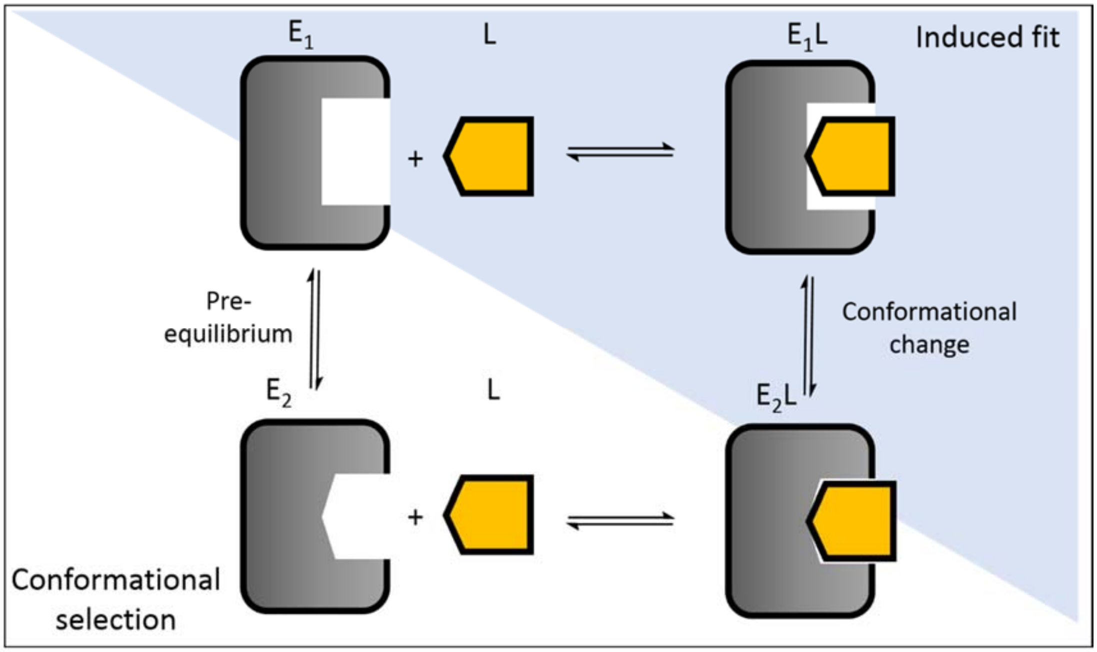

Figure 3.10. Induced fit and conformational selection models for an enzyme and a substrate. The induced fit model (shaded blue) postulates that the binding of a ligand results in a conformational transition of E_1 to E_2 that optimizes binding. In the case of conformational selection (not shaded), the enzyme exist in a dynamic equilibria of two or more conformations, and only one form of the enzyme (shown as E_2) binds to the ligand. Kinetic and thermodynamic studies are required to determine the mechanism of ligand binding for P-gp.

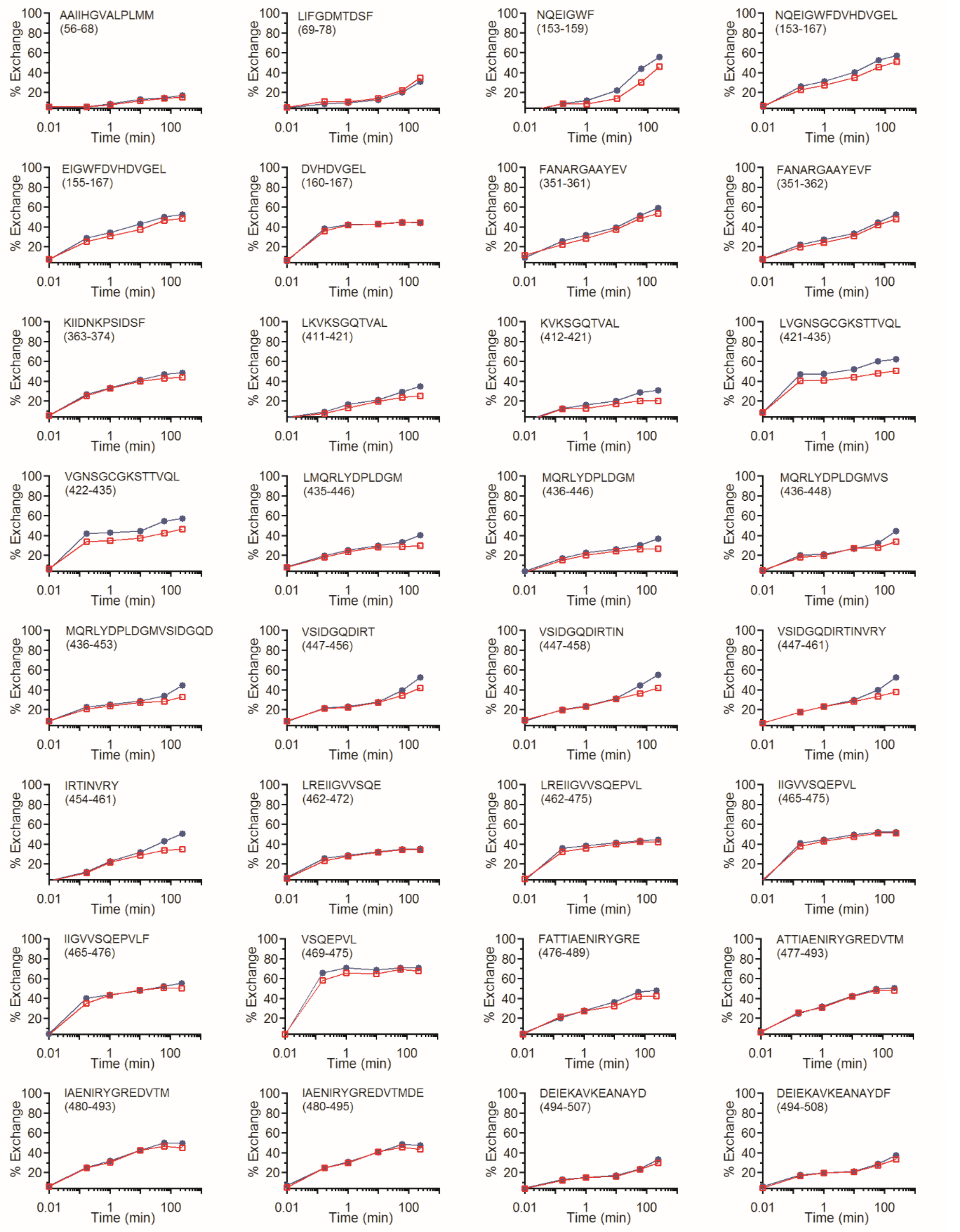
% Exchange
Time (min)
0.01
1
100
20
40
60
80
100
AAIIHGVALPLMM
(56-68)
LIFGDMTDSF
(69-78)
NQEIGWF
(153-159)
NQEIGWFDVHDVGEL
(153-167)
EIGWFDVHDVGEL
(155-167)
DVHDVGEL
(160-167)
FANARGAAYEV
(351-361)
FANARGAAYEVF
(351-362)
KIIDNKPSIDSF
(363-374)
LKVKSGQTVAL
(411-421)
KVKSGQTVAL
(412-421)
LVGNSGCGKSTTVQL
(421-435)
VGNSGCGKSTTVQL
(422-435)
LMQRLYDPLDGM
(435-446)
MQRLYDPLDGM
(436-446)
MQRLYDPLDGMVS
(436-448)
MQRLYDPLDGMVSIDGQD
(436-453)
VSIDGQDIRT
(447-456)
VSIDGQDIRTIN
(447-458)
VSIDGQDIRTINVRY
(447-461)
IRTINVRY
(454-461)
LREIIGVVSQE
(462-472)
LREIIGVVSQEPVL
(462-475)
IIGVVSQEPVL
(465-475)
IIGVVSQEPVLF
(465-476)
VSQEPVL
(469-475)
FATTIAENIRYGRE
(476-489)
ATTIAENIRYGREDVTM
(477-493)
IAENIRYGREDVTM
(480-493)
IAENIRYGREDVTMDE
(480-495)
DEIEKAVKEANAYD
(494-507)
DEIEKAVKEANAYDF
(494-508)

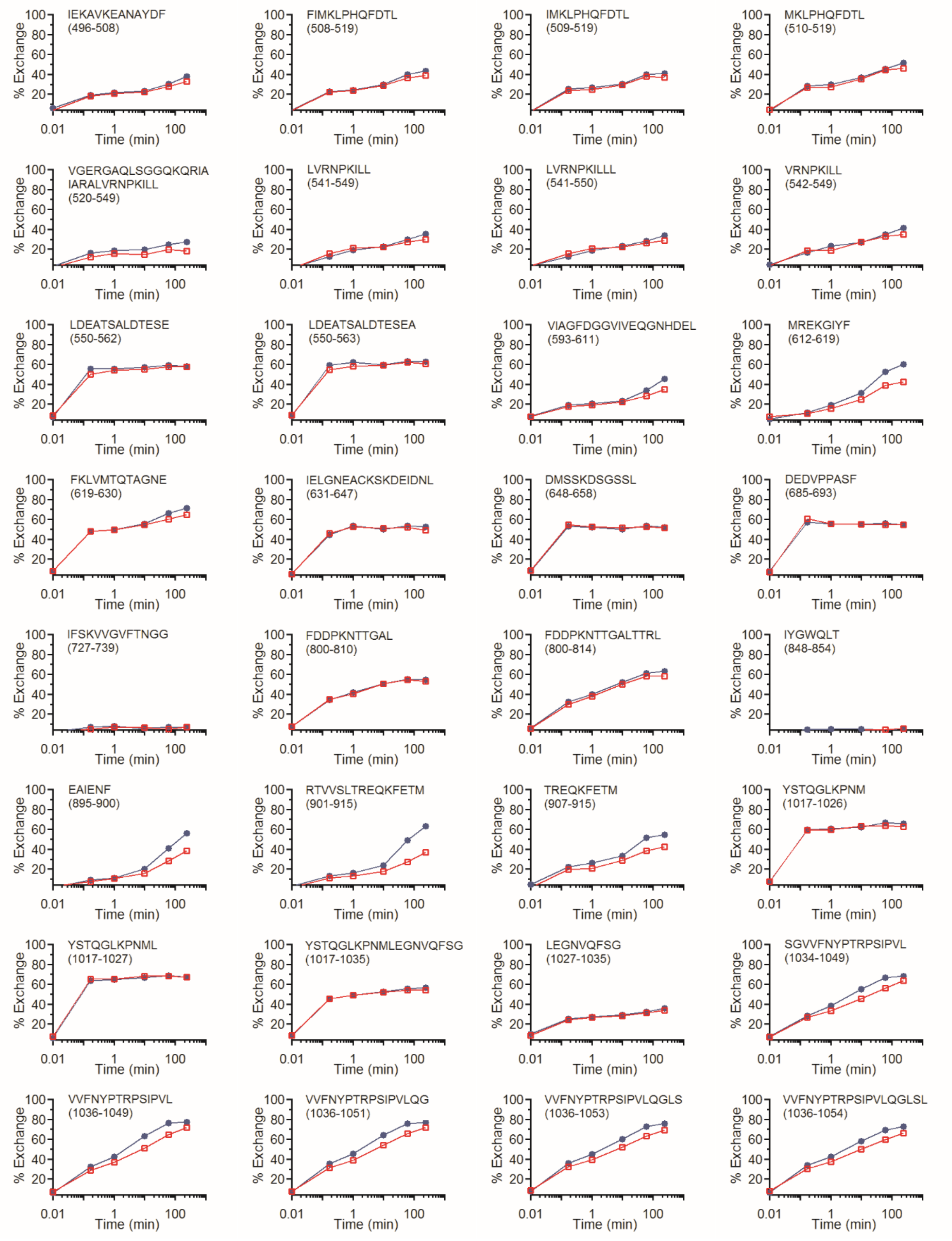
% Exchange
Time (min)
0.01
1
100
20
40
60
80
100
IEKAVKEANAYDF (496-508)
FIMKLPHQFDTL (508-519)
IMKLPHQFDTL (509-519)
MKLPHQFDTL (510-519)
VGERGAQLSGGQKQRIA IARALVRNPKILL (520-549)
LVRNPKILL (541-549)
LVRNPKILLL (541-550)
VRNPKILL (542-549)
LDEATSALDTESE (550-562)
LDEATSALDTESEA (550-563)
VIAGFDGGVIVEQGNHDEL (593-611)
MREKGIYF (612-619)
FKLVMTQTAGNE (619-630)
IELGNEACKSKDEIDNL (631-647)
DMSSKDSGSSL (648-658)
DEDVPPASF (685-693)
IFSKVVGVFTNGG (727-739)
FDDPKNTTGAL (800-810)
FDDPKNTTGALTTRL (800-814)
IYGWQLT (848-854)
EAIENF (895-900)
RTVVSLTREQKFETM (901-915)
TREQKFETM (907-915)
YSTQGLKPNM (1017-1026)
YSTQGLKPNML (1017-1027)
YSTQGLKPNMLEGNVQFSG (1017-1035)
LEGNVQFSG (1027-1035)
SGVVFNYPTRPSIPVL (1034-1049)
VVFNYPTRPSIPVL (1036-1049)
VVFNYPTRPSIPVLQG (1036-1051)
VVFNYPTRPSIPVLQGLS (1036-1053)
VVFNYPTRPSIPVLQGLSL (1036-1054)

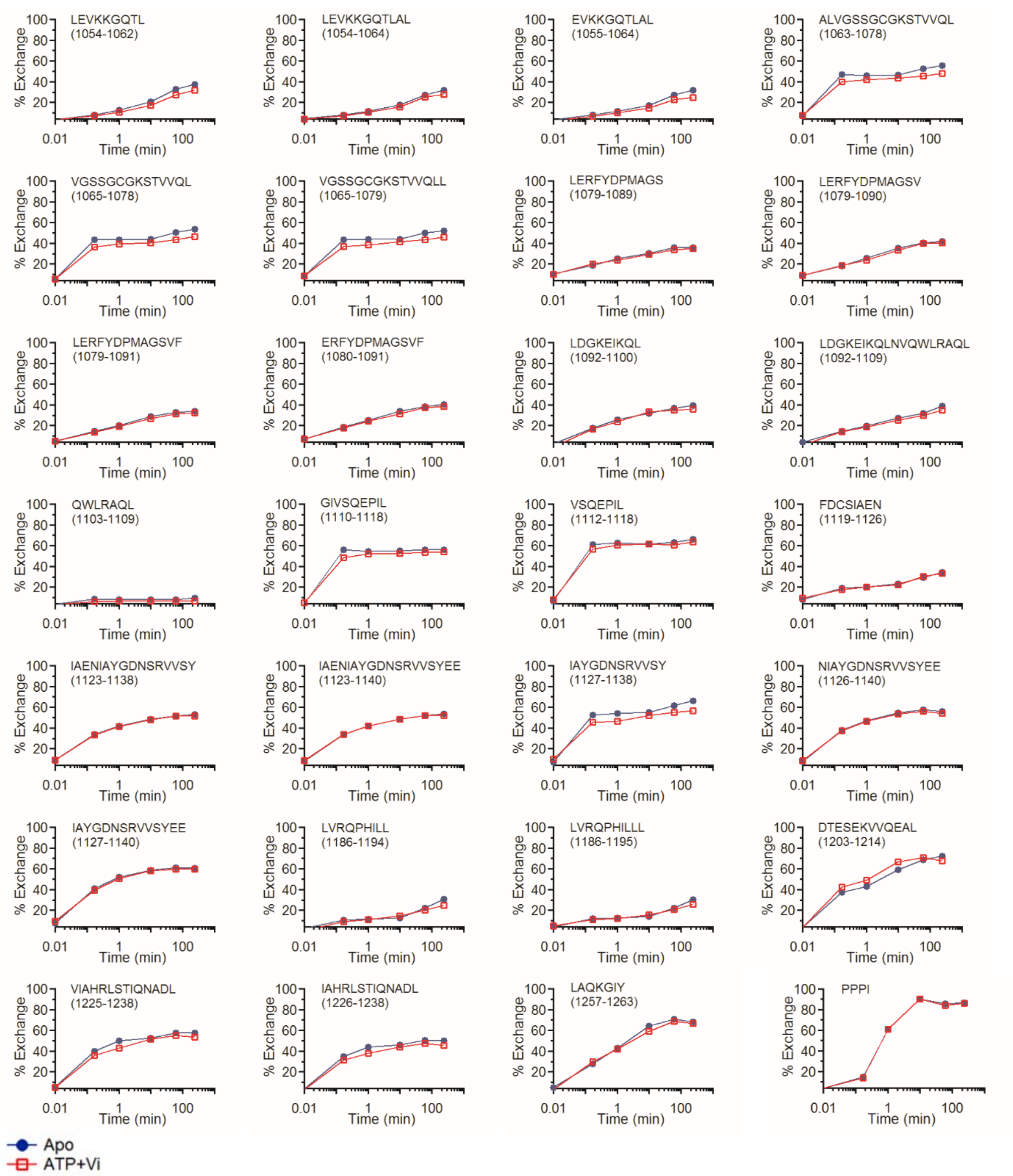

Figure 3.11. Individual uptake plots for all recovered peptides of P-gp in detergent-lipid micelles, comparing the apo (blue, solid circles) and vanadate-trapped states (red, open squares). Each plot represents the average from multiple charged states and the average percent deuterium exchange was calculated by dividing the observed deuterium uptake by the theoretical maximum deuterium

uptake for each peptide ((number of residues – number of prolines -1)*final fraction of D_2O during exchange). PPPI is used as an internal standard and the uptake plot indicates identical exchange conditions between the two states (last plot).

3.5 References

1. Dawson, R. J., and Locher, K. P. (2007) Structure of the multidrug ABC transporter Sav1866 from Staphylococcus aureus in complex with AMP-PNP. *FEBS Lett* **581**, 935-938
2. Mishra, S., Verhalen, B., Stein, R. A., Wen, P. C., Tajkhorshid, E., and McHaourab, H. S. (2014) Conformational dynamics of the nucleotide binding domains and the power stroke of a heterodimeric ABC transporter. *Elife* **3**, e02740
3. Ward, A., Reyes, C. L., Yu, J., Roth, C. B., and Chang, G. (2007) Flexibility in the ABC transporter MsbA: Alternating access with a twist. *Proc Natl Acad Sci U S A* **104**, 19005-19010
4. Frank, G. A., Shukla, S., Rao, P., Borgnia, M. J., Bartesaghi, A., Merk, A., Mobin, A., Esser, L., Earl, L. A., Gottesman, M. M., Xia, D., Ambudkar, S. V., and Subramaniam, S. (2016) Cryo-EM Analysis of the Conformational Landscape of Human P-glycoprotein (ABCB1) During its Catalytic Cycle. *Mol Pharmacol* **90**, 35-41
5. Verhalen, B., Ernst, S., Borsch, M., and Wilkens, S. (2012) Dynamic ligand-induced conformational rearrangements in P-glycoprotein as probed by fluorescence resonance energy transfer spectroscopy. *J Biol Chem* **287**, 1112-1127
6. Wen, P. C., Verhalen, B., Wilkens, S., McHaourab, H. S., and Tajkhorshid, E. (2013) On the origin of large flexibility of P-glycoprotein in the inward-facing state. *J Biol Chem* **288**, 19211-19220
7. Urbatsch, I. L., Sankaran, B., Weber, J., and Senior, A. E. (1995) P-glycoprotein is stably inhibited by vanadate-induced trapping of nucleotide at a single catalytic site. *J Biol Chem* **270**, 19383-19390
8. Urbatsch, I. L., Tyndall, G. A., Tombline, G., and Senior, A. E. (2003) P-glycoprotein catalytic mechanism: studies of the ADP-vanadate inhibited state. *J Biol Chem* **278**, 23171-23179
9. Esser, L., Zhou, F., Pluchino, K. M., Shiloach, J., Ma, J., Tang, W. K., Gutierrez, C., Zhang, A., Shukla, S., Madigan, J. P., Zhou, T., Kwong, P. D., Ambudkar, S. V., Gottesman, M. M., and Xia, D. (2017) Structures of the Multidrug Transporter P-glycoprotein Reveal Asymmetric ATP Binding and the Mechanism of Polyspecificity. *J Biol Chem* **292**, 446-461
10. Moeller, A., Lee, S. C., Tao, H., Speir, J. A., Chang, G., Urbatsch, I. L., Potter, C. S., Carragher, B., and Zhang, Q. (2015) Distinct conformational spectrum of homologous multidrug ABC transporters. *Structure* **23**, 450-460

11. Pan, L., and Aller, S. G. (2015) Equilibrated atomic models of outward-facing P-glycoprotein and effect of ATP binding on structural dynamics. *Sci Rep* **5**, 7880
12. Jin, M. S., Oldham, M. L., Zhang, Q., and Chen, J. (2012) Crystal structure of the multidrug transporter P-glycoprotein from Caenorhabditis elegans. *Nature* **490**, 566-569
13. Ward, A. B., Szewczyk, P., Grimard, V., Lee, C. W., Martinez, L., Doshi, R., Caya, A., Villaluz, M., Pardon, E., Cregger, C., Swartz, D. J., Falson, P. G., Urbatsch, I. L., Govaerts, C., Steyaert, J., and Chang, G. (2013) Structures of P-glycoprotein reveal its conformational flexibility and an epitope on the nucleotide-binding domain. *Proc Natl Acad Sci U S A* **110**, 13386-13391
14. Callaghan, R., Berridge, G., Ferry, D. R., and Higgins, C. F. (1997) The functional purification of P-glycoprotein is dependent on maintenance of a lipid-protein interface. *Biochim Biophys Acta* **1328**, 109-124
15. Lerner-Marmarosh, N., Gimi, K., Urbatsch, I. L., Gros, P., and Senior, A. E. (1999) Large scale purification of detergent-soluble P-glycoprotein from Pichia pastoris cells and characterization of nucleotide binding properties of wild-type, Walker A, and Walker B mutant proteins. *J Biol Chem* **274**, 34711-34718
16. Li, M. J., Nath, A., and Atkins, W. M. (2017) Differential Coupling of Binding, ATP Hydrolysis, and Transport of Fluorescent Probes with P-Glycoprotein in Lipid Nanodiscs. *Biochemistry* **56**, 2506-2517
17. Chifflet, S., Torriglia, A., Chiesa, R., and Tolosa, S. (1988) A method for the determination of inorganic phosphate in the presence of labile organic phosphate and high concentrations of protein: application to lens ATPases. *Anal Biochem* **168**, 1-4
18. Zhan, Y., and Rule, G. S. (2004) Glutathione induces helical formation in the carboxy terminus of human glutathione transferase A1-1. *Biochemistry* **43**, 7244-7254
19. Le Trong, I., Stenkamp, R. E., Ibarra, C., Atkins, W. M., and Adman, E. T. (2002) 1.3-A resolution structure of human glutathione S-transferase with S-hexyl glutathione bound reveals possible extended ligandin binding site. *Proteins* **48**, 618-627
20. Grahn, E., Novotny, M., Jakobsson, E., Gustafsson, A., Grehn, L., Olin, B., Madsen, D., Wahlberg, M., Mannervik, B., and Kleywegt, G. J. (2006) New crystal structures of human glutathione transferase A1-1 shed light on glutathione binding and the conformation of the C-terminal helix. *Acta Crystallogr D Biol Crystallogr* **62**, 197-207
21. Honaker, M. T., Acchione, M., Zhang, W., Mannervik, B., and Atkins, W. M. (2013) Enzymatic detoxication, conformational selection, and the role of molten globule active sites. *J Biol Chem* **288**, 18599-18611
22. Kavan, D., and Man, P. (2011) MSTools—Web based application for visualization and presentation of HXMS data. *International Journal of Mass Spectrometry* **302**, 53-58

Chapter 4

Applications of Lipid Nanodiscs for the Study of Membrane Proteins by Surface Plasmon Resonance

Parts of this chapter are taken from the published manuscript:

Trahey, M., Li, M. J., Kwon, H., Woodahl, E. L., McClary, W. D., and Atkins, W. M. (2015) Applications of Lipid Nanodiscs for the Study of Membrane Proteins by Surface Plasmon Resonance. *Curr Protoc Protein Sci* **81**, 29 13 21-16.

4.1 Introduction

Methods for characterizing the structure and function of membrane proteins have lagged behind corresponding approaches for the study of soluble proteins. Despite significant advances in structural methods applied to membrane proteins (1-3), it is often difficult to identify and implement the best conditions for purifying membrane proteins and for studying their functional interactions with ligands or other proteins. As a result many membrane proteins are studied in a diverse range of artificial membranes or detergents that are not optimal for all the studies desired for a complete characterization. The fundamental kinetic and thermodynamic parameters that describe the interaction of many protein complexes are required for accurate prediction of binding to cell surface receptors. However the effects of receptor solubilization on these in vitro parameters remain uncertain and likely vary for different receptors. Even with a wide range of lipid systems or detergents available, many analytical methods applied to systems of this type remain difficult or impossible.

Surface Plasmon Resonance (SPR) has revolutionized the study of molecular interactions between soluble proteins and their partners or small molecule ligands. However, the application of SPR to membrane proteins is sometimes successful but may be significantly more susceptible to artifacts (4-7). These experiments often include immobilization of a soluble protein, or solubilized portion of a membrane protein, on a sensor chip with subsequent analysis of a soluble binding partner as an analyte. In principle, there could be value in immobilizing full length membrane proteins in a native-like membrane environment using soluble proteins or small molecule ligands as analytes. Indeed, attempts have been made to use liposomes as the membrane in this experimental approach (8-10). However, a few problems with liposomes are likely to limit the generalizability of the approach. Liposomes are large, unstable and may fuse to form larger vesicles or aggregates. There may also be a large extent of non-specific partitioning of ligands into excess lipids. In short, traditional membrane platforms have limitations when used in SPR analyses.

Despite great effort to characterize the fundamental mechanism of P-gp and its interactions with drugs, its large size and integral membrane character have made progress difficult. As demonstrated in previous chapters where P-gp nanodiscs were exploited for FCS or H/DX MS, P-gp nanodiscs could also enable surface plasmon resonance (SPR), which could be a powerful method for studying the interactions of P-gp with drug substrates and inhibitors. SPR can provide kinetic information and binding affinities for proteins with ligands, but its application with membrane proteins has been nearly nonexistent. Therefore, protocols for the study of membrane proteins in nanodiscs with SPR could provide a much needed starting point for the application of SPR to study P-gp. However, there are only a few examples of the application of nanodiscs to study membrane proteins by SPR (11-15) and the limited experience with this combination of technologies suggests that many experimental parameters must be considered and optimized. This chapter focuses on the optimization of methods and conditions to apply SPR to the proteins in nanodiscs, with the potential to apply them to study drug-P-gp interactions in the future.

One distinction to consider is the advantages of nanodiscs compared to liposomes in studying these interactions. A few previously published experiments from our lab, combined with some experiments not previously described, demonstrate the potential utility of P-gp nanodiscs in contrast to P-gp liposomes. An interesting and useful feature of nanodisc-incorporated transmembrane proteins is that epitopes on both sides of the membrane are available for analysis. This is demonstrated in Figure 4.1 with an example in which two different antibodies can be observed to bind to human P-glycoprotein incorporated into nanodiscs by SPR. A second example with P-glycoprotein-nanodiscs demonstrates that both sides must be available in at least some particles. Here ATP and VO_4^- bind to the cytosolic nucleotide-binding domains and cause a conformational change that releases the UIC2 antibody, known to bind at the external side of P-gp in its ligand free form. Such a result would not be possible with liposomes where both nucleotide and the UIC2 antibody could not reach their binding sites on a single P-gp. Clearly, nanodiscs provide a potential means of studying complex interactions via SPR with some unique advantages. Therefore, the purpose of this chapter is to provide protocols for the initial parameterization of SPR experiments in which a membrane protein or receptor incorporated in a nanodiscs is immobilized on SPR chips for analysis of binding to a soluble partner protein. Methods to prepare the CM5, L1 and NTA sensor chips with nanodiscs are described (Figure 4.2). Furthermore, examples of small-molecule SPR experiments are shown, using model P-gp substrates, verapamil and vinblastine, to obtain kinetic rates and demonstrate multiple drug binding sites.

4.2 Materials and Methods

4.2.1 Protein Expression and Purification

P-gp and MSP1D1 were expressed and purified as previously described in Chapter 2.

4.2.2 Reconstitution into Nanodiscs and Purification

POPC empty nanodiscs used for testing biosensor surface capacity and stability were formed by mixing POPC (1-palmitoyl-2-oleoyl-sn-glycero-3-phosphocholine) and MDP1D1 in a 65:1 ratio with sodium cholate in disc forming buffer (100 mM potassoum phosphate, 50 mM sodium chloride, pH 7.4) and incubated on a nutator for 1 hour at 4 °C. To remove the detergent, pre-washed Amberlite XAD2 resin was added and the sample was incubated for an additional 4 hours at 4 °C and empty nanodiscs were recovered by passing through a 25 Ga needle. P-gp was reconstituted into DMPC lipid nanodiscs and purified as described in Chapter 2.

4.2.3 SPR Experiments

Because the presence of nanodisc presents additional options for capuring proteo-nanodiscs on SPR sensor chips and additional surfaces for nonspecific binding, compared to nonmembrane proteins, it was essential to first characterize the interaction of empty nanodiscs with various chip surfaces.

4.2.3.1 Immobilization of Anti-6 Histidine Antibody on a CM5 Chip and Nanodiscs Capture

The CM5 chip consists of a layer of carboxymethylated dextran immobilized onto a gold surface. Molecules such as proteins can be covalently attached to the free carboxyl groups via amine, aldehyde or thiol functional groups.

The CM5 chip was first activated with a 10-minute injection of 0.4 M 1-ethyl-3-(3-dimethylaminoprolyl)-carbodiimide (EDC)/0.1 M N-hydroxysuccinimide (NHS) mixture at a flow rate of 10µl/min, followed by an injection of 86 µg/ml of mouse anti-6-histidine antobody diluted in 10 mM sodium acetate (pH 4.5) for 5 minutes to reach immobilization level of 13000 RU. The surface was deactivated with an injection of 1M ethanolamine, pH 8.5, for 7 minutes. Two 20-seconds pulses of regeneration solution containing 10 mM glycine (pH 1.5) were included to stabilize the surface before priming instrument with running buffer (100 mM KPi, 50 mM NaCl, pH 7.4) and loading with nanodiscs. To investigate surface capacity and post-capture stability, various concentrations (0.5, 2 and 8 µM) of histidine-tagged empty nanodiscs were injected for 3 minutes at a flow rate of 10µl/min.

4.2.3.2 Capture of Nanodiscs using the L1 Chip

The L1 sensor chip is comprised of lipophilic alkyl chains covalently attached to carboxymethylated dextran on the surface. The alkyl chains insert into the lipid layer of vesicles or liposomes, therefore there is no need for additional affinity tags on the protein or lipid. This sensor chip is also suitable for nanodisc work because of the presence of a lipid bilayer, which is expected to incorporate the alkyl chains from the chip as a method of 'capture.'

The L1 chip was first washed with two 30-seconds pulses of 20 mM CHAPS before equilibration with running buffer (100 mM KPi, 50 mM NaCl, pH 7.4). 0.5, 2 and 8 µM of empty nanodiscs were injected at a flow rate of 10µl/min for 30 minutes, before coating any unbound sensor surface with BSA (0.2mg/ml for 5 minutes) to reduce non-specific binding of analyte. The level of BSA captured also provides an indication of the degree of sensor chip saturation with nanodiscs, because a fully saturated surface will not bind BSA (or only to a small extent).

4.2.3.3 Capture and Immobilization of Nanodiscs using the NTA Chip

The NTA chip consists of a carboxylmethylated dextran matrix pre-immoblized with nitrilotriacetic acid (NTA). This allows affinity capture of histidine-tagged proteins via Ni-NTA complex.

The NTA chip was preconditioned with three 1-minute injections of 350 mM EDTA (pH 8.0) at a flow rate of 30 µl/min, followed by a wash step with running buffer (100 mM KPi, 50 mM NaCl, pH 7.4). 500 µM $NiCl_2$ solution diluted in running buffer was injected at a flow rate of 10 µl/min for 1 minute to charge the surface, followed by an extra wash step with 3 mM EDTA and stabilization for 1 minute. Charging with Ni^{2+} resulted in an increase of ~ 40 RU. 0.5, 2 and 8 µM of empty nanodiscs were injected at a flow rate of 10µl/min for 3 minutes .

To perform crosslinking of nanodiscs on a NTA chip, steps were carried out as above with an injection of 500 µM Ni^{2+} solution for 3 minutes. Flow cells were activated with an injection of 0.4 M EDC /0.1 M NHS mixture at a flow rate of 10µl/min for 5 minutes, followed by loading empty nanodiscs or P-gp nanodiscs (10 mM HEPES, 350 mM NaCl, pH 7.4) onto reference or sample flow cell respectively. 400 nM P-gp nanodiscs were injected at a flow rate of 5 µl/min for 12 minutes (about 4500 to 6000 RU) and empty nanodiscs were injected to reach 2250 to 3000 RU. Remaining exposed surface was deactivated with an injection of 1M ethanolamine, pH 8.5, for 7 minutes and nickel was stripped from the surface with a 1 minute pulse of 350 mM EDTA.

4.2.3.4 SPR Binding Experiments and Data Analysis

Binding experiments were performed at 25ºC on Biacore T200 at a flow rate of 50 µl/min in running buffer containing 20 mM Tris, 350 mM NaCl, 2% DMSO, pH 7.4. Association and dissociation of tested analytes were set at 120 and 300 s respectively. Sensorgrams were solvent corrected and double referenced (signals from reference flow cell were substracted from sample flow cell and corrected with a buffer injection). All referenced sensorgrams were analyzed with Biacore T200 evaluation software for equilibrium and kinetic binding parameters.

4.3 Results

4.3.1 Comparison of Empty Nanodiscs Capture between Different Chips

CM5 Chip

The anti-6-his antibody coupled CM5 chip had a lower capture level than the NTA chip but higher than the L1 chip (Figure 4.3). However, the post-capture stability was less than the L1 chip. Comparing the stability of similar capture levels of nanodiscs (~3000 RU; the 2 uM curve for L1 and the 0.5 uM curve for CM5) we observed that material on L1 showed no loss during the stabilization period yet 1.7 % of the initial capture was lost from the CM5 chip (49 RU).

L1 Chip

The L1 chip saturated at ~ 3500 RU of empty nanodiscs (Figure 4.3C). When levels less than 3000 RU were captured, a response was detected from the BSA injection; for capture levels around 2000 RU there was an increase of ~100 RU of BSA. The post-capture baseline was the most stable among all the tested chips as depicted in Figure 4.3E.

NTA Chip

The nickel-activated NTA surface captured significantly more nanodiscs than either the CM5/Ab or L1 chips, with over 10,000 RU captured at the highest ligand concentration (Figure 4.3A). However at these high capture levels the stability was extremely poor (Figure 4.3E).

4.3.2 Real Time Monitoring of Analyte Binding by SPR

In order to maximize the signal from small molecule binding events to P-gp nanodiscs, the NTA chip was chosen because it offered the highest capacity for nanodiscs loading. To overcome the problem of unstable baseline and dissociation of nanodiscs from the biosensor surface, amine coupling was performed in addition to histitidine-tag capture by nickel to provide a stable baseline. Although the final level of captured-crosslinked nanodiscs was ~6000 RU compared to captured-uncrosslinked nanodiscs (~16800 RU), possibly due to limited dextran sites available for crosslinking, the immobilized level was higher than what could be obtained with L1 or anti-his antibody coupled CM5 chip and was suitable for small molecule experiments. In this setup, between 1 to 60 RUs of signal were observed from the two common substrates of P-gp. Duplicate injections of the concentration series of each compound were highly reproducible and saturation of a high affinity site could be observed, demonstrating the robustness and stability of the system. Binding constants (K_D) obtained from steady-state analyses of verapamil and vinblastine at low occupancy were 28.6 ± 7.05 uM and 15.4 ± 1.8 uM respectively, which were in close approximation to the K_M values of 55.7 ± 14.8 uM and 2.6 ± 1.0 uM measured from activity assays (Chapter 2, Table 2.1 and Figure 2.4). Kinetic analyses of the sensorgrams revealed a mass-transport limited fast phase in both on- and off-rates for verapamil and vinblastine, which indicates on-rates greater than 10^5/M•sec and off-rates greater than 1/sec. A second slow phase in the on-rates for verapamil and vinblastine was observed, which may indicate heterogeneity in the system.

At higher drug concentrations, the association phase was non-saturable within 120 s. In addition, a slower off-rate of 0.02/sec was observed for vinblastine binding based on a separate, double exponential fit of the dissociation phase. A slower off-rate is consistent with the higher affinity of vinblastine for P-gp compared to verapamil.

4.4 Discussion

It is clear that there are different approaches (i.e. different biosensor chips, capture or immobilization strategies) to study membrane protein in nanodiscs using SPR. However, careful design and consideration of experimental setup is required to obtain reliable sensorgrams. While developing and optimizing these assays we have found the following parameters to be important.

1. Purity of Nanodiscs

It is critical that nanodisc preparations be as pure as possible. We recommend removing empty nanodiscs from a his-tagged proteonanodisc preparation by nickel chromatography followed by size exclusion chromatography. For the L1 chip it is important to purify the discs by size exclusion chromatography because liposomes and various lipid-protein complexes can also be captured via the lipophilic substituent.

2. Desired Nanodisc Capture Level

This depends on many factors including the specific analyte (high molecular weight versus small molecule) as well as the goal of the experiment (quantitative kinetics or qualitative response). In either case, one should first calculate the R_{max}, the theoretical maximal response obtainable for the analyte:

R_{max} (RU) = (analyte mol wt / ligand mol wt) X immobilized ligand (RU) X stoichiometry

High molecular weight analytes will result in greater response so lower capture levels are adequate. Low molecular weight analytes requires greater capture levels to achieve a detectable Rmax. In addition some analytes may demonstrate mass transfer limited binding requiring low capture levels (see point 4). The L1 chip requires more nanodiscs due to longer capture time (15-30 min) compared to CM5 and NTA chip (1-2 min).

3. Choosing a reference surface

A well matched reference surface is critical to deal with artifacts arising from possible refractive index changes in the analyte solution (the bulk effect), injection noise, and non-specific binding. We recommend using empty nanodiscs as the reference surface. If empty nanodiscs are unavailable for the reference cell, an anti-6-his antibody immobilized CM5 chip or a deactivated CM5 surface (capped with ethanolamine) can be used. In the case of NTA chip, the reference cell can be the naive NTA surface (uncharged with Ni^{2+}); a charged surface is not recommended due to issues with non-specific binding.

4. Mass Transfer Limitations

The transfer of the analyte from the bulk flow to the sensor surface is a diffusion-controlled process. To minimize possible mass transfer limitations for kinetic experiments, lower capture levels of nanodisc (ligand) on the surface and fast flow rates (30 – 100uL/min) of analyte are recommended. Both help reduce the analyte consumption and diffusion distance. Mass transfer limitation can be checked by using different flow rates for the analyte injection. If mass transfer limitation occurs, the apparent rates of both association and dissociation will increase as the flow rate increases.

5. Baseline drift with different chips

Baseline drift, the dissociation of captured nanodiscs from the surface of the chip, complicates the analysis of analyte binding especially in cases where the level of drift approaches the analyte response level. In addition different rates of drift between the experimental and reference cell must be taken into account. This will likely vary with individual proteins and can be tested.

The L1 chip has been observed to provide the most stable baseline of captured nanodiscs compared to the CM5/Ab chip and NTA chip. Although both the NTA and CM5 chip demonstrate significant drift at high capture level, lowering the capture level can improve the stability of response on the surface. Nanodiscs can also be captured and crosslinked on the NTA chip to improve stability.

6. Non-specific binding

It is important to initially test for non-specific binding by injecting analyte over the reference surface of empty nanodiscs. If binding is detected, the source may be determined by performing control experiments injecting analyte over surfaces without the nanodiscs, such as the deactivated surface or anti-6-his antibody surface for CM5 chip, the NTA or Ni-NTA surface for NTA chip, or the exposed hydrophobic layer on the L1 chip. In some cases the running buffer can be optimized to reduce the non-specific binding by adding: soluble carboxymethyl dextran (NSB reducer, GE Healthcare), high salt (up to 500mM NaCl), BSA (up to 2 mg/ml), or EDTA (250 uM). Detergents should be avoided because they can affect the lipid bilayer.

With these key parameters in mind, experiments were performed to monitor real-time binding of small molecules to P-gp nanodiscs using SPR. So far, there are no direct kinetic analyses of drug binding to P-gp. Determination of the kinetic rate constants may provide critical information such as the rate-determining step in the transport cycle of P-gp, and the extent to which substrate binding and transport is coupled to the ATPase activity of the transporter. This provides an idea of the efficiency of P-gp as a transporter in harnessing the energy from ATP hydrolysis to result in productive translocation of drugs across the membrane, which is most likely to vary between drugs (i.e. substrates and inhibitors). SPR provides a direct measurement of association and dissociation rate constants in addition to equilibrium binding parameters. Other advantages include low sample consumption, a fully automated system, and versatility of biosensor chips for different capture/immobilization strategies.

We first assessed the binding of two typical substrates of P-gp, verapamil and vinblastine, to P-gp nanodiscs captured and crosslinked onto a NTA chip. We chose the NTA chip because a high level of captured nanodiscs is required to maximize the signal from small molecule binding events. However, due to the unstable baseline at such high levels of capture we included an additional crosslinking step to immobilize the captured nanodiscs onto the surface using amine-coupling chemistry. This resulted in a much more stable baseline, although a lower level of nanodiscs was immobilized, which suggests that the available dextran sites for crosslinking are limited on the NTA chip (Figure 4.4). Nevertheless, the amount of P-gp immobilized (~ 5500 RU) was adequate to observe signals from small molecule binding. Similarly, a matching level of empty nanodiscs (~ 2250 RU) based on mass differences was immobilized in the reference flow cell. Steady-state analyses of the sensorgrams for both verpamamil and vinblastine revealed a high affinity binding site, with $K_D = 28.6 \pm 7.05$ µM and 15.4 ± 1.8 µM respectively, in close approximation to the K_M values of these drugs based on ATPase activity measurements (Figures 4.5 and 4.7). Interestingly, the signal demonstrated an intial saturation at around 5-6 RU for verapamil at the high affinity site, which was close to the expected signal from the binding of one molecule of verapamil to P-gp (7-9 RU) based on a mass ratio calculation, from equation in Parameters, point 2. With increasing concentrations of verapamil, a nonsaturable binding component was observed, as elaborated below. Similarly, the signal for vinblastine saturated at around 3-4 RU at the high affinity site, which was lower than the value expected from one molecule of vinblastine binding to P-gp (~ 15-18 RU). It is possible that the lower solubility or increased hydrophobicity of vinblastine may contribute to this result because there may be more non-specific binding to the empty nanodiscs (which is subtracted) and P-gp also encounters less of the soluble drug for a given concentration. Due to this uncertainty, the results with vinblastine must be considered with caution.

A more detailed assessment of the sensorgrams reveals that there are fast and slow processes in the association and dissociation phases of both drugs (Figures 4.6 and 4.8). The initial linear association/dissociation kinetics is indicative of mass transport limited (MTL) binding, and only the lower bounds of the rates could be determined. The fast association rates for both drugs are greater than 10^5/M•sec because in the case of MTL, the rate of diffusion of drugs from the bulk flow to the receptor sites on the biosensor surface is slower than the actual rate of association of drugs to P-gp. Indeed, in a confluent monolayer cell system, the rate of association of drugs to P-gp has been reported to be in the range of 10^9 to 10^{10}/M•sec that is limited by the lateral diffusion of drugs within a lipid layer (16,17). The linear dissociation phase also limits extraction of kinetic information, but it suggests that the fast dissociation rates for both drugs have to be greater than 1/s. Notably, a slower dissociation phase was observed in the case of vinblastine but not for verapamil, which is in good agreement with a higher affinity for vinblastine than verapamil. The off-rate of vinblastine was around 0.02/s, and a slower off-rate of 0.093/min has been reported for radiolabeled vinblastine (18). An interesting observation is that the steady-state response does not saturate at higher concentrations. The lack of saturation at higher drug occupancy indicates the presence of weaker, and perhaps non-specific, binding sites on the receptor. As alluded to in Chapter 1, P-gp is capable of binding to multiple drug molecules and there are high and low drug affinity sites which allosterically activate or inhibit ATPase activity. Subsequently, we performed separate analysis of the off-rates of vinblastine at low and high concentrations in order to discern kinetic differences at the high and low affinity sites. A slower off-rate of 0.002/s was obtained for vinblastine at low concentrations, which is close to the value previously reported. Collectively, it appears that the off-rates for vinblastine vary about 10 fold between the high and low affinity sites. Taking into account a 20-fold difference in K_M based on activity assays, it may be speculated that drug binding affinity to P-gp is primarily governed by dissociation rate.

An observation that needs more work to address is the presence of a second slow association phase that takes a longer time to reach steady-state and may arise from heterogeneity in the system. Sources of heterogeneity include non-uniform orientation of immobilized protein, multiple protein conformations, or analyte heterogeneity. More experiments that include different immobilization strategies, varying association and dissociation duration will be required to test which model is operative. Despite the complexity of the SPR data that prevents definitive conclusions about the stoichiometry and mechanism of binding it is particularly interesting to consider the possibility that the binding complexity is related to the conformational complexity of P-gp that was observed in the H/DX MS experiments in Chapter 3. Specifically, the slow conformational changes suggested by the EX1 kinetics of some peptides would possibly yield slow binding phases in the SPR experiments.

In summary, this chapter describes SPR as a powerful tool that can be applied to membrane proteins in nanodiscs to dissect the intricacies of ligand binding. However, detailed work is needed to fine-tune experimental conditions to obtain reliable and reproducible kinetic information. Importantly, we have successfully demonstrated the use of SPR for monitoring substrates binding to P-gp nanodiscs. The lower bounds of the association and dissociation rates are obtained from these experiments, and we have also shown that the off-rate is drug-dependent. The kinetics of these drugs binding to P-gp suggest that relatively weak substrate binding, which entails fast association and dissociation rates, may be a dominant mode of action for P-gp to transport a broad range of substrates out of the cell.

Figures

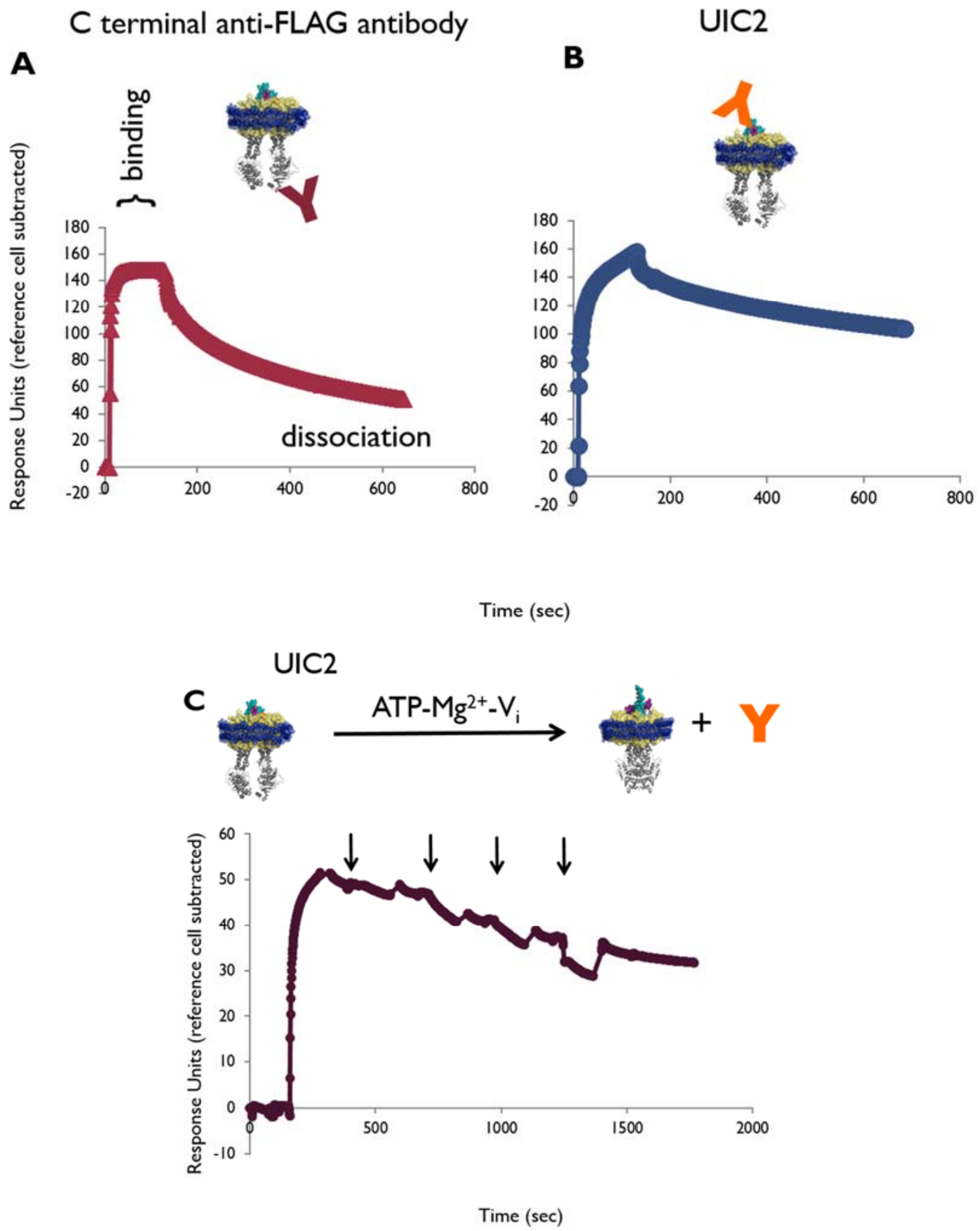

Figure 4.1. SPR can be used to interrogate membrane protein epitopes on either side of the membrane. P-glycoprotein (Pgp) embedded in MSP1D1E3/*E.coli* lipid nanodiscs were captured on L1 sensor chips. (A) Monoclonal antibody (M2) binding to the C-terminal FLAG tag on the cytosolic side of P-gp detected by SPR. (B) Monoclonal antibody (UIC2) to an extracellular epitope detected by SPR. (C) UIC2 bound to Pgp nanodiscs on the L1 chip is eluted by increasing concentrations of ATP-Mg^{2+}-orthovanadate (injections depicted by arrows). ATP-Mg^{2+}-orthovanadate binds to the nucleotide binding domain of P-gp, alters the conformation of Pgp and lowers the affinity for UIC2 antibody. In these experiments the reference cell contained empty nanodiscs.

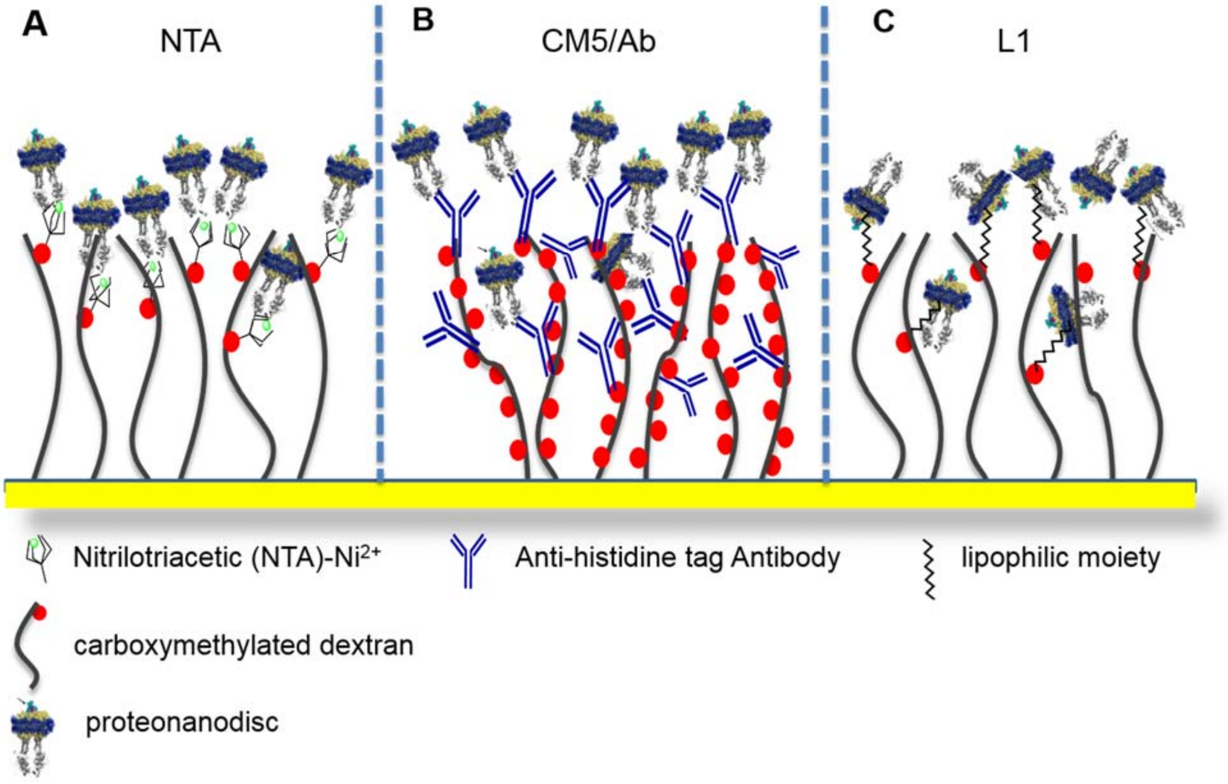

Figure 4.2. A schematic of the SPR sensor chips and their capture strategies. Depicted are three Biacore sensor chips tested for capturing nanodiscs. All chips have a gold layer coated with a carboxymethylated dextran matrix. The first two chips, NTA and CM5/Ab, exploit the histidine tag on the nanodiscs for capture. The third, the L1 chip, uses the lipid bilayer for capture. (A) The nitrilotriacetic acid (NTA) chip is charged with nickel ions that chelate the NTA and the histidine-tagged nanodisc. (B) The CM5 chip uses amine coupling to covalently link an anti-histidine tag antibody to the chip surface that binds to the histidine-tagged nanodiscs. (C) The L1 chip has a proprietary lipophilic substituent on the dextran that inserts into the bilayer.

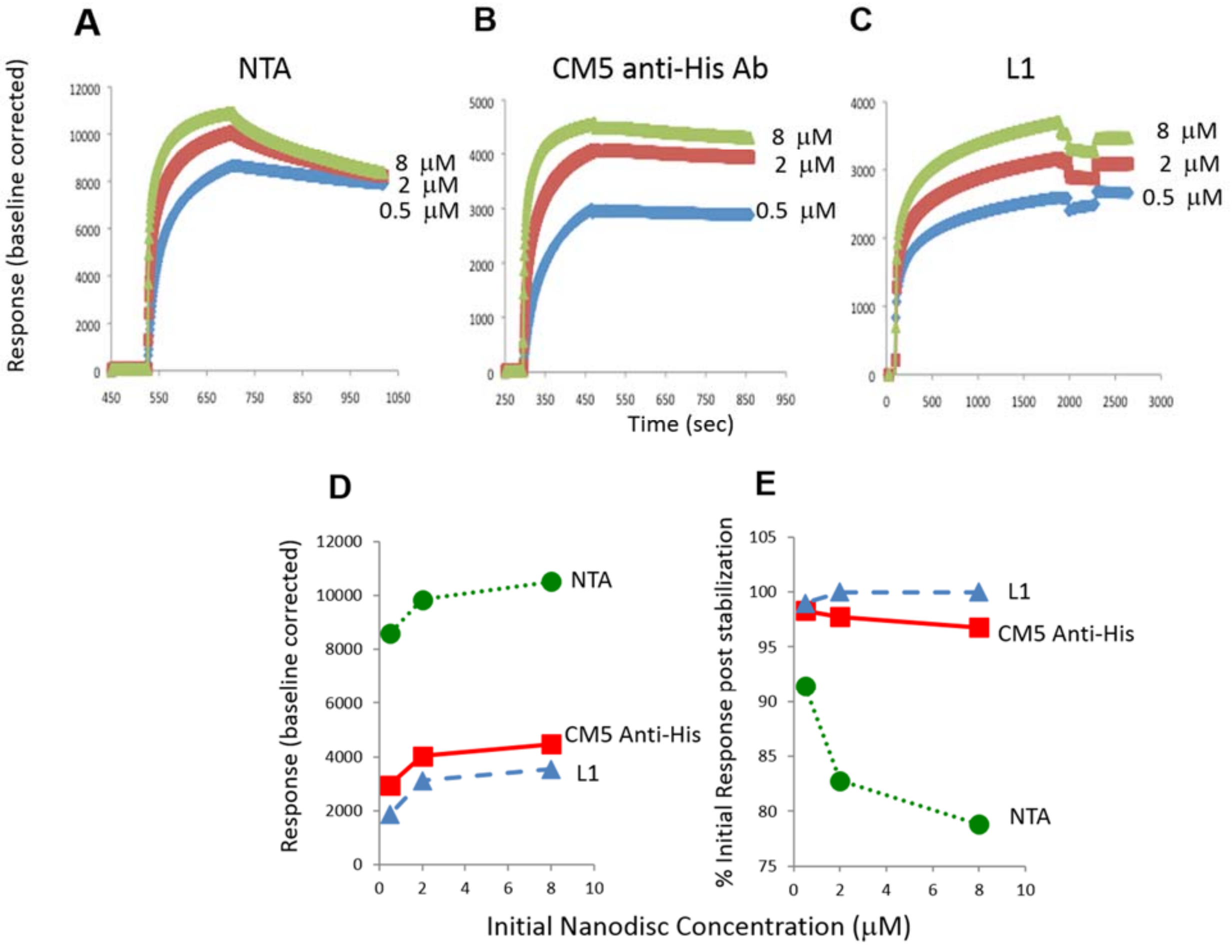

Figure 4.3. Capture and stability of nanodiscs on NTA, CM5 anti-histidine antibody and L1 sensor chips. Three concentrations of histidine-tagged MSP1D1-POPC empty nanodiscs (8, 2 and 0.5 μM) were captured on three different sensor chips. (A) The NTA chip surface was charged with nickel and then loaded with the indicated concentrations of nanodiscs for 3 min followed by a 5 min stabilization period. (B) The CM5 chip was activated with EDC/NHS to amine couple the anti-6-his antibody and then loaded with nanodiscs for 3 min followed by a 5 min stabilization period. (C) The L1 chip was conditioned with brief injections of 20 mM CHAPS, washed with buffer then loaded with nanodiscs for 30 min, tested for saturation with BSA, followed by a 5 min

stabilization period. The decline seen (noted with *) is the bulk shift effect due to the BSA injection. All chips were regenerated in between cycle of increasing nanodiscs concentrations. (D) The capture capacity of the different chips derived from the data in (A)-(C) as a function of the initial nanodiscs concentration used for capture. (E) The percentage of the captured nanodiscs response remaining after the 5 min stabilization period as a function of the initial nanodiscs concentration used for capture.

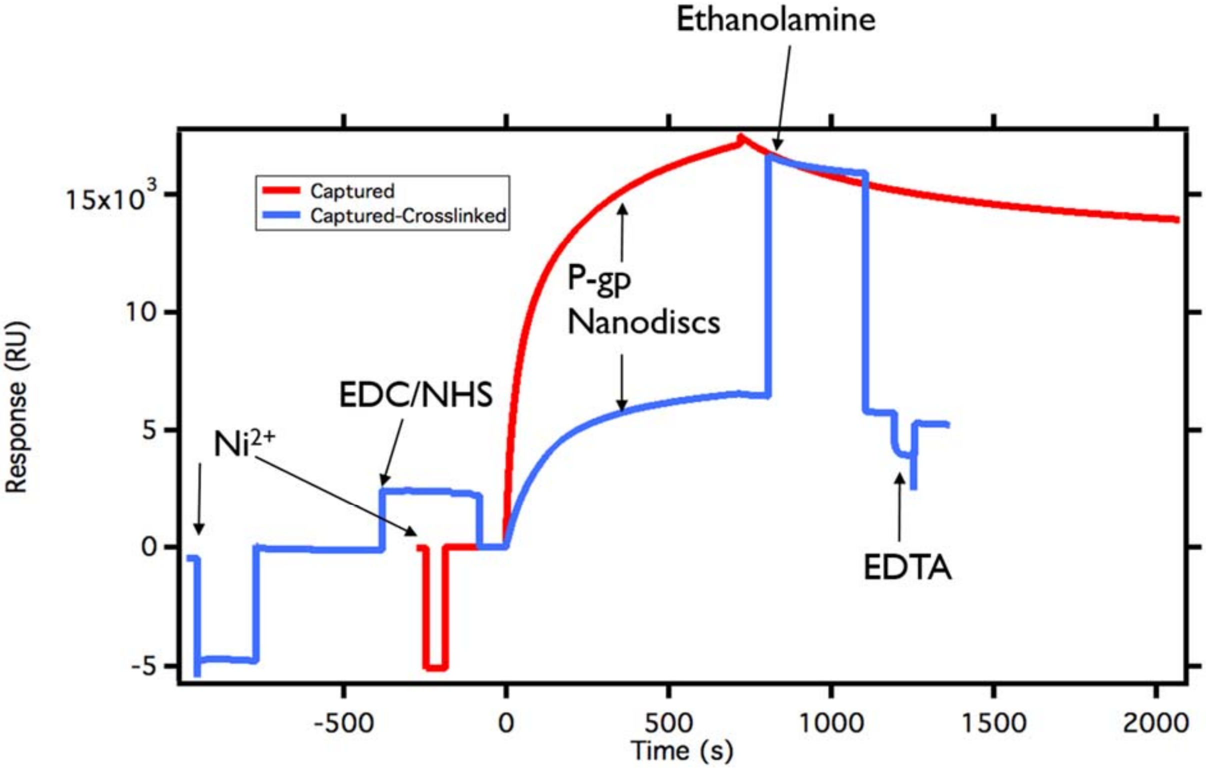

Figure 4.4. Comparison between P-gp nanodiscs captured or captured-crosslinked onto a NTA chip. For capture only, the NTA chip was charged with 500 μM $NiCl_2$ for 1 min, followed by an extra wash step with 3 mM EDTA and stabilization for 1 min before loading with P-gp nanodiscs for 12 minutes (shown in red). For capture-crosslinking, the NTA chip was charged with 500 μM $NiCl_2$ for 3 min with extra wash step and stabilization as described previously, with an activation of the surface by an injection of 0.4 M EDC /0.1 M NHS mixture at a flow rate of 10μl/min for 5 minutes, before loading with P-gp nanodiscs for 12 minutes. Surface was deactivated with an

injection of 1M ethanolamine for 7 minutes and Ni^{2+} was removed from the surface with a 1 minute pulse of 350 mM EDTA. One-third of the protein was immobilized on the surface using the capture-crosslink approach, but the post-immobilization baseline was more stable than capture only approach.

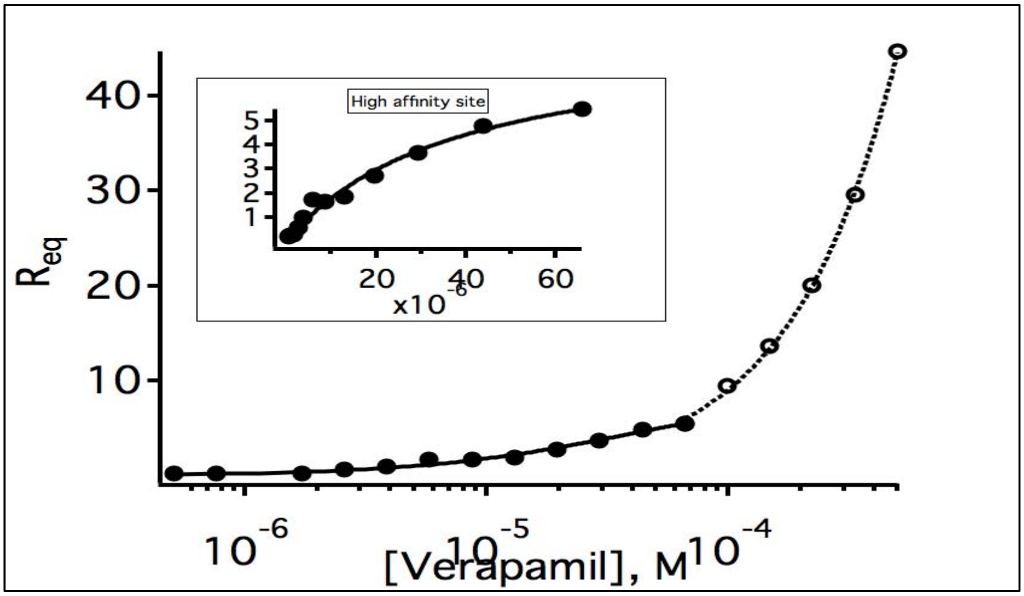

Figure 4.5. Semi-log plot of equilibrium response of verapamil binding to P-gp nanodiscs immobilized onto the NTA chip. A two-site steady state binding model is used to determine the binding constants for verapamil binding to the high and low affinity sites. Binding constant for the high affinity site can be determined because the signal reached saturation (inset; normal plot) and the saturating signal is well within the response expected from the binding of a molecule of verapamil. The binding constant for the low affinity site cannot be determined accurately because of non-saturating response at the highest drug concentration.

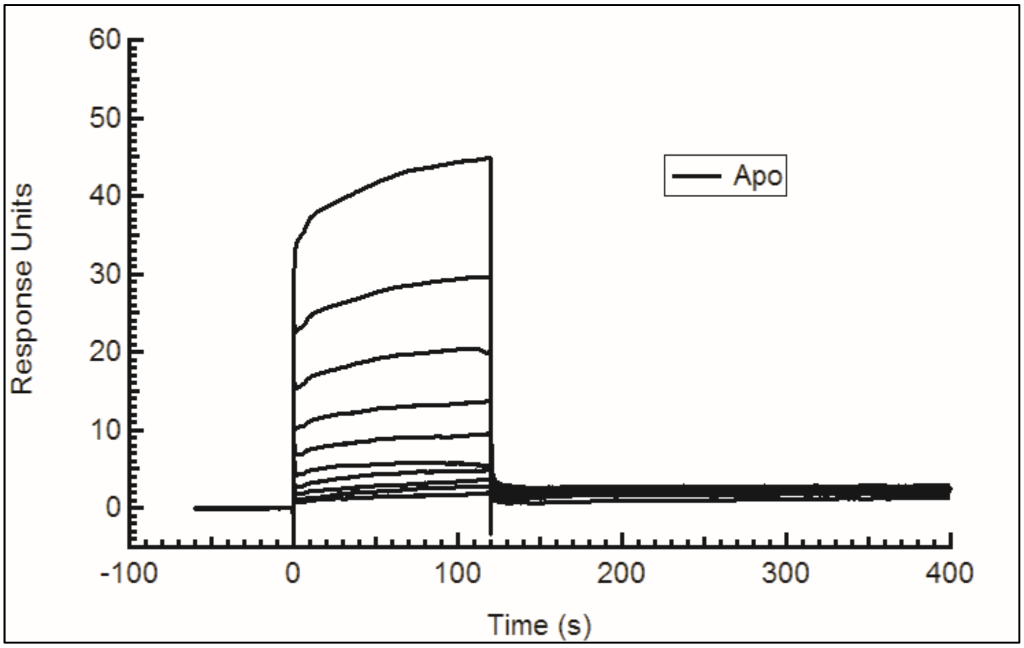

Figure 4.6. SPR sensorgram of verapamil binding to P-gp nanodiscs immobilized onto the NTA chip. Dose-response curves obtained with an association duration of 120 s and dissociation period of 300 s, at a flow rate of 50µl/min. Note that the binding signal does not saturate at high concentrations, suggesting that weak and possibly non-specific binding is involved. The presence of a slow association phase indicates some sources of heterogeneity the system.

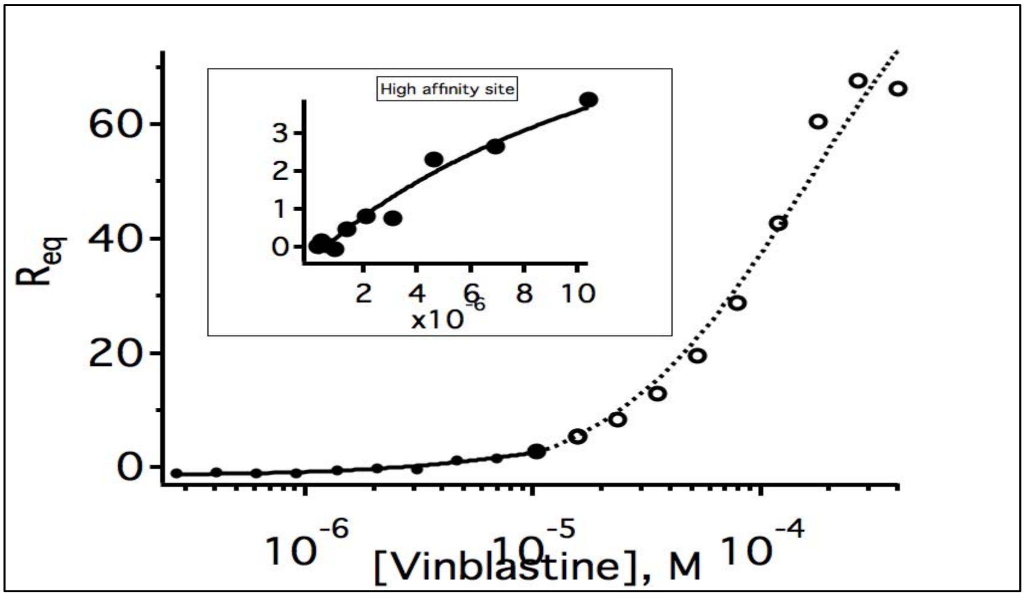

Figure 4.7. Semi-log plot of equilibrium response of vinblastine binding to P-gp nanodiscs immobilized onto the NTA chip. A two-site steady state binding model is used to determine the binding constants for vinblastine binding to the high and low affinity sites. Binding constant for the high affinity site can be estimated because the signal is reaching saturation (inset; normal plot), however the signal is lower than expected from the binding of a molecule of vinblastine, possibly because of a larger extent of non-specific binding to the empty nanodiscs in the reference cell which has been subtracted. The binding constant for the low affinity site cannot be determined accurately because of non-saturating response at the highest drug concentration.

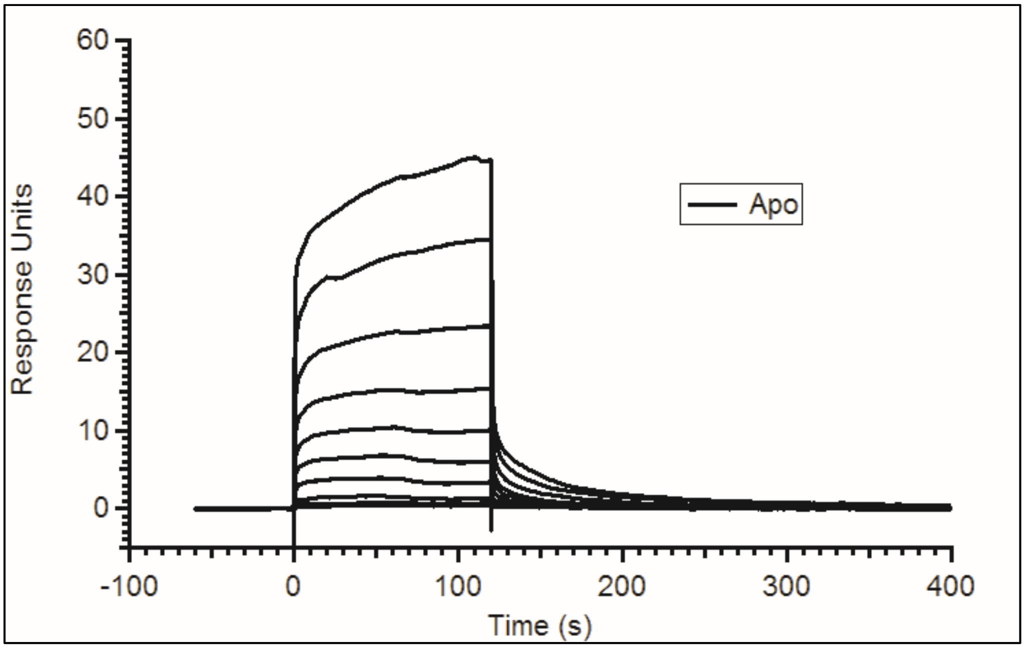

Figure 4.8. SPR sensorgram of vinblastine binding to P-gp nanodiscs immobilized onto the NTA chip. Dose-response curves obtained with an association duration of 120 s and dissociation period of 300 s, at a flow rate of 50µl/min. Note that similar to verapamil, the binding signal does not saturate at high concentrations, suggesting that weak and possibly non-specific binding is involved. The presence of a slow association phase indicates some sources of heterogeneity the system. Compared to verapamil, vinblastine has a slower off-rate which is consistent with a higher affinity for P-gp.

4.5 References

1. Baker, L. A., and Baldus, M. (2014) Characterization of membrane protein function by solid-state NMR spectroscopy. *Curr Opin Struct Biol* **27**, 48-55
2. Huster, D. (2014) Solid-state NMR spectroscopy to study protein-lipid interactions. *Biochim Biophys Acta* **1841**, 1146-1160
3. Moraes, I., Evans, G., Sanchez-Weatherby, J., Newstead, S., and Stewart, P. D. (2014) Membrane protein structure determination - the next generation. *Biochim Biophys Acta* **1838**, 78-87
4. de Mol, N. J. (2012) Surface plasmon resonance for proteomics. *Methods Mol Biol* **800**, 33-53
5. Rich, R. L., and Myszka, D. G. (2000) Advances in surface plasmon resonance biosensor analysis. *Curr Opin Biotechnol* **11**, 54-61
6. Rich, R. L., and Myszka, D. G. (2010) Grading the commercial optical biosensor literature-Class of 2008: 'The Mighty Binders'. *J Mol Recognit* **23**, 1-64
7. Hahnefeld, C., Drewianka, S., and Herberg, F. W. (2004) Determination of kinetic data using surface plasmon resonance biosensors. *Methods Mol Med* **94**, 299-320
8. Maynard, J. A., Lindquist, N. C., Sutherland, J. N., Lesuffleur, A., Warrington, A. E., Rodriguez, M., and Oh, S. H. (2009) Surface plasmon resonance for high-throughput ligand screening of membrane-bound proteins. *Biotechnol J* **4**, 1542-1558
9. Zeng, S., Baillargeat, D., Ho, H. P., and Yong, K. T. (2014) Nanomaterials enhanced surface plasmon resonance for biological and chemical sensing applications. *Chem Soc Rev* **43**, 3426-3452
10. Kinouchi, H., Onishi, M., and Kamimori, H. (2013) Lipid membrane-binding properties of daptomycin using surface plasmon resonance. *Anal Sci* **29**, 297-301
11. Das, A., Zhao, J., Schatz, G. C., Sligar, S. G., and Van Duyne, R. P. (2009) Screening of type I and II drug binding to human cytochrome P450-3A4 in nanodiscs by localized surface plasmon resonance spectroscopy. *Anal Chem* **81**, 3754-3759
12. Goluch, E. D., Shaw, A. W., Sligar, S. G., and Liu, C. (2008) Microfluidic patterning of nanodisc lipid bilayers and multiplexed analysis of protein interaction. *Lab Chip* **8**, 1723-1728
13. Proverbio, D., Roos, C., Beyermann, M., Orban, E., Dotsch, V., and Bernhard, F. (2013) Functional properties of cell-free expressed human endothelin A and endothelin B receptors in artificial membrane environments. *Biochim Biophys Acta* **1828**, 2182-2192
14. Ritchie, T. K., Kwon, H., and Atkins, W. M. (2011) Conformational analysis of human ATP-binding cassette transporter ABCB1 in lipid nanodiscs and inhibition by the antibodies MRK16 and UIC2. *J Biol Chem* **286**, 39489-39496
15. Gluck, J. M., Koenig, B. W., and Willbold, D. (2011) Nanodiscs allow the use of integral membrane proteins as analytes in surface plasmon resonance studies. *Anal Biochem* **408**, 46-52
16. Tran, T. T., Mittal, A., Aldinger, T., Polli, J. W., Ayrton, A., Ellens, H., and Bentz, J. (2005) The elementary mass action rate constants of P-gp transport for a confluent monolayer of MDCKII-hMDR1 cells. *Biophys J* **88**, 715-738
17. Tran, T. T., Mittal, A., Gales, T., Maleeff, B., Aldinger, T., Polli, J. W., Ayrton, A., Ellens, H., and Bentz, J. (2004) Exact kinetic analysis of passive transport across a

polarized confluent MDCK cell monolayer modeled as a single barrier. *J Pharm Sci* **93**, 2108-2123

18. Martin, C., Berridge, G., Higgins, C. F., Mistry, P., Charlton, P., and Callaghan, R. (2000) Communication between multiple drug binding sites on P-glycoprotein. *Mol Pharmacol* **58**, 624-632

VITA

Mavis Li received her Bachelor of Science (Pharmacy) with First Class Honors at the National University of Singapore in 2011. She joined the Department of Medicinal Chemistry at the University of Washington in the fall of 2011, and became a member of Professor William Atkins' lab. Her doctoral thesis work involved the use of nanodiscs technology to investigate the structure-function of P-glycoprotein, and she graduated with a Doctor of Philosophy in Medicinal Chemistry in 2017.